



**BRNO UNIVERSITY OF TECHNOLOGY**

VYSOKÉ UČENÍ TECHNICKÉ V BRNĚ

**CENTRAL EUROPEAN INSTITUTE OF TECHNOLOGY BUT**

STŘEDOEVROPSKÝ TECHNOLOGICKÝ INSTITUT VUT

**EFFECT OF SUB-MICROMETER STRUCTURAL FEATURES  
ON RHEOLOGY OF POLYMER NANOCOMPOSITES**

EFEKT SUBMIKROMETRICKÝCH RYSŮ NA REOLOGII POLYMERNÍCH NANOKOMPOZITŮ

**DOCTORAL THESIS**

DIZERTAČNÍ PRÁCE

**AUTHOR**

AUTOR PRÁCE

Ing. Petr Lepcio

**SUPERVISOR**

ŠKOLITEL

prof. RNDr. Josef Jančář, CSc.

**BRNO 2018**





## **ABSTRACT**

Polymer nanocomposites (PNCs) hold a great promise as future lightweight functional materials processable by additive manufacturing technologies. However, their rapid deployment is hindered by their performance depending strongly on the nanoparticle (NP) spatial organization. Therefore, the ability to control the nanoparticle dispersion in the process of PNCs preparation is a crucial prerequisite for utilizing their potential in functional composites. This work investigates solution blending of PNCs in a model glass forming polymer matrix, a bulk processing technique of a tailored NP spatial organization controlled by structural and kinetic variables of the preparation protocol. The presented results describe the differences between nanoparticle induced changes on the rheological behavior of a polystyrene solution under large amplitude oscillation shear (LAOS). High-affinity OP-POSS NPs seem to interact with the PS at low filler loadings and form stiffened aggregates, whereas low-affinity OM-POSS NPs remained rather uninvolved in the polymer deformation at these conditions. Furthermore, an interest was focused on the impact of the blending solvent on the NP spatial arrangement in silica/PMMA and silica/PS nanocomposites, which has already been suggested as the controlling parameter of the solid-state structure. An emphasis was put on the qualitative differences between “poorly dispersed” NP arrays which, by combination of rheological assessment and structural analysis (TEM, USAXS), were identified as chain bound clusters and two types of aggregates, one of thermodynamic and the other of a kinetic origin, which are characterized by substantially distinct formation kinetics and mismatched properties compared to individually dispersed NPs and each other. The currently observed types of NP dispersion were quantitatively linked with their rheological properties during the solution blending step and the amount of polymer adsorption and depletion attraction. The results were compared to the PRISM theory. Finally, the importance of NP spatial organization was demonstrated on the comparison of glass transition temperatures of various structures at constant chemical composition.

## **KEYWORDS**

Polymer nanocomposite (PNC), nanoparticle (NP), structure, spatial organization, dispersion, aggregate, chain bound cluster, depletion attraction, adsorption, acid-base interaction, solution blending, rheology, large amplitude oscillatory shear (LAOS), transmission electron microscopy (TEM), ultra-small angle X-ray scattering (USAXS), polystyrene (PS), poly(methyl methacrylate) (PMMA), silica, polyhedral oligomeric silsesquioxane (POSS)

## **ABSTRAKT**

Polymerní nanokompozity (PNCs) mají slibnou budoucnost jako lehké funkční materiály zpracovatelné aditivními výrobními technologiemi. Jejich rychlému rozšíření však brání silná závislost jejich užitečných vlastností na prostorovém uspořádání nanočástic (NP). Schopnost řídit disperzi nanočástic je tak klíčovým předpokladem pro jejich uplatnění ve funkčních kompozitech. Tato práce zkoumá přípravu polymerních nanokompozitů v modelové sklotvorné polymerní matici roztokovou metodou, technikou schopnou vytvářet prostorové uspořádání nanočástic řízené strukturními a kinetickými parametry přípravného procesu. Prezentované výsledky popisují rozdíly mezi změnami rheologického chování roztoku polystyrenu při oscilačním smyku s vysokou amplitudou (LAOS) vyvolanými nanočásticemi. Výsledky vedou k závěru, že vysoce-afinní OP-POSS nanočástice při nízkých koncentracích dobře interagují s PS a tvoří tuhé agregáty, zatímco nízko-afinní OM-POSS nanočástice za těchto podmínek neovlivňují deformační chování polymerních řetězců. Dále byla pozornost zaměřena na vliv použitého rozpouštědla na uspořádání nanočástic v  $\text{SiO}_2/\text{PMMA}$  a  $\text{SiO}_2/\text{PS}$  nanokompozitech, který je v literatuře prezentován jako parametr řídící prostorové uspořádání nanočástic v pevném stavu. Důraz byl kladen na kvalitativní rozdíly mezi „špatně dispergovanými“ shluky nanočástic, které byly na základě rheologie a strukturální analýzy (TEM, SAXS) identifikovány jako polymerními řetězci vázané nanočásticové klastry a dva typy agregátů, jeden termodynamického a druhý kinetického původu. Jednotlivé druhy agregátů se vyznačují odlišnými kinetikami vzniku a rozdílnými vlastnostmi jak mezi sebou, tak v porovnání s dispergovanými nanočásticemi. Pozorované typy disperze nanočástic byly kvantitativně posouzeny podle svých rheologických vlastností během roztokové přípravy, podle kterých byla vyhodnocena míra adsorpce polymeru na povrch nanočástic a atrakce ve vypuzeném objemu. Výsledky byly porovnány s teorií PRISM. Důležitost uspořádání nanočástic byla demonstrována na porovnání teplot skelných přechodů různých struktur při stejném chemickém složení.

## **KLÍČOVÁ SLOVA**

Polymerní nanokompozit, nanočástice, struktura, prostorové uspořádání, disperze, agregát, klastr, atrakce ve vypuzeném objemu, adsorpce, acidobazická interakce, roztokové míchání, rheologie, oscilační smyk s vysokou amplitudou (LAOS), transmisní elektronová mikroskopie (TEM), rentgenový rozptyl v ultra-malých úhlech (SAXS), polystyrene (PS), poly(methyl methakrylát) (PMMA), silika, polyhedrální oligomerní silsesquioxan (POSS)

*(Intentionally blank page)*

LEPCIO, P. *Effects of sub-micrometer structural features on rheology of polymer nanocomposites*. Brno: Brno University of Technology, Central European Institute of Technology (CEITEC), 2018. 94 p. Supervisor prof. RNDr. Josef Jancar, CSc.

## **DECLARATION**

I declare that the thesis has been composed entirely by myself and that all the quotations of the literary sources are accurate and complete. The presented results are the property of the Central European Institute of Technology of the Brno University of Technology and all commercial uses are allowed only if approved by both the supervisor and the director of the Central European Institute, BUT. The thesis includes copyrighted content which further use may require a permission from the copyright owner.

.....  
student's signature

## **ACKNOWLEDGMENTS**

I would like to thank my supervisor prof. RNDr. Josef Jančář, CSc. for his constructive supervision throughout the entire Ph.D. course. My deepest appreciation is addressed to my colleague Ing. František Ondreáš for the close collaboration on the topic, particularly on the structuring phenomena of polymer nanocomposites, with whom I shared experimental samples, results and wisdom. I also highly value the collaboration with Ing. Klára Zárybnická and Ing. Marek Zbončák. I am grateful for the assistance provided by my colleagues at the Central European Institute of Technology, especially for the SAXS measurements by Mgr. Ondřej Caha, Ph.D., the general instrumentation guidance by Ing. Radka Bálková, Ph.D. and the inspiring discussions with Ing. Jakub Sadílek. Part of the work was carried out with the support of CEITEC Nano Research Infrastructure (ID LM2015041, MEYS CR, 2016–2019), CEITEC Brno University of Technology. Many thanks to Ing. Ladislav Ilkovics and Dobromila Klemová from the Institute of histology and embryology at the Medical faculty of Masaryk University in Brno for the collaboration on the transmission electron microscopy. I would like to express special gratitude to Dr. Chris Holland for supervising me during the internship at the University of Sheffield, UK and guiding me on rheology and general science, Dr. Peter Laity for his valuable guidance and comments and Andreas Köppel for his aid. Finally, I thank my family and friends for the support during the period of the Ph.D. course.

*(Intentionally blank page)*

# 1. Content

1. Content .....	9
2. Introduction .....	10
3. State of the art .....	12
3.1. Structuring phenomena in polymer nanocomposites .....	12
3.1.1. Self-assembly in polymer nanocomposites .....	13
3.1.1.1. Steric stabilization and enthalpy of adsorption .....	13
3.1.1.2. Nanoparticle dispersion control .....	18
3.1.2. Force-assembled polymer nanocomposites .....	21
3.1.2.1. Shear force directed assembly .....	21
3.1.2.2. Magnetic field force assembly .....	22
3.1.2.3. Electric field force assembly .....	26
3.2. Properties of polymer nanocomposites .....	27
3.2.1. Thermomechanical properties .....	27
3.2.2. Rheological properties .....	33
3.2.2.1. Steady-flow rheology .....	33
3.2.2.2. Rheology under Oscillation .....	34
3.2.3. Electrical properties .....	37
3.2.4. Magnetic properties .....	38
3.2.5. Optical properties .....	39
3.2.6. Barrier properties .....	40
4. Aims of thesis .....	42
5. Methods .....	43
6. Results and discussion .....	47
6.1. POSS/PS model nanocomposites .....	47
6.2. Silica/PMMA nanocomposites .....	50
6.3. Silica/PS nanocomposites .....	67
7. Conclusions .....	72
8. References .....	74
9. Author's publication list .....	94

## 2. Introduction

Synthetic and natural polymers and composites are being increasingly utilized in fields ranging from aerospace to tissue engineering. A considerable scientific effort has recently focused on the enhancement of thermomechanical<sup>1–5</sup>, optical<sup>6–10</sup>, electromagnetic<sup>1,11–14</sup>, and barrier properties<sup>3,15–17</sup> of polymers by adding nanoparticles (NPs). The resulting material is usually referred to as a polymer nanocomposite (PNC), i.e., a composite with polymer matrix and one or more *nano*-structured components ( $\lesssim 100$  nm). The essential advantage of nanofillers is their large surface area which amplifies the surface effects which is responsible for the property enhancement. Wide range of properties could be modified by the introduction of relatively small amount of nanoparticles into a polymer matrix, and, thus PNCs can achieve properties comparable or even superior to conventional composites at extraordinary low filler loadings.

Polymer nanocomposites represent a promising and progressive field which could meet the recent challenges of the material development. Despite the unceasing progress in the development of conventional materials such as metals and ceramics, many scientists believe that the future of material engineering lies in novel *bottom-up* platforms for additive manufacturing. Besides their *eco-friendliness* and the capability to fabricate materials with advanced *physico-chemical* properties, these techniques can keep the processing relatively simple and highly customizable by adding *end-use specific* functions while minimizing the number of the required components. The only principal limitation of the *bottom-up* methods is the size of the primary building block which is used to build up larger objects. The elementary building blocks of PNCs are represented by polymer matrix and nanoparticles. If assembled in a specific geometrical manner, it allows for a synergistic gain in properties. Since any given property requires a specific NP organization, no single length scale NP spatial organization can optimize all macroscopic properties simultaneously. Hierarchical systems, on the other hand, could be adjusted to optimize processes and properties which originate at various length scales as it is often observed in natural materials like wood,<sup>18,19</sup> bone<sup>20–22</sup> or nacre,<sup>21,23</sup> which combine properties that are typically contradictory in artificial materials, such as a high stiffness and a high toughness. The tiny size of nanoparticles enables a fine tuning of the structure in several hierarchical levels when the assemblies become the building blocks of the next step. This way, the material is precisely built up from the *nano*- to the *macro*-scale with a complex structure over the whole length scale. However, despite the near perfection of the natural processes, the industrial application longs for a technique that would fabricate parts quicker than by the rate of a growing tree.

The spatial organization adjustment at the *nano*-scale has to solve the following limitations: (i) there is limited to no ability to manipulate nanoobjects directly and exclusively, (ii) mutual positions available to nanoobjects are severely constrained by thermodynamic potentials, and (iii) some thermodynamically stable structures could be kinetically inaccessible due to the presence of energetic wells and barriers unless an adequate preparation protocol is adopted. Hence, the NP spatial organization in an amorphous polymer results from a complicated interplay between the thermodynamically controlled NP organization in the liquid phase, mixing kinetics in the liquid nanocomposite and the kinetics of the liquid nanocomposite

vitrification. While significant progress has recently been made in the development of theories for predicting the equilibrium structure of the PNCs, there is a strong need to address the effects of processing and kinetic entrapment on the development of their structure.

In liquid polymer, NPs can assemble in three limiting structures – NP agglomerates, chain bound NP clusters or individually dispersed NPs<sup>24</sup>. At this point, the meaning of “aggregate” and “agglomerate” should be clarified since a widespread confusion exists with different authors and fields preferring various nomenclatures. The terms are often freely interchanged and the only mutual agreement is that both are related to assemblies of primary particles<sup>25</sup>. This work considers convenient to distinguish between these two terms; therefore, aggregate will be used for an arrangement of rigidly adjoining particles while agglomerate will mark a much looser and weaker assemblage, such as a flocculate. The distinguishing criteria is whether the particles can or cannot undergo a spontaneous rearrangement due to the thermal motion. NPs in aggregate interact directly with each other and the NP-NP attraction prevails all the interfacial interactions in the system. In the case of the chain bound clusters, particles are separated by polymer chains which mediate the NP-NP interaction while a single “bridging” chain adsorbs on multiple particles. Therefore, NP clusters behave as internally structured inclusions. Dispersion of individual NPs maximizes the NP-chain interfacial area per unit volume which results in the greatest extent of polymer affected by the particles. Segments of adsorbing chains are immobilized on the particle surface and frustrate the packing in their vicinity which is reflected in macroscopic deformation response. However, the course of the NP spatial organization through the transition between the equilibrium PNC liquid and the solid-state bulk material has not been fully understood yet. Answering the related questions might also boost other fields not typically considered as nanocomposites, e.g. additives and stabilizers for plastics. Meanwhile, the incomplete theoretical understanding did not stop PNCs to enter the worldwide market. Besides car tires which utilize carbon black reinforced rubber for decades, the range of nanocomposite components in automotive has been growing ever since its first application as step assists in 2002<sup>26</sup>.

The thesis reports on solution blending preparation protocols and the outcoming NP spatial organizations in a glass forming polymer. The structure control was achieved by changing the processing conditions, yielding either dispersed, agglomerated or clustered NPs which were fixed by the rapid solvent evaporation and remained kinetically stable through the consequent excessive thermal processing. The qualitative differences between the structural types manifested by their properties and formation kinetics were emphasized. Two types of aggregates were recognized, one of a kinetical and one of a thermodynamic origin, both dissimilar to what was identified as the chain bound clusters which supposedly emerged from a solvent mediated analogue of bridging predicted by the PRISM theory of Schweizer et al<sup>24</sup>. The structural information of the *submicro*-shaped PNC features was combined with their rheological behavior to provide novel experimental evidence on the NP ordering in model PNC systems.

### 3. State of the art

#### 3.1. Structuring phenomena in polymer nanocomposites

The field of particle dispersion in polymer nanocomposites can benefit from some well-established concepts of colloidal chemistry such as colloidal hard and soft spheres, DLVO theory, etc. Colloidal particles generally tend to stick closely together due to the attractive van der Waals forces unless their dispersion is stabilized by other forces. When considering nanoparticles, theoretical models should incorporate the NP atomic-scale surface patchiness to encompass the distribution of interaction potential between the nanoparticle surface and neighboring bodies<sup>27</sup>. However, the complex situation is often simplified by the 12-6 power law also known as the Lennard-Jones potential<sup>28</sup>. In the case of charged particles, the Coulomb repulsion can act as the stabilizing force as described by the DLVO theory. Moreover, hydrophilic repulsion and hydrophobic attraction may arise next to the electrostatic double layer and van der Waals interactions as additional forces between the hydrophobic and hydrophilic surfaces. This case is, however, beyond the scope of the DLVO model<sup>29</sup>. Steric repulsion is another stabilization effect and will be discussed in greater detail further in the text since it is particularly relevant to the PNCs. Other interactions can be induced in PNCs if the system is subjected to an external electric, magnetic or shear force field.

Particles can be either randomly dispersed in space or arranged in a regular pattern. Higher maximum concentration could be achieved in the latter case than in the former<sup>30</sup>. For monodisperse spheres in close packing, the theoretical maximum is  $\sim 0.74$  but higher values can be achieved for polydisperse or non-spherical particles. If dense packing of particles is favored, polyhedral specks incline to maximize their face-to-face contact, non-spherical smoothly shaped particles prefer contact at sites with lower principal curvature and non-centrosymmetric particles can exploit their rotational degrees of freedom<sup>31</sup>. In a polymer matrix, NPs can occupy one of the three basic spatial organizations – aggregated, clustered and dispersed NPs. Particles in aggregates lie in (near) contact with each other and the whole aggregate resembles one large particle. Despite the aggregated particles do not fuse together to yield a new particle with reduced surface like in the case of coalescence, some surface sites may be blocked<sup>28</sup> and the effective surface area – the surface available for interaction with polymer chains – is reduced.

Clusters are built up from particles bridged by adsorbed polymer chains, which mediate the interparticle interactions. They also seem to act as one independent entity but, unlike aggregates, clusters are principally two-level hierarchical systems where the higher level is represented by stiff inclusions in polymer matrix while the lower level encompasses both the NPs and the polymer chains. Finally, good dispersion of individual particles ensures that the whole NP surface is exposed to the polymer and the amount of affected matrix is maximized. Consequently, good dispersion usually exhibits the most pronounced change in properties<sup>32-34</sup> and is particularly favored in fundamental studies and optical applications. The structural impact on PNC material properties is described in the following chapter. Despite the enormous effort and the huge amount of published papers<sup>32,33,35-53</sup>, a reliable prediction of experimentally prepared dispersion states has not yet been fully achieved and the “*trial-error*”

approach still dominates many of the studies on the NP spatial organization in PNCs. It is not unanimously agreed which physical parameters govern the formation and properties of self-assembled nanoparticle-polymer structures.

### 3.1.1. Self-assembly in polymer nanocomposites

The *bottom-up* structure could be either derived simply due to favorable conditions, the so-called *self-assembly* (SA), or it could be aided with external forces, such as a shear or a magnetic field, which is commonly referred to as the *directed-assembly* or the *force-assembly* (FA). *Self-assembly* is a spontaneous process controlled by thermodynamic balance of enthalpy and entropy, and, if metastable structures are favored, by kinetics of the NP arrangement. There is only a limited number of fundamental structural organizations available for self-assembled PNCs. The control over the final morphology is achieved by shifting the thermodynamic equilibrium or altering the kinetic route of preparation. In contrast, external fields induce additional driving forces which might eventually become the dominant factor and take control over the assembly process, resulting in defined *nano-* and *micro-*structures.

#### 3.1.1.1. Steric stabilization and enthalpy of adsorption

Steric stabilization is induced by polymer chains attached to NP surface, either by the covalent bond or by the less permanent physical interaction, since the polymer shells repel each other on approach due to the gradually increasing entropic penalty of distorting chains. The effect is more pronounced for dense and rigid chains or charged shells, which are less favorable to entwine each other. The progress in SA of grafted NPs was reviewed in depth by Kumar, et al.<sup>54</sup> and only the highlights are recalled in this work. The long-range repulsion imposed by polymer grafts balances the short-range attraction of particle cores and allows for new structures to be formed. If grafts have the same chemical composition as matrix, all changes are driven by entropy and aggregates only occur when the molecular weight of the matrix exceeds that of the grafts<sup>55</sup>. Akcora, et al.<sup>56</sup> presented a phase diagram of uniformly grafted particles obtained by a Monte Carlo simulation (Fig. 1). Spherical aggregates of ungrafted particles are followed by sheets, strings and dispersed state as the length and/or the density of the grafts increases. The prediction is in perfect qualitative agreement with their experimental observations on polystyrene grafted silica nanoparticles embedded in polystyrene matrix<sup>56</sup> (Fig. 1).

If the polymer chains are not permanently attached to the particle surface by covalent bond, the enthalpy of chain adsorption onto the particle needs to be considered. The mechanism of polymer adsorption was investigated by Housmans, et al.<sup>57</sup> for polystyrene and silica in toluene and it apparently depends on the extent of the surface coverage of the particles. The approaching chains initially adsorb with high number of segments per chain and occupy flat conformations (trains) while the polymer layer grows linearly with time. Later, the incoming chains have to diffuse through the adsorbed layer and the growth switches to logarithmic regime once the diffusion slows down enough to become the dominant kinetic-controlling

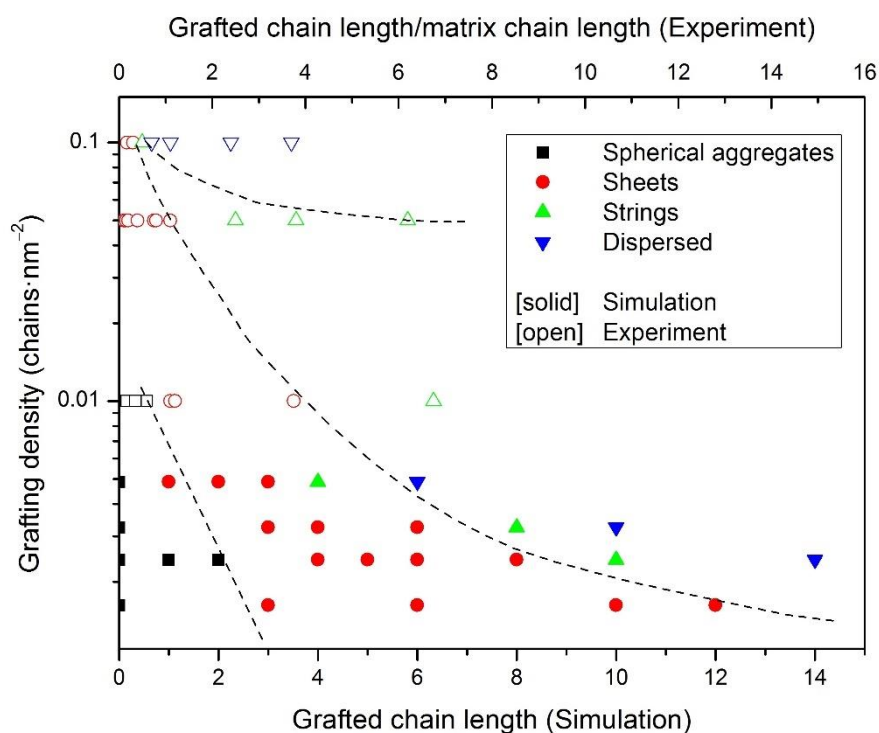


**Fig. 1:** Phase diagram of grafted particles based on a Monte Carlo simulation of uniformly grafted particles and experimental observations on grafted particles in polymer matrix. The dimensionless simulation data was recalculated to match the particle size from the experiment. The dashed lines serve only as guidelines for eyes. The data was acquired from the reference 56.

factor. The kinetics conforms to the equation of an Arrhenius-like thermally-activated process, which activation energy equal to  $(66 \pm 11)$  kJ·mol<sup>-1</sup> is comparable to that of other non-cooperative rearrangements in polystyrene. Polymer chains with purely-repulsive interaction to the filler were predicted by a MD simulation to occupy a perpendicular orientation to the surface while attractive interaction promotes tangent orientation at bond, segment and chain length scales<sup>58</sup>.

The coil dimension of an adsorbed chain can shrink, expand or retain its original size relative to the chains in bulk<sup>59,60</sup> and a theory on substantial conformational changes upon chain adsorption onto NP surface was proposed<sup>45</sup>. NMR experiments for silica-polyethylene glycol (PEG) nanocomposite revealed that the adsorbed polymer consists of segments with three degrees of mobility<sup>61</sup>. Closest to the NP surface, 1–2 segments in the direct contact form a rigid glassy layer which fraction is independent of the molecular weight and, for a given NP size, it scales accordingly with the particle concentration. Mobile segments distant more than one radius of gyration from the surface are, on the other hand, are not influenced by NPs and relax alike to the chains in the bulk polymer. Finally, there is a fraction of segments, presumably tails and loops in proximity to NP surface<sup>61</sup>, which are partially constrained, and their relaxation times take values intermediate to the two previous cases.

Patra and Singh applied a coarse-grain MD simulation to investigate the dispersion of monodisperse NPs assemblies in polymer melt<sup>55</sup>. Their phase diagram (Fig. 2A) shows a transition from the dispersed state to spherical aggregates similar to the one predicted for grafted particles by Akcora<sup>56</sup> (Fig. 1), except of the variables were the NP-polymer segment strength of attraction and the polymer molecular weight.

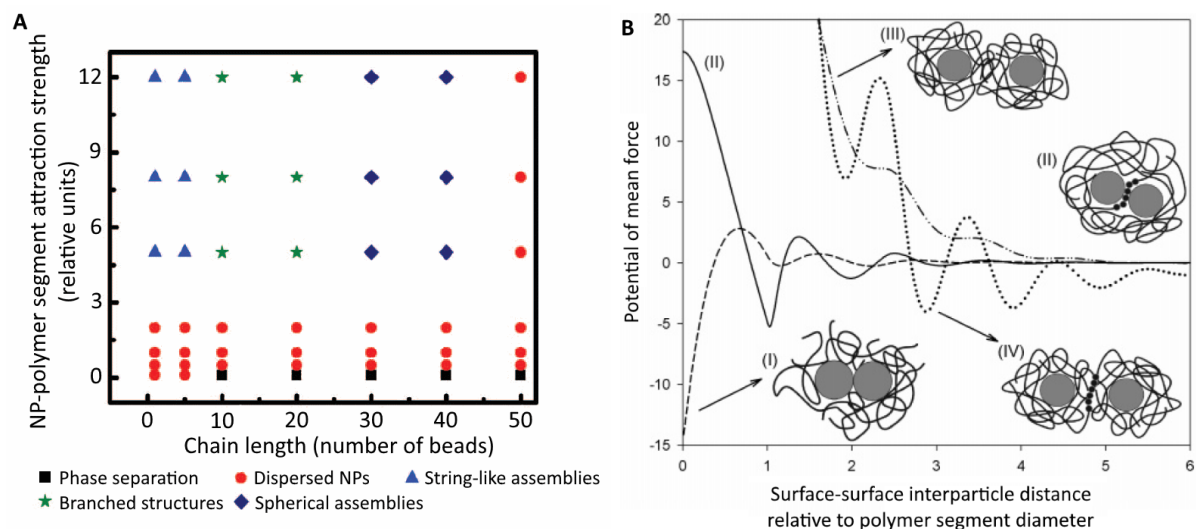


**Fig. 2: (A)** Phase diagram based on a coarse-grained molecular dynamics simulation of NPs in polymer melt. Reprinted with a permission from the ref. 55. Copyright 2013 AIP Publishing. **(B)** Particle-particle potential of mean force dependence on the interparticle distance relative to the polymer segment diameter according to the PRISM theory for representative examples of I. contact aggregation, II. bridging, III. dispersed state (steric stabilization), IV. telebridging. Reprinted with a permission from the ref. 24. Copyright 2006 American Chemical Society.

Mackay, et al.<sup>45</sup> appointed the governing role to a sole parameter represented by the particle radius to polymer gyration radius ratio. They proposed a qualitative model that good dispersion is obtained only when the particle radius is smaller than the polymer radius of gyration (Fig. 3). Hooper and Schweizer<sup>24,62–64</sup> applied the microscopic polymer reference interaction site model (PRISM) to predict the dispersion and the interparticle potential of mean force (PMF) for hard spheres in adsorbing homopolymer melt (Fig. 2B). They investigated several variables including the particle–monomer size ratio, degree of polymerization, interaction strength and spatial range of NP-polymer attraction and the direct particle–particle van der Waals attraction. Furthermore, they extended their original two-particle model<sup>62,63</sup> into many-body simulation in real space<sup>24,64</sup> to account for the filler volume fraction. Contrary to Mackay, et al.<sup>45</sup>, Hooper and Schweizer claimed only a moderate dependence of the structure on the particle-polymer size ratio attributing the major role to the strength of attraction between the NPs and the polymer.

Their model predicts an unfavorable chain adsorption onto particles at low polymer-NP interfacial energy and a contact aggregation induced by the consequent entropically-driven depletion attraction between the particles as the polymer chains keep off the NP surface. The

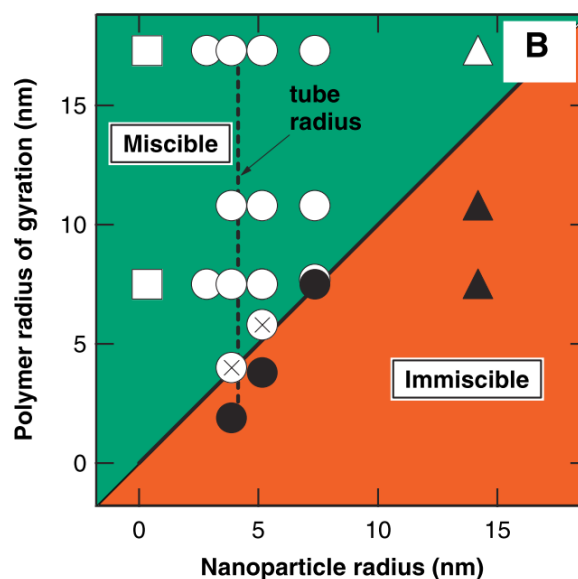


**Fig. 3:** Phase diagram of polymer nanocomposites. Solid symbols represent the phase separated systems while open symbols stand for the miscible ones. The cases with agglomeration detected by SANS but without large-scale phase separation are marked by open circles with a cross. Squares denote C<sub>60</sub>/PS nanocomposites, circles PS NPs/PS matrix nanocomposites, and triangles the dendritic PE/PS system. The filler content was 2 wt.% for all the presented data. Reprinted with a permission from the ref. 45. Copyright 2006 Science.

amplitude of the depletion force is proportional to the particle size and results in strong attraction even in the case of particles as small as 10 nm<sup>62</sup>. When the particle-chain interaction strengthens, the prospect of the polymer adsorption onto the particle increases and results into the dispersed sterically-stabilized state<sup>24</sup>. The situation is somewhat similar to the steric stabilization of grafted particles; however, it has to be stressed out that the role of enthalpy differs substantially. The enthalpic gain of the polymer adsorption gradually rises in importance upon the increasing polymer-NP interfacial strength until it eventually takes over and dominates the system while the dispersed structure is obtained. Hence, the transition from the dispersed to the aggregated state at low interfacial energies was identified as an enthalpically-driven phase separation.

For even stronger particle-chain attraction, a polymer induced NP bridging state emerges as a consequence of strongly adsorbed polymer layers onto the NPs. The corresponding enthalpic gain of the adsorption overwhelms the entropic loss of the chain conformational change connected with the polymer adsorption and the steric repulsion diminishes. Once already distorted, segments of this chain will preferentially adsorb onto another particle rather than a chain which has not paid the entropic penalty, yet. As a result, particles become bridged by polymer chains into clusters. In the clusters, the average interparticle separation of the nearest neighbors corresponds to one monomer diameter<sup>24</sup>. Therefore, the phase separation at strong NP-chain interaction is enthalpically dominated. Finally, *telebridging* is similar to bridging but occurs at longer interparticle distances when the spatial reach of the polymer-particle interaction favors presence of multiple layers of adsorbed chains between the bridged

particles<sup>24</sup>. Some of the modelled PMF contains multiple energy wells (Fig. 2B) which suggests that, for certain combination of parameters, the kinetic entrapment might give rise to thermodynamically metastable structures. For instance, Wang, et al.<sup>65</sup> studied adsorption of PEO onto silica NPs in water by dynamic light scattering (DLS) and isothermal titration calorimetry (ITC). They observed that the NPs tended to form pairs if the polymer was being dissolved in suspension of NPs in pure solvent (“NPs first”) while adding the NPs into PEO solution (“polymer first”) led to the dispersion of individual NPs.

Hooper and Schweizer transformed their results into phase diagrams constructed for various cases of the above-mentioned parameters. The NP-chain interaction strength  $\epsilon_{pc}$  and the particle volume fraction were the structural variables. A representative example is displayed in Fig. 4A showing that the miscibility region at medium NP-chain attraction narrows with increasing particle volume fraction. This is caused by rearrangement of the collective particle packing at the increased filler volume fraction, though these changes are rather quantitative than qualitative<sup>64</sup>. The miscibility region is also shrunk by the direct interparticle van der Waals attraction, particle shape asymmetry or longer polymer chains<sup>24</sup>. In all cases, the restricted miscibility promotes bridging while the phase separation at low interfacial attraction is less sensitive to the variation in structural parameters. The thermodynamic temperature  $T$  comes in play through the relative  $k_B T$  units of the thermal energy in the form of the  $\epsilon_{pc}/k_B T$  ratio, where  $k_B$  is the Boltzmann constant. Hence, the nanocomposite melt could be understood as a solution of NPs in a polymer melt with an entropically-driven lower critical temperature of phase separation and an enthalpically-driven upper critical temperature of phase separation<sup>24</sup>.

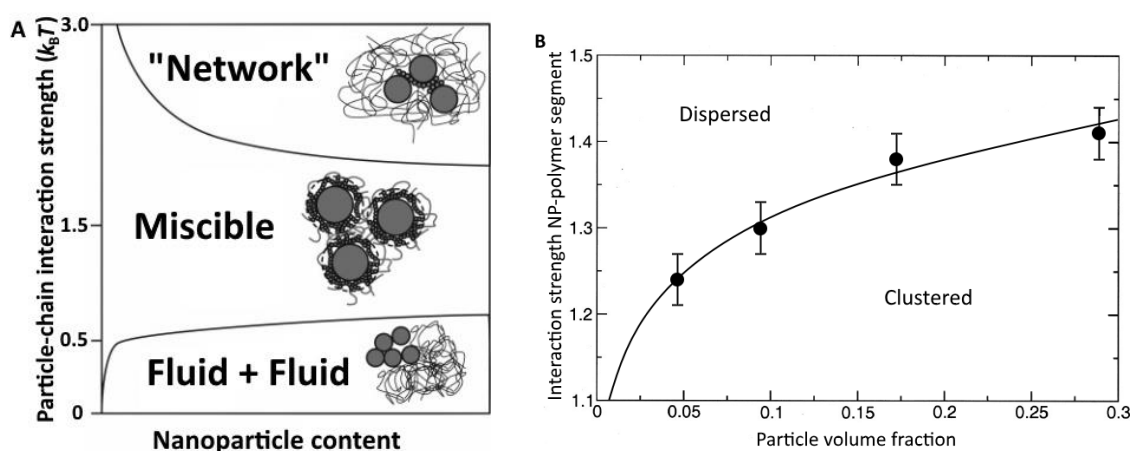


**Fig. 4:** Morphology diagrams of NPs in polymer matrix predicted by **(A)** PRISM theory (representative example). Reprinted with a permission from the ref. 64. Copyright 2007 American Chemical Society. **(B)** molecular dynamics simulation. Reprinted with a permission from the ref. 27. Copyright 2003 AIP Publishing.

The PRISM theory was successfully adopted by Zukoski, et al. to determine NP-polymer interaction strength by correlating experimental structure factors obtained from scattering measurements to the theoretical prediction<sup>51,53,61,66–71</sup>. The PRISM theory fitted well to their experimental observations in the limit of low molecular weight polymers ( $M_w < 1000$  for silica in polyethylene glycol) but fails for higher molecular weight polymers. The authors suggested

that it is caused by segments of the adsorbed chains not reaching equilibrium with the bulk polymer and proposed hypothesis that the NP organization states can eventually be reached after sufficiently long time. However, this hypothesis was not proved by successive experiments<sup>61</sup>.

Douglas and Starr performed a molecular dynamics simulation of the nanoparticle clustering<sup>27,72</sup> and proposed that the effect of polymer on nanoparticles can be represented simply with a long-range weak repulsion. According to their model, NPs phase separated in the absence of polymer, while in its presence, the NPs underwent a reversible self-assembly to form clusters at low temperature. At higher temperatures, the NPs remained dispersed except for high particle concentrations (Fig. 5A). The scaling of the critical cluster transition temperature  $T^*$  with the particle density  $\rho$ , i.e., the number of particles per unit volume, adapts reasonably well to a thermally activated process (Fig. 5B), according to the equation  $\rho = A \cdot \exp\left(\frac{-E}{k_B T^*}\right)$ , where  $A$ ,  $E$ , and  $k_B$  is a pre-exponential factor, enthalpy of NP association and the Boltzmann constant, respectively. By comparing the simulation (Fig. 4B) to the model of Hooper and Schweizer<sup>24,62–64</sup> (Fig. 4A), one can conclude that the phase diagrams from both studies agree qualitatively on the phase separation at low interaction strength while the reversible self-assembly predicted by Douglas and Starr is of entropic nature.

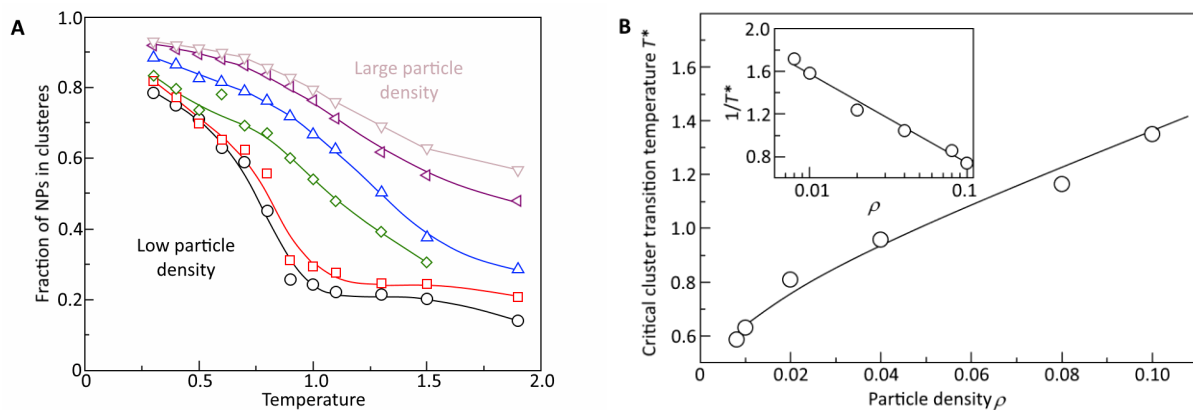


**Fig. 5: (A)** Critical cluster transition temperature dependence on the nanoparticle density **(B)** Fraction of nanoparticles as a function of temperature. All temperatures are provided as relative unitless values. Reprinted with a permission from the ref. 72. Copyright 2008 AIP Publishing.

### 3.1.1.2. Nanoparticle dispersion control

Currently, there are several techniques for PNC fabrication but all struggle to ensure the desired dispersion of the nanofiller in the polymer matrix. The formation of the NP arrangement is typically carried out in a liquid phase since the related processes are kinetically hindered in the solid state, keeping the internal structure relatively stable over extended periods of time. Melt and solution blending are preferred and most common for thermoplastic PNCs. Other techniques cover *in-situ* chemical reactions such as polymerization<sup>14,73,74</sup>, particle synthesis<sup>75,76</sup> or combination of both<sup>77</sup>. These approaches also benefit from the low viscosity of the dispersing medium and the related effects. However, nanoparticles can alter the

polymerization kinetics, making it somewhat troublesome to determine the properties of the neat matrix, to which are the properties of PNCs always related. Particles with multiple reactive chemical moieties directly enter the polymerization reaction similarly to conventional cross-linkers (increased  $T_g$  and stiffness)<sup>78–80</sup> while inert particles act as heterogeneous catalysers. Therefore, one can conclude that these systems do not suit the needs of the fundamental investigation, though many applications might find them convenient. Other, more exotic techniques, have been developed for special applications such as the production of carbon-nanocomposite silk by feeding silk worms with carbon nanoparticles<sup>81</sup> or filling a nanostructured crab shell<sup>82</sup> and wood template<sup>83</sup> with synthetic polymer matrix.

In general, it is difficult to obtain a good dispersion when nanoparticle powder is added to polymer melt<sup>84–90</sup>. Nanoparticles are commonly aggregated in dry state and they often do not fully disperse even under extreme shear forces. Solution blending, on the other hand, allows for nanoparticle predispersion and colloidal-like solvation and stabilization effects to take place. Solvent also dilutes all interactions including the interparticle attraction<sup>51</sup>, low viscosity compared to melts enhances the formation kinetics, and the solvent composition could be used as a convenient tuning parameter<sup>50</sup>. NP-polymer assemblies occur in polymer nanocomposite solutions if the NP's affinity to polymer is superior to the affinity between the NPs and the solvent<sup>91</sup>. Solution blending, however, brings on a major drawback represented by the need to remove the solvent after the desired dispersion state is achieved. Evaporation rate enters the structuring phenomenon as a kinetic factor, since the post-processing of solution-casted solid-state samples does not critically impact the dispersion initially obtained after the drying<sup>50</sup>. The solvation stabilization by electrostatic repulsion diminishes upon the solvent removal and is replaced by the kinetic stabilization due to the increasing viscosity and restricted NP diffusion; therefore, a slow evaporation rate promotes aggregation<sup>50,92</sup>.

Jouault, et al.<sup>47,48</sup> reported unexpectedly low structural variation between a strongly interacting PMMA matrix and weakly interacting PS matrix in nanosilica-based composites. They ascribed the decisive role for morphogenesis to the choice of solvent and the shear field applied during the mixing step. In further research, Jouault, et al.<sup>50</sup> provided experimental evidence for the spatial distribution of PNCs controlled by altering the effective interaction strength through the choice of solvent. Solvent molecules can either favor the polymer-depletion attraction and induce aggregation, or they can enhance the polymer adsorption and, thus, the interparticle steric repulsion resulting in a good dispersion (Fig. 6). In the latter case, the adsorbed layer thickness was determined by dynamic light scattering (DLS) to be close to the radius of gyration  $R_G$  of the neat polymer. Zhao et al.<sup>36</sup> proposed the relative interaction strength between the particle-solvent, and the particle-polymer as the key forces which drive the formation of the bound polymer layer. It has to be noted that in the presence of solvent, the interaction sites on both the NP and the polymer are presumably occupied by adsorbed solvent molecules, which have to desorb prior the polymer-NP adsorption to free the active sites. The energy of the ceasing polymer-solvent and NP-solvent interactions has to be subtracted from the newly formed NP-polymer and solvent-solvent interaction energies to yield the total energetical difference of the NP-polymer adsorption in nanocomposite solution.

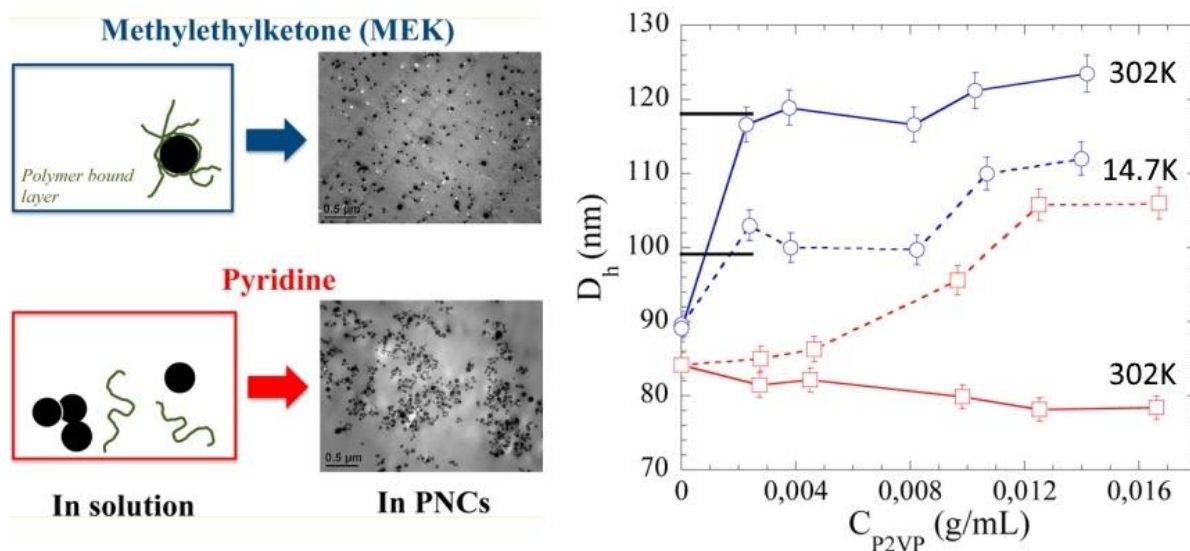


**Fig. 6:** Schematic interpretation of particle-polymer state in (blue) methylethylketone and (red) pyridine for 40–50 nm bare silica in poly(2-vinylpyridine) (P2VP). Hydrodynamic diameter  $D_h$  as a function of P2VP concentration for 14.7 kg·mol<sup>-1</sup> (dashed lines) and 302 kg·mol<sup>-1</sup> (solid lines) P2VP. Black lines indicate the value of nanoparticle diameter increased by  $2R_G$ . Reprinted with a permission from the ref. 50. Copyright 2014 American Chemical Society.

A polymer layer adsorbed on a nanoparticle may be desorbed by modification of the solvent composition with a co-solvent, the so-called displacer, which affinity to the particle exceeds that of the polymer<sup>93</sup>. The work of adhesion calculated from the critical concentration of the co-solvent required for the total polymer desorption does not necessarily reaches the same order as that for monomers/segments since segments experience different number of specific interactions per unit area. In order to investigate solvation effects, Zukoski, et al.<sup>51</sup> tested silica-PEG nanocomposite in water and ethanol at  $\Theta$  and non- $\Theta$  temperatures and concluded, that the NP dispersion is not explicitly related to the solvent quality regarding the polymer  $\Theta$  state. Clearly, the role of solvent in NP assembly goes beyond its solvation impact on the dissolved polymer and is likely directly involved in the NP assembly.

Another strategy to tailor the dispersion state is to tune the interface interaction strength through nanoparticle surface modification<sup>33,43,69,94–96</sup>. Native silica surface is amphoteric, but interacts preferentially with the basic moieties of the adsorbent through its acidic hydroxyl groups, because they can achieve optimal orientation to the incoming adsorbent<sup>93</sup>. Zukoski, et al.<sup>69</sup> silanized silica NPs to replace the surface hydroxyls with isobutyl groups, rendering the NPs more hydrophobic. They expected to reduce the amount of hydrogen bonding between the NPs and the polymer, and, thus, the interaction strength with the extent of surface treatment. However, the interaction strength was not assessed directly but estimated by comparing the experimental structure factors to the PRISM simulations. These correlated structure factors revealed that the apparent interaction strength indeed decreased initially with the increasing extent of silanization but later recovered as the silanization progressed. They concluded that there has to be an additional parameter not captured by the PRISM

model. However, experiments using a range of solvents revealed that the specific interactions, such as polar forces and hydrogen bonding, did not account for more than half of the adhesion work<sup>93</sup>. The largest contribution was from the dispersive interaction arising from the London's part of van der Waals forces. Therefore, other factors beyond the hydrogen bonding shall be considered when evaluating the NP-polymer interaction strength.

### 3.1.2. Force-assembled polymer nanocomposites

Fabrication of complex structures can take advantage of an external force field to assist the arrangement of NPs in a manner, which would not be obtained by simple self-assembly. Tailored assemblies can improve the mechanical properties, conductivity and thermal expansion of PNCs or tune other functional properties of the composite. The force-assembly (also referred to as directed assembly) approaches create highly anisotropic structures with regular NP spacing, controlled orientation and dimension tunable over wide length scales.

#### 3.1.2.1. Shear force directed assembly

Shear is the easiest realized external force field which affects the particle arrangement. A melt-blending processing technique is a simple example. Both polymers and coagulated or flocculated particles show non-linear features under shear coupled with internal structural changes. However, the role of the shear on structuring the PNCs is often rather a kinetic aid to the self-assembly than a genuine shear-induced force assembly. The external agitation assists the diffusional process to reach the thermodynamic equilibrium state. This effect is particularly pronounced in viscous polymer melts. Two size-dependent diffusivity modes have been predicted for a nanoparticle in weakly interacting entangled polymer melts. The first considers that NPs smaller than polymer entanglement mesh size are subjected to the local Rouse dynamics of the chains. The second assumes that the diffusion of larger NPs is slowed down by chain entanglements and fails to conform the Stokes-Einstein equation<sup>97</sup>.

Unlike simple liquids dominated by the short-range forces, the viscoelasticity of polymer melts and concentrated solutions is governed by the long-range interactions with long relaxation times arising from the soft-sphere-like contacts between the deformed polymer chains<sup>98</sup>. These contacts could only withstand relatively small deformations and they disrupt readily under loading. The distortion of polymeric chains under deformation is followed by their relaxation<sup>99</sup> and structural transformations result from the complex interplay of the formation and the destruction of the structural domains. The rates of both processes are exponential system-specific functions of the shear stress and their ratio determines the structuring ability of the system. Superior formation rate promotes shear thickening which corresponds with enhanced internal interactions and the creation of new structural features. Dominant destruction rate, on the other hand, fosters disruption of the structures and improves the dispersion<sup>100,101</sup>. Computer simulations suggest that the shearing favors dispersion of NPs due to the presence of the additional force which disrupts the aggregated particles<sup>27,102,103</sup>. In melt-blended PNCs, a combination of an excessive shearing by a twin-screw extruder and a favorable chemical composition is typically required in order to improve the NP dispersion. Nevertheless, a genuine dispersion of individual NPs in entangled polymer matrices seems to

be accessible only in some systems and at relatively low filler loadings<sup>43,84–90</sup>. As an additional effect, shearing induces orientation of dilute non-spherical particles with rotational symmetry by minimizing their rotational energy under the shear. This effect is blocked at semi-concentrated regime by mutual hydrodynamic interactions and sheared particles maintain a random distribution of orientations<sup>104</sup>. However, high aspect ratio particles without a rotational symmetry preserve a chaotic unoriented motion even under shearing<sup>104</sup>.

### 3.1.2.2. Magnetic field force assembly

An external magnetic field induces magnetization in a magnetically responsive species, e.g. Co, Fe, Ni, Fe<sub>3</sub>O<sub>4</sub> or Fe<sub>2</sub>O<sub>3</sub> particles and their ferro- or magnetofluids, which are the most commonly reported substances in such experiments. The magnetic force is proportional to the magnetic moment induced by the external field, hence, the ability to control the intensity of the magnetic field provides an opportunity to fine tune the ordering of NPs. Magnetic fields of moderate strength in the range of several mT commonly suffice to force the assembly of NPs but can vary from system to system depending on viscosity of medium, particle shape and energy of the thermal motion<sup>105</sup>. These fields can easily be generated by standard electromagnets (in AC, DC or pulse regime) or permanent magnets.

A single magnetically responsive particle tends to align its magnetic moment with the orientation of the external magnetic field. Orientation of non-magnetic particles requires attachment of magnetically active species on their surface to render them magnetically responsive<sup>106–108</sup> or by dispersing them in magnetized ferrofluids where non-magnetic particles act as magnetic holes, and thus develop a magnetic moment resulting from the ferrofluid imbalance<sup>109,110</sup>. In the presence of multiple particles, dipole-dipole interactions give rise to either interparticle attraction or repulsion depending on the mutual position of the particles and the orientation of their magnetic moments<sup>111</sup> (Fig. 7A). For illustration, if magnetic moments of two monodisperse spherical particles are aligned in the same direction due to an external magnetic field, the interaction turns from repulsive to attractive when the angle between the center-center position vector and the magnetic moment vector becomes less than 54°<sup>112</sup>. In non-uniform fields, particle is subjected to magnetic force which acts in the direction of the magnetic gradient and results into a magnetophoretic flow – a translational and/or rotational motion which is modified by the resistance of the surrounding environment<sup>113</sup>. The gradient could be utilized as a control parameter of magnetic assembly. Ghosh, et al.<sup>114</sup> prepared filaments of magnetic nanoparticles on a substrate through magnetophoresis by applying a small gradient of magnetic field while a large gradient caused a formation of a uniform coating.

Some magnetic particles can spontaneously self-assemble due to their dipole-dipole interactions even without the aid of an external magnetic field. However, a magnetic field can enhance the extent of assembly and modify the resulting morphology<sup>115</sup>. Magnetic force assembly of nanoparticles in liquid polymer matrix is an approach capable to fabricate structures<sup>116–120</sup> with prescribed orientation, tailoring mechanical<sup>121–124</sup> and functional properties such as optical<sup>109,125</sup>, electrical<sup>126</sup> or magnetic<sup>117,127</sup>.

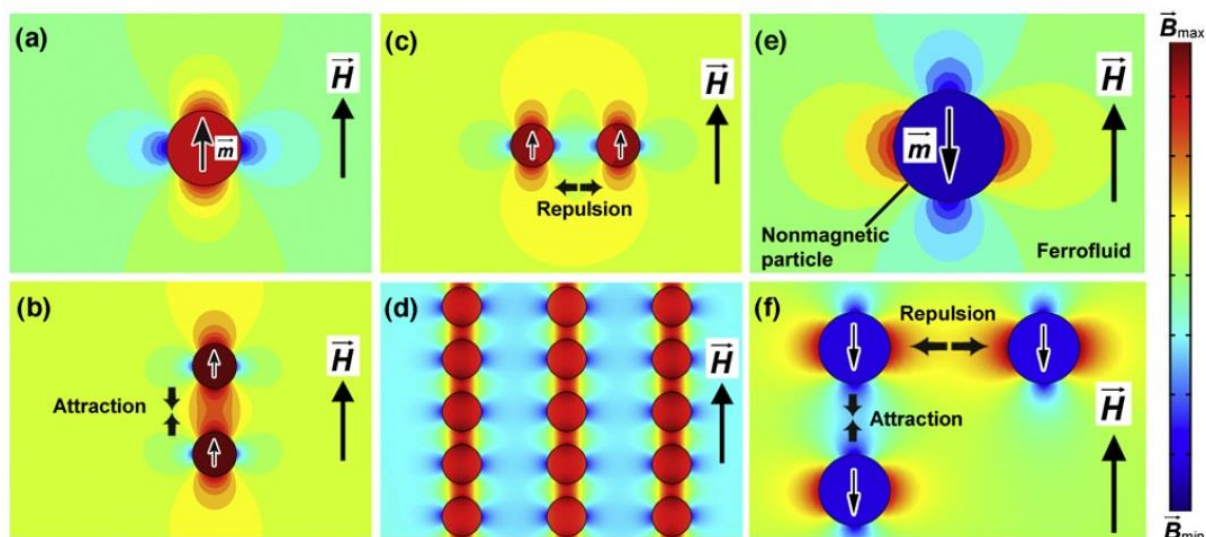


**Fig. 7:** (A) Magnetic field distribution around a superparamagnetic particle with a dipole moment in the same direction as the external magnetic field. The repulsive (B) and attractive (C) dipole–dipole forces in different particle configurations drive the formation of chains along the magnetic field (D). (E) Magnetic field distribution around a nonmagnetic particle with a dipole moment in the opposite direction of the external magnetic field. (F) The interparticle dipole–dipole interaction is either repulsive or attractive, depending on the particle configuration. Reprinted with a permission from the ref. 111. Copyright 2013 Elsevier.

Various analytical methods have been employed to study the kinetics of the magnetic force assembly, which is much quicker than self-assembly in polymer melt but still a relatively slow kinetically controlled process<sup>117,118,128</sup>. The most straight-forward of these techniques is a direct microscopic observation of the growing structures<sup>118,128–132</sup> but the results are limited by the resolution of the microscope used. Post synthesis analysis could also prove helpful, if system solidification time and the time of the field application are known<sup>117</sup>. Some researchers applied small-angle light scattering<sup>133–135</sup>, X-ray scattering<sup>124</sup> or magnetorheology<sup>119,130,136–139</sup> which measures kinetics through the rheological changes accompanying the magnetic assembly process. However, despite the vast number of available studies, there is no experimentally verified theory which would unite all the controlling parameters, time and structural relationships, able to predict the morphology solely from the input parameters.

Besides the magnetic force, the initial particle packing and the interparticle distances are other variables which play a role in the structure of the resulting NP assemblies. Careful choice of these driving parameters combined with the van der Waals forces determines a subtle balance of attractive and repulsive forces within the system (Fig. 8) which gives rise to the formation of fine 1D, 2D or 3D super-lattice structures<sup>128</sup>. The most commonly reported outcome of NP magnetic assembly is a formation of one dimensional particle arrays – strings<sup>130,140–149</sup> (Fig. 9A). The driving force responsible for the orientation is the interparticle attraction while repulsive interactions keep particles in single strings separated from the surrounding arrays. (Fig. 7B–E) The orientation of strings is guided by the direction of the external field while their width depends strongly on the quality of dispersion in the initial colloidal solution<sup>150</sup>. One- or

few-particle wide arrays are formed only if a perfect dispersion precedes the magnetic assembly step<sup>109,125,151</sup>. In contrary, particle aggregates originate from an imperfect dispersion states replacing single particles as the individual assembly building blocks during the magnetic manipulation. In fact, these 1D structures are in most cases rather elongated aggregates with a controlled orientation than genuine single-particle wide strings in most of the reported cases.

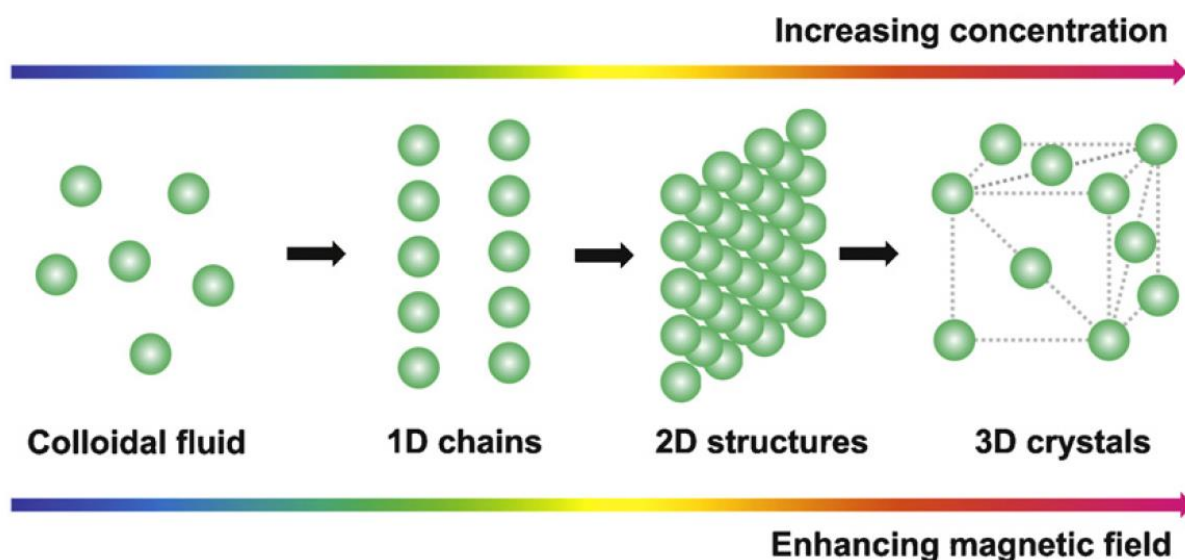


**Fig. 8.** Schematic illustration of magnetically induced phase transition between colloidal fluids, 1D chain-like, 2D sheet-like and 3D structures. Reprinted with a permission from the ref. 112. Copyright 2013 Elsevier.

The balance of 1D structures is easily disrupted, e.g. at higher particle concentration or at elevated magnetic field strength, and turns the arrays into higher-dimensional ensembles<sup>73,112,152</sup>. The repulsive forces which stabilize one-dimensional strings are overcome by attractive forces between neighboring arrays which shift closer to each other and merge into a single 2D structure (Fig. 9B) with regular ordering due to the dipolar interactions<sup>153</sup>. However, the 2D patterns seem to be a quite rare transitional state<sup>111</sup> and their desintegration continues to yield 3D structures (Fig. 9B) by stacking the 2D planes in a single super-lattice, which still respects the dipolar interparticle interactions<sup>154–156</sup>.

Hynninen and Djisktra<sup>157</sup> calculated a phase diagram of dipolar hard and soft spheres which matched well the experimental observation of Yethiraj and Blaaderen<sup>158</sup> and revealed a formation of bulk HCP, BCT and BCO lattices under the external magnetic field. A shape anisotropy may give a rise to more complicated structures as will be demonstrated in the following examples. A lattice can convert from FCC to triclinic when magnetically assembled  $\text{Fe}_2\text{O}_3$  nanospheres are replaced with ellipsoids<sup>154</sup>. Panda, et al.<sup>129</sup> observed that introduction of H-shaped particles causes 1D strings of magnetically assembled rods to show an increased tendency of chain widening and branching. Tang, et al.<sup>115</sup> assembled maghemite ( $\text{Fe}_3\text{O}_4$ ) nanocrystals of an elongated rice-like shape into “walnut” structures in absence of an external

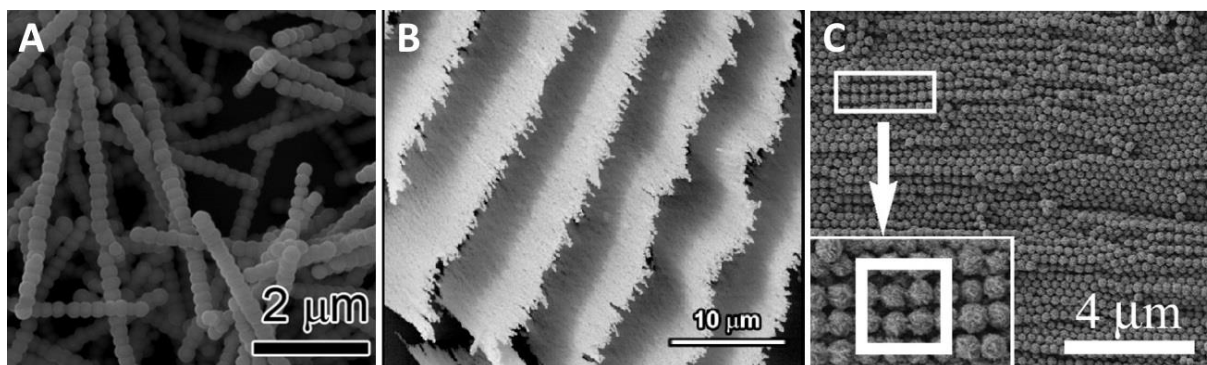


**Fig. 9:** Experimental examples of magnetically assembled **(A)** 1D strings. Reprinted with a permission from the ref. 112. Copyright 2013 Elsevier. **(B)** 2D sheets. Reprinted with a permission from the ref. 73. Copyright 2013 American Chemical Society. **(C)** 3D structures. Reprinted with a permission from the ref. 115. Copyright 2015 Elsevier.

magnetic field. These walnuts could be organized by an external magnetic field (0.2–0.3 T) into the hexagonal packing and form cylinders; however, a stronger magnetic field (> 0.4 T) disrupts the original walnuts and yields 1D strings of primary particles.

Crystalline particles often exhibit complex shapes due to their crystalline structure. Their magnetic properties differ between various crystallographic axes and some planes, the so-called *easy axes*, might be magnetized more easily than others – the hard axes. A magnetization of a crystalline particle along the preferred crystallographic planes is referred to as a magnetocrystalline anisotropy<sup>159,160</sup> and it determines the position of the particle magnetic poles<sup>161</sup>. If such anisotropic particle is free to rotate within its medium, it aligns its easy axis parallel with the external magnetic field<sup>129</sup>. For example, cubic  $\text{Fe}_3\text{O}_4$  particles preferentially align in the [111] direction<sup>161</sup>.

When the stabilizing factor of an external magnetic field is removed, the stability of magnetically assembled structures depends on the viscosity of the medium and the particle remanent magnetization. These two variables determine whether the strength of the interparticle dipolar magnetic forces suffices to prevent the structure from a collapse by diffusion and thermal motion. The ensembles are disordered easily in the case of (super)paramagnetism or low remanent magnetization while it may require elevated temperatures and/or prolonged time to disrupt arrays where the remanent magnetization is high<sup>116,162,163</sup>. The necessity to maintain an external magnetic field in order to prevent the structural changes led to several designs how to stabilize the arrays, for example a stabilization via a chemical reaction on the surface of particles which interconnects the particles by reaction products (e.g. oxides, sulfides, etc.)<sup>144,147</sup>, a stabilization via an interconnection of particles by polymer layer<sup>110,116,125,151,164</sup> or a solidification (a liquid-to-solid transition) performed as a polymerization or a solvent evaporation<sup>117,121–124,165</sup>.

### 3.1.2.3. Electric field force assembly

Though electric assembly techniques of particles are intensively studied by colloidal science<sup>166–168</sup>, publications on their application in the field of polymer nanocomposites remain scarce. In principle, the electric assembly is similar to its magnetic counterpart with the only difference being the type of the applied field. However, the essence of these two fields differ – an electric field is a source field while a magnetic field is a vortex field. Additionally, an assembly by a magnetic force requires particles to bear a non-zero magnetic moment while an electric moment can be induced even in non-polar molecules when their electron shells are distorted, and they become polarized. In the case of conductive particles, such as carbon nanotubes, metallic particles, etc., the response to an electric field is dominated by the surface charge which gives rise to an electrophoretic force<sup>169</sup>. A dielectrophoretic force originates from the mismatch of complex dielectric permittivity between the matrix and the NPs. Therefore, unlike a shear field, electric forces can cause an active migration of nanoparticles in the direction lateral to the field orientation and intrinsically change the structure of an assembly<sup>13</sup>. Hence, structural organization of an electric assembly is achieved by the combined contribution of polarization, dipole-dipole moments, electrophoresis, dielectrophoresis and the Coulombic attraction<sup>13,170</sup>.

The parameters of an electric field have a direct impact on the NP assembly. A typical field strength in experimental studies lies around tens of  $\text{V}\cdot\text{mm}^{-1}$ . An increasing intensity of an electric field enhances the particle orientation of the equilibrium state up to a saturation limit when all the particles become oriented<sup>171</sup>. A further strengthening of the electric field quickens the kinetics and decreases the time to equilibrium but causes no additional change to the structural ordering (within the range of the investigated field strengths<sup>171</sup>). The reason is that the torque induced by the an electric force is opposed by a viscous drag while the alignment of particles is being distorted by the Brownian motion<sup>14,74</sup>. Accordingly, long carbon nanotubes (CNT) were reported to orient more easily in an electric field than short ones due to their larger dipole moments<sup>172</sup>.

Colloidal particles in a liquid medium typically show a complex frequency dependence on the electric polarizability<sup>168</sup>; however, the effect can practically diminish when particles are immersed in a viscous medium<sup>171,173</sup>. In general, the use of an AC electric field avoids the electroosmosis and the electrochemical effects induced by a DC<sup>166</sup>. Hence, AC fields seem to produce more uniform structures<sup>174</sup>. An example can be found in the work of Nihara, et al. who reported an electric field-type control of the PNC structure<sup>170,175,176</sup>. Furthermore, they fabricated linear bridge-like assemblies of boron nitride nanosheets in polysiloxane by choosing an electrode with periodically varied intensity of an electric field near its surface<sup>175</sup>. Park, et al.<sup>13</sup> reported that at very low frequencies, a dielectrophoretic force aligning carbon nanotubes (CNTs) is weaker than the combination of the Brownian motion and the electrophoretic force, which prevents and/or disrupts the nanoparticle alignment. Above 1 Hz, the effect of electrophoresis is reduced and the dielectrophoretic force becomes the dominant factor, saturating above 100 Hz. However, a further increase in the frequency seems to disrupt the nanoparticle alignment. As expected, oriented nanoparticles exhibit a lower concentration threshold of the percolation than randomly dispersed ones<sup>13,74</sup>.

## 3.2. Properties of polymer nanocomposites

### 3.2.1. Thermomechanical properties

In general, introduction of nanoparticles into a polymer matrix results in a nontrivial alteration of its thermomechanical behavior<sup>177–182</sup>. NPs modify the chain dynamics and the molecular packing of the matrix on various time and length scales; moreover, anisotropic composite structures such as magnetically assembled 1D strings are coupled with strong anisotropy of mechanical properties in both micro-<sup>121,122,183</sup> and nanocomposites<sup>123,124</sup> and typically exhibit a significant enhancement of the stiffness and strength in the direction parallel to the NP alignment. However, science has yet to fill numerous gaps in the fundamental description of the interconnection between the nanostructure and the macroscopic mechanical response of hierarchical NP assemblies. A part which is particularly poorly understood is the transition between the nano- and microscale models.

Stiff inorganic particles induce various effects on the stiffness, toughness and yield properties of polymers, which are, in the case of PNCs, strongly dependent on the spatial organization of NPs. Regarding the stiffness, micro-composites benefit from the well-known reinforcing mechanisms of the volume replacement and stress transfer. The former is a consequence of a partial substitution of the soft matrix by rigid particles and the latter refers to a situation when the loading stress is being transferred from the matrix to the reinforcing phase of a non-spherical shape due to the elastic modulus difference between the soft matrix and the rigid reinforcement. However, experimental results of Jouault, et al.<sup>47–49</sup> on silica/PS nanospheres above the percolation threshold (about 7.5 vol. % of silica) failed to meet the prediction of the simple volume replacement model by Guth-Smallwood though the same model provided a reasonable fit for microsilica/PMMA samples (Fig. 10A)<sup>48</sup>. Jancar and Recman<sup>184</sup> demonstrated that a particle size reduction from the micro- to the nanoscale leads to a pronounced enhancement of thermomechanical properties which could not be explained by any conventional microcomposite model (Fig. 11). It suggests that an additional, specific surface area dependent reinforcing mechanism exists in PNCs. Its contribution is negligible above a certain critical particle size, which is commonly agreed to be approximately 50–100 nm<sup>185</sup> while becoming dominant below this threshold size. This value corresponds to a threshold length scale at which nanoscale heterogeneities smear out and become negligible<sup>55</sup>. Above this limit, conventional fillers typically act as a reinforcement whereas smaller particles can either reinforce or plasticize polymer matrix regarding to their chemical nature<sup>186</sup>. In contrast with volume replacement and the stress transfer mechanism, experimental data suggests that the shape of NPs plays only a minor direct role on the mechanical reinforcement of polymers, because the nanoparticle dimensions lie far below the critical stress-transfer length, and the dominant role is ascribed to the filler specific surface area<sup>187</sup>, except of unidirectionally aligned fibrous or platelet shaped NPs.

The first recognition of the nano-reinforcement is traced back to Payne and his experiments on rubbers filled with carbon black<sup>177,178</sup>. A dynamic analysis on these samples revealed a drop of the elastic modulus in the rubber phase when subjected to an oscillatory loading with an

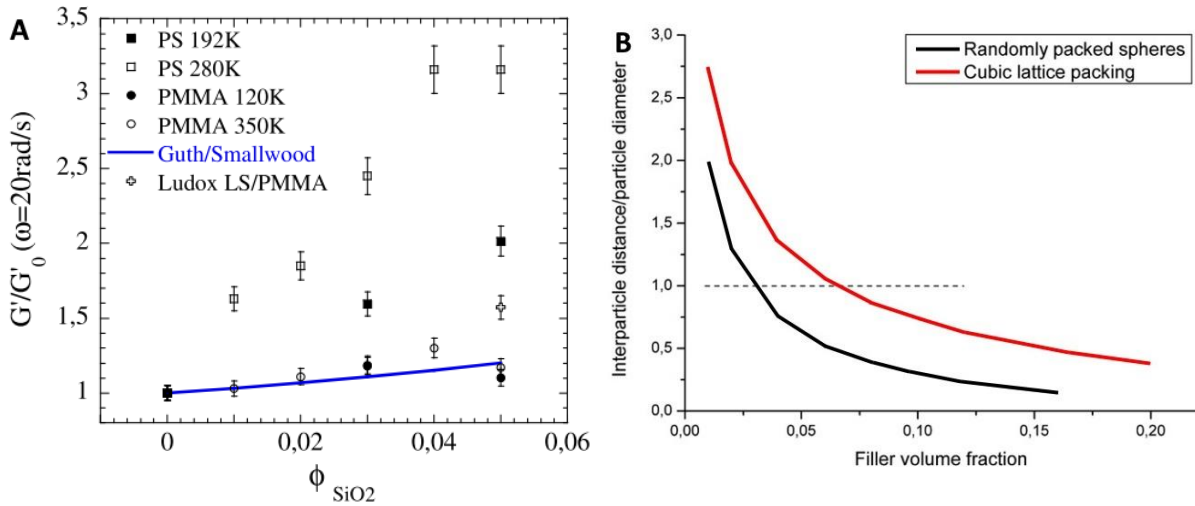


**Fig. 10: (A)** Comparison of relative plateau moduli of nanocomposites Nissan-St (5.9 nm)/PS (192 kg·mol<sup>-1</sup>, and 280 kg·mol<sup>-1</sup>) and Nissan-St (5.9 nm)/PMMA (120 kg·mol<sup>-1</sup>, and 350 kg·mol<sup>-1</sup>) with theoretical volume replacement based prediction of Guth-Smallwood model. Reprinted with a permission from the ref. 48. Copyright 2012 Elsevier. **(B)** Interparticle distance to particle diameter ratio dependence on filler volume fraction according to 1000 monodisperse spherical particles with (blue) random distribution and (red) cubic lattice packing. Reprinted with a permission from the ref. 188. Copyright 2012 Elsevier.

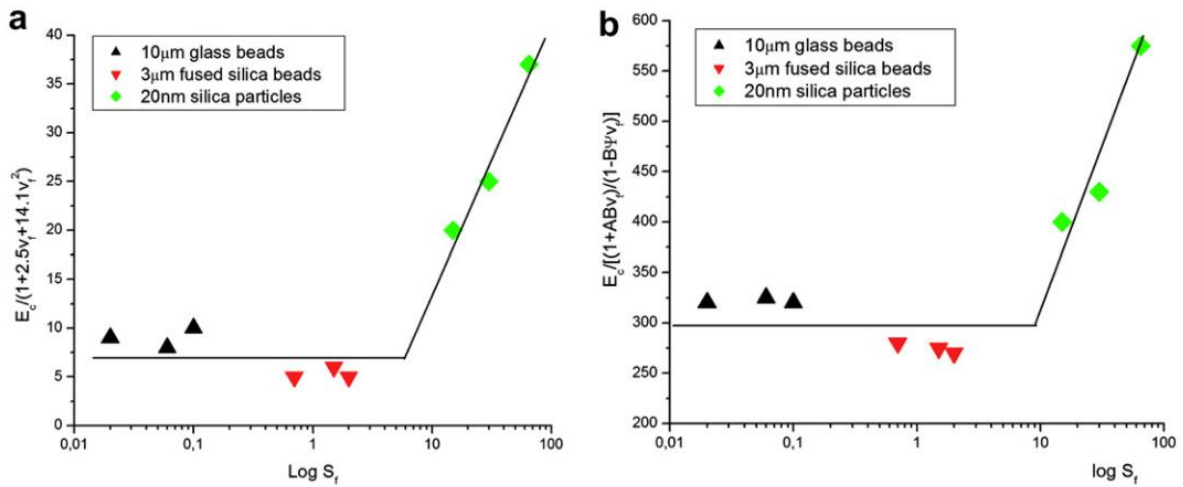


**Fig. 11:** Dependence of the matrix modulus  $M_m^* = \frac{E_c}{f(v_f)}$  on the logarithm of the specific interface area ( $S_f$ ) (A) above  $T_g$  using the Guth model and (B) below  $T_g$  using the Kerner-Nielsen model. Reprinted with a permission from the ref. 184. Copyright 2010 Elsevier.

increasing strain which was not native to unfilled rubbers. This feature of strain softening, which is now known as the Payne effect, was substantially weakened in the successive runs of a strain sweep measurement but it eventually recovered given sufficient time after the straining. Payne attributed the effect to a breakdown of the filler structure within the samples, but his suggestion was contradicted by additional evidence. Cassagnau<sup>88</sup> found the Payne

effect even in EVAc/silica samples below the percolation threshold which violates the network breakdown theory and he proposed a chain disentanglement as the driving mechanism of the Payne effect. The same study also reports the Payne effect in systems with unentangled low molecular weight matrices. Hence, Cassagnau suggested that the disentanglement and the structure breakdown are two alternative mechanisms responsible for the Payne effect. Kalfus and Jancar<sup>187</sup> studied shifts in the onset and the intensity of the Payne effect on PVAc/hydroxyapatite and observed that it is more pronounced for low molecular weight matrices and at higher temperatures. Based on their modulus recovery experiments, they concluded that the immobilized layer around NPs is partially perturbed after large-strain oscillations which causes the Payne effect.

One of the suggested models assumed the presence of bridging chains between NPs and/or clusters with highly retarded conformations (i.e. extremely stretched chains). However, no direct evidence of such stretched chains was found in a SANS study<sup>189,190</sup>. On the other hand, a theory that considers the nano-reinforcement effect as a consequence of the altered chain dynamics and segmental packing near the particle surface is supported by vast number of experiments. The following example was chosen for illustration. The average interparticle separation of randomly packed monodisperse rigid spheres equals to their diameter at the particle content  $\approx 2.6$  vol. %<sup>30</sup>, i.e., randomly distributed 1  $\mu\text{m}$  spheres lie in average 1  $\mu\text{m}$  apart while 10 nm spheres are separated only by 10 nm at this loading (Fig. 10B). In the former case, the separation distance is three orders of magnitude larger than the average radius of gyration, which allows only a small part of the matrix chains to interact with the NP surface while the majority remains unaffected in the bulk. Small enough particles ( $\lesssim 10$  nm), on the other hand, are separated by narrow distances, which means that all the chains are located in the proximity of at least one particle, effectively erasing the bulk matrix properties. If the interaction between the NPs and the polymer is highly repulsive, the chain dynamics accelerates and, in contrary, decelerates in the case of attractive particles<sup>32</sup>, which form an immobilized layer of adsorbed chain segments around their surface. Hence, the segmental immobilization originates from these interactions as an additional mechanical reinforcement largely responsible for the observed non-classical stiffening. The immobilization is only relevant to mobile chains; therefore, the large reinforcing effect is typically observed above the glass transition temperature as will be discussed in detail further in the text. The reinforcing effect is particularly strong when a continuous NP network is created at higher particle volume fractions<sup>188</sup>. It has been suggested by various authors<sup>47-49,191</sup> that the formation of percolated NP network improves stiffness by deforming this percolated structure responding with the particle-particle interactions under the loading. Hence, nanoparticle percolation expectedly stands for a second nano-reinforcing mechanism within the polymer nanocomposites.

A “*modified matrix*” concept was developed based on experimental results<sup>55,185,187,192-195</sup> to address the altered chain dynamics and chain packing in the vicinity of NPs. The model assumes that the modified matrix consisting of immobilized “*glassy*” chains coexists in the nanocomposite with the bulk unmodified matrix as schematically illustrated in Fig. 12. When the chain immobilization is taken into account, the modulus recovery times of hydroxyapatite filled poly(vinyl acetate) could be explained by the reptation dynamics, as was demonstrated

by Kalfus and Jancar<sup>193</sup>. In principle, the modulus recovery times are constrained by two limiting cases, the lower one represented by the reptation of neat matrix and the upper one by the fully immobilized matrix, which is reached when the nanofiller specific surface area rises to approximately 42 m<sup>2</sup>/g. At the percolation threshold, the recovery time dependence on NP volume fraction exhibits an abrupt increase towards the upper theoretical limit, which correspond with the expected stiffening effect of the percolated structures.

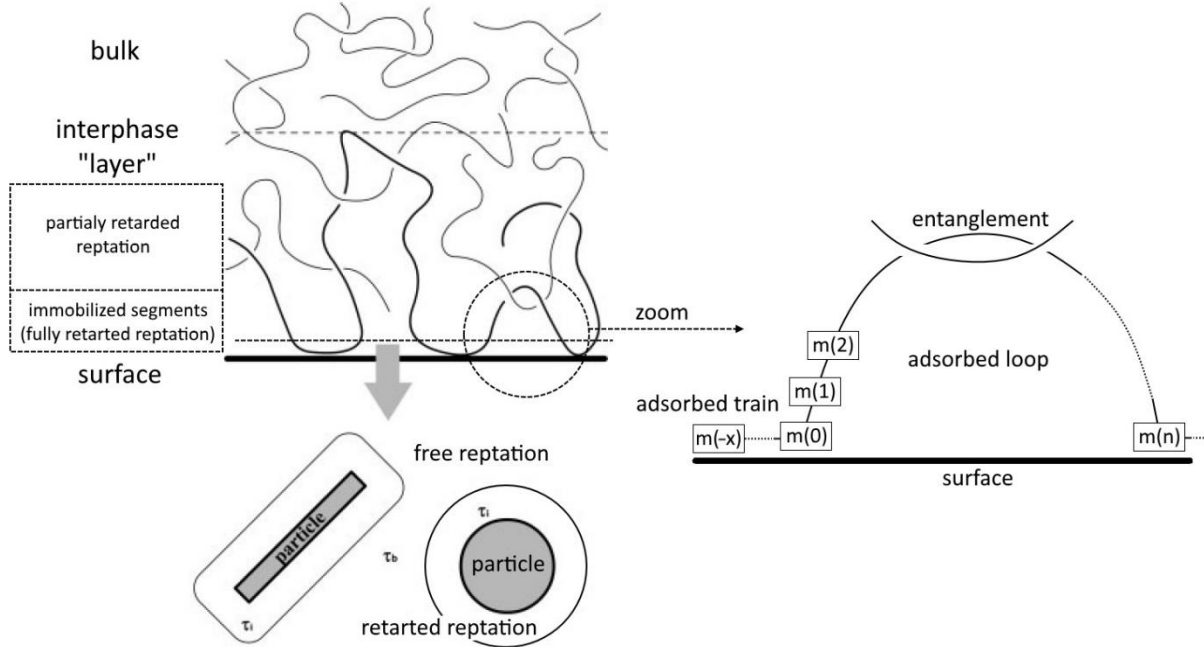


**Fig. 12:** Simplified scheme of a single nanoparticle surrounded by immobilized segmental layer and frustrated-packing interphase "layer" with thickness of approximately  $R_G$  embedded in a glassy matrix. Reprinted with a permission from the ref. 193. Copyright 2007 John Wiley and Sons.

Akcora, et al.<sup>196</sup> derived equations for the bulk ( $K$ ) and the shear ( $G$ ) moduli of PNCs based on their model system represented by nanosilica filled polyethylene. In order to obtain a good fit of the experimental results, they introduced a new parameter  $\alpha$ , which represents the modified matrix ratio:

$$\alpha = \frac{m_2}{\varphi} \quad (1)$$

where  $\varphi$  stands for the filler volume fraction and  $m_2$  represents the relative amount of the modified matrix out of the total matrix amount  $m$  given by the equation  $m = m_1 + m_2$  where  $m_1$  is the relative amount of the unmodified bulk matrix. The combined volume of nanoparticles and modified matrix forms up the nanocomposite inclusions which volume content is  $\varphi' = \varphi + m_2 = \varphi(1 + \alpha)$ . The effective nanocomposite moduli are then given by the following equations:

$$K = K_m + \frac{\varphi'(K_f - K_m)}{1 + (1 - \varphi')R_m(K_f - K_m) + R} \quad (2)$$

and

$$G = G_m + \frac{\varphi^{(G_f - G_m)}}{1 + (1 - \varphi')Q_m(G_f - G_m) + Q} \quad (3)$$

where

$$R = \frac{\alpha}{1 + R_f(K_m - K_f)} \quad (4)$$

$$Q = \frac{\alpha}{1 + Q_f(G_m - G_f)} \quad (5)$$

The subscripts 'm' and 'f' mark the values related to the matrix and the filler, respectively. Finally, the parameters  $Q_m$ ,  $Q_f$ ,  $R_m$ ,  $R_f$  are calculated from the equations:

$$R_i = \frac{3}{3K_i + 4G_i} \quad (6)$$

$$Q_i = \frac{6(K_i + 2G_i)}{5G_i(3K_i + 4G_i)} \quad (7)$$

where the subscript  $i$  is to be replaced either by 'm' or 'f' to refer to the matrix or the filler, respectively. The main drawback of their model is its inability to predict the modified matrix ratio  $\alpha$  which has to be fitted from experimental values. However, the reference to their work is included since the attempts to a quantitative description of nanocomposite mechanical properties with regard to their internal structural organization remain scarce.

A segmental immobilization is usually coupled with an increase of the glass transition temperature  $T_g$  while the opposite applies for repulsive interactions. The immobilization mechanism also explains why the tremendous reinforcing effect of NPs is typically found above  $T_g$  as manifested by a strong increase of plateau modulus, reptation time and stiffness<sup>47-49</sup>, while the impact of NPs on mechanical properties at a low filler content below the glass transition temperature is generally modest (examples shown in Fig. 13) and any significant increase of the mechanical strength is usually attributed to the stress transfer<sup>197</sup> or a physicochemical cross-linking<sup>33</sup>. However, Jancar, et al.<sup>188,198</sup> observed an improvement of mechanical properties (elastic modulus, yield, strain softening and strain hardening response) of nanosilica filled PMMA at  $T_g - 80$  K, far below the glass transition temperature, which was relatively low compared to the increase above  $T_g$  but unexpectedly high regarding the continuum mechanics models<sup>188</sup>. A kinetic analysis of yield, strain softening, and strain hardening showed that the activation energies of these processes increase with the specific interface area. The authors suggested that an elevated amount of energy is required to activate the adequate segmental rearrangements related with the plastic flow and the strain hardening in the presence of NPs. In agreement with the immobilization theory, the  $\alpha$ -process related to the entire backbone of the PMMA chain was more influenced by the presence of the rigid particles than the  $\beta$ -process, which presumably concerns only several segments.

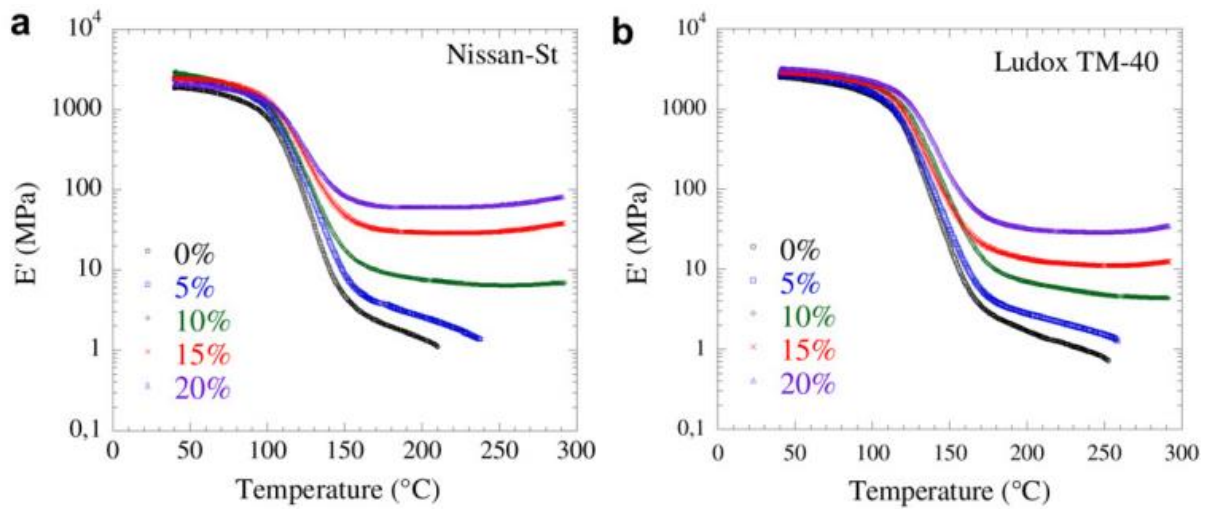


**Fig. 13:** Storage modulus as a function of temperature for PMMA based nanocomposites filled with commercially available silica **(A)** Nissan-St and **(B)** Ludox TM-40. Reprinted with a permission from the ref. 48. Copyright 2012 Elsevier.

However, some experimental data disturbs the simplicity of the segmental immobilization theory. For instance, it is not trivially obvious why PS should show a stronger reinforcing effect by nanosilica than PMMA<sup>47–49</sup>, since silica interacts strongly with PMMA through the hydrogen bonding while only weak dipole-dipole interactions occur in PS. A possible explanation might be found in the suggestion by Tannenbaum, et al.<sup>199,200</sup> who proposed that there are two possible options of the chain adsorption onto rigid attractive particles. Weakly binding polymers prefer the formation of loops with a longer effective range, in which most of the segments reside out of the NP surface. On the other hand, strongly binding polymers form “trains” with a short spatial reach in which segments are preferentially located on the NP surface. Both cases are incorporated in the schematic illustration in the Fig. 12. Hence, strongly interacting chains show a shorter spatial impact on the surrounding chains despite being strongly adsorbed on the NP surface. According to this concept, an adsorption mode should be considered as an additional parameter regarding the PNCs macroscopic properties.

The mechanical strength of PNCs compared to the neat polymer could only be retained or enhanced in the absence of supercritical flaws while the presence of another component may reduce the flaw-sensitivity<sup>201</sup>. It could be also boosted indirectly by a crystalline-phase transition of semi-crystalline polymers if the crystalline modification with a higher elongation to break is promoted by the presence of nanoparticles<sup>1</sup>. A strong adhesion of polymer onto a particle on the other hand restricts the matrix debonding and causes a brittle fracture coupled with a declined elongation to break<sup>201</sup>. Nanoparticles cause up to a several-fold increase of fracture toughness through microcracking, pinning, deflection and branching of the crack, rupture and pull-out of the NPs and it is further improved by a particle alignment for cracks growing transverse to the alignment direction<sup>14</sup>. The role of geometry extends to the particle shape-dependency since 1D nanofibers promote intrinsic toughness attributed to the void growth mechanism while 2D nanoplatelets are more effective in increasing the extrinsic toughness due to the pull-out and crack bridging<sup>74</sup>.

## 3.2.2. Rheological properties

### 3.2.2.1. Steady-flow rheology

Nanocomposite melts and solutions are viewed as colloidal-size particles immersed in a liquid continuum. This concept is especially durable in the case of low molecular weight chains exhibiting Newtonian flow behavior and containing well-dispersed nanoparticles. Strongly interacting chains form an adsorbed layer around NPs while weakly interacting ones tend to slip from the NP surface and can cause a depletion attraction. As a result, the effective hydrodynamic volume of NPs is altered from that expected for bare hard spheres of the same size. Kim and Zukoski<sup>53</sup> addressed these changes by introducing an additional scaling factor  $k$  into the well-established Einstein-Stokes equation:

$$\eta_r = 1 + 2.5 k\varphi + H\varphi^2 + \dots, \quad (8)$$

where  $\eta_r$  and  $\varphi$  stands for relative viscosity and particle volume fraction respectively. The value of 2.5 is the so-called Einstein's coefficient derived from the analytic solution of a flow around an isolated hard sphere.  $H$ , also sometimes marked as  $B_1$ , is the second virial coefficient, also known as the Huggins coefficient, which reflects the interparticle interactions<sup>104</sup>. The value of  $2.5k$  equals intrinsic viscosity  $[\eta]$  and could be readily assessed experimentally. Kim and Zukoski<sup>53</sup> reported values of  $k$  ranging from large positive for NPs encapsulated in strongly adsorbed polymer layers to large negative for NPs smaller than polymer radius of gyration  $R_G$  in entangled polymers<sup>53</sup>. Negative intrinsic viscosity contradicts the continuum rheological models since particles distort the flow of the surrounding liquid and increase the amount of the energy distorted upon flow which is reflected in the increased viscosity<sup>202</sup>. However, molecular dynamics simulations revealed that the NP diffusion coefficient reaches a steady value upon increasing the molecular weight of polymer medium despite it should be gradually slowed down due to the raising bulk viscosity<sup>203</sup>. It should be noted that the equation (8) was based on experiments with fairly oligomeric chains (about 8 segments long) and does not consider other factors such as the rotation of particles which also impacts the value of the intrinsic viscosity<sup>202</sup>. Small NPs of the size equal or smaller than the polymer tube diameter or the entanglement mesh-length were indeed reported to diffuse through the entangled polymer faster than predicted by the continuum Stokes-Einstein equation<sup>204,205</sup>.

Zukoski, et al.<sup>71</sup> compared experimental structure factors of a strongly interacting system (silica/polyethylene oxide) obtained from scattering measurements to the PRISM model and concluded that low molecular weight PEO keeps the silica NPs dispersed while high molecular weight PEO flocculates the NPs into a bridged state. Rheological measurements revealed a hard-sphere-like behavior ( $H \cong 5.9$ )<sup>71</sup> of spheres enlarged by  $(2.82 \pm 0.08) \cdot R_G$ <sup>66,70</sup>. The linear dependence of the NP effective hydrodynamic diameter on the polymer radius of gyration  $R_G$  is preserved even when the molecular weight exceeds the critical entanglement value  $M_c$ . Altogether, the experimental evidence suggests a presence of a polymer layer adsorbed on the NP surface in a thickness proportional to the random coil radius of gyration ( $\sim 1.4 R_G$ ). However, the scattering experiments did not correlate with the hard-sphere like behavior detected by rheology and, instead, yielded a constant effective size  $D_{NP} + 20 \text{ nm}$ <sup>70</sup>

which suggests that polymer segments were affected further beyond the reach of the adsorbed layer up to  $\sim 10$  nm from the particle's surface. Interestingly, this value is identical to the expected range of the hydrophobic interaction<sup>29</sup>. Wang, et al.<sup>65</sup> also studied the silica-PEO system and they observed that in a dilute aqueous solution at  $\text{pH} \cong 9.6$ , the thickness of the adsorbed PEO layer measured by dynamic light scattering was nearly equal to the size of sole PEO coils in the same medium, i.e., more extended than in a PEO melt. Despite the silica NPs were only 12 nm in diameter, about three times smaller than that used by Zukoski, et al., the results were comparable for  $20\,000\text{ g}\cdot\text{mol}^{-1}$  and  $200\,000\text{ g}\cdot\text{mol}^{-1}$  PEO suggesting that the NP-chain relative size plays a minor role in this case.

Four critical NP volume fractions were recognized in the silica/PEO system<sup>66</sup>. The first corresponds to the situation when NP separation drops below  $\text{ca } 6 R_G$  and bulk chains get constrained between two layers adsorbed on two neighboring particles. The layers eventually start to interact with each other at  $\text{ca } 3.6 R_G$  and cause a rapid increase of the low-frequency modulus. It will be discussed below that low frequencies are related to the reptation motion and presumably, the entanglement dynamics of the adsorbed polymers is altered. However, this effect was observed even for chains below the critical entanglement molecular weight. Further on, a colloidal glass transition takes over when the interparticle separation drops below approximately  $2.9 R_G$  – coinciding with the volume fraction of the colloidal hard-spheres glass transition ( $\varphi = 0.58$ ). Finally, sufficiently high molecular weight matrix ( $M_w > 2000$ ) leads to a fluid-to-brittle transition at the constant molecular-weight-independent volume fraction of 0.317.

In a weakly interacting system (silica/polytetrahydrofuran) with NPs in the near mutual contact, fluid-like properties are preserved up to high particle volume fractions until a gel is eventually formed<sup>71</sup>. A weak adsorption accelerates the segment mobility near the NPs<sup>69</sup> and causes segments to slip off the surface while the intrinsic viscosity falls below the Einstein's value of  $[\eta] = 2.5^{71}$ . A medium interaction strength (silica/polyethylene oxide dimethyl ether) gives birth to a complicated attraction-repulsion balance of the enthalpic and the entropic forces. Gelation, i.e., percolation of the inner 3D network accompanied by transition from liquid-like to solid-like behavior, occurs above 20 % of NPs and hints at the long-range repulsive behavior accompanied with an enhanced structuring at low particle loadings. The elevated intrinsic viscosity suggests presence of an adsorbed polymer layer but, unlike in PEO, this increase as well as the nanocomposite structure factor is independent of the polymer molecular weight. The theoretical explanation of this behavior still remains a scientific challenge<sup>71</sup>.

#### 3.2.2.2. Rheology under Oscillation

Viscoelastic properties of complex fluids are also investigated with rheological oscillatory measurements. When carried out at relatively small-amplitude oscillatory deformations, the elastic storage ( $G'$ ) and the viscous loss ( $G''$ ) moduli are independent of the strain amplitude and fall within the linear-viscoelasticity regime. Such experiments are referred to as the small-amplitude oscillatory shear (SAOS) tests. The non-linear viscoelasticity regime is entered when

the diffusion is no longer capable to recover the disrupted structures under the large-amplitude oscillatory shear (LAOS).

It has been long established that the zero-shear elastic modulus  $G_0$  of particle gels scales with the volume fraction  $\varphi$  according to the power law<sup>206</sup>

$$G_0 \propto \varphi^m, \quad (9)$$

where the exponent  $m$  is believed to depend on the interparticle interactions<sup>207</sup> and its experimental value was reported to vary between 3.2–7.2<sup>88,207–210</sup>. Furthermore, it is expected that the exponent can also incorporate the influence of the filler structure. Piau, et al.<sup>211</sup> investigated silica fractal aggregates and proposed that the power law exponent  $m$  is equal to  $\frac{5}{(3-D)}$  where  $D$  is the fractal dimension of the structures. According to this equation, the datasets for the different types of silica collapse into a single master-curve. However, the situation becomes more complex when extended to the time (frequency) related behavior. During oscillatory tests, neat polymer melt response is governed by the reptation dynamics at low frequencies and shifts towards the Rouse dynamics at higher frequencies. The former is characterized by a quadratic dependence of the storage modulus and a linear dependence of the loss modulus on the frequency, while both moduli scale with the square root of the frequency in the latter case<sup>179</sup>. Robertson, et al. reported that there is yet another process with even longer relaxation times than the reorientation of an entangled chain – approximately 1.5times longer relaxation time which was attributed to the re-entanglement kinetics of chain molecules disentangled upon shearing<sup>212</sup>. Data by multiple authors<sup>179,181,207,213–215</sup> suggests that the reptation dynamics is, unlike the Rouse dynamics, affected by nanoparticles and retarded (Fig. 14A). High loadings of nanoparticles may cause a nonterminal behavior and introduce a low-frequency plateau in the frequency dependence of the storage modulus<sup>181</sup>. In addition, layered silicate nanocomposites were reported to violate the empirical Cox-Merz equation<sup>54</sup> established for polymer melts and solutions<sup>216</sup>:

$$\eta(\dot{\gamma}) = \eta^*(\omega), \quad (10)$$

for the value of the shear rate  $\dot{\gamma}$  equal to the angular frequency  $\omega$ . The symbol  $\eta$  stands for the steady shear viscosity and  $\eta^*$  denotes the complex viscosity which relates the oscillatory shear rate  $\dot{\gamma}$  to the shear stress  $\tau$ .

Kabanemi, et al.<sup>217</sup> proposed a reptation-based model to address the dynamics and the rheology of linear entangled polymers constrained by rigid nanoparticles according to which the effective reptation time is controlled by the polymer molecular weight, nanoparticle size, interaction-site density on the nanoparticle surface, monomer-nanoparticle energetic interaction and nanoparticle volume fraction. It predicts that the effective reptation time  $\tau_{d,eff}$  of a chain in the presence of a nanoparticle scales as:

$$\tau_{d,eff} \propto \tau_d(\varphi_{ad}N + 1)^2, \quad (11)$$

where  $\tau_d$  stands for the effective reptation time of a polymer chain in the bulk,  $\varphi_{ad}$  is the fraction of attached monomers per chain and  $N$  is the number of monomers per chain. As

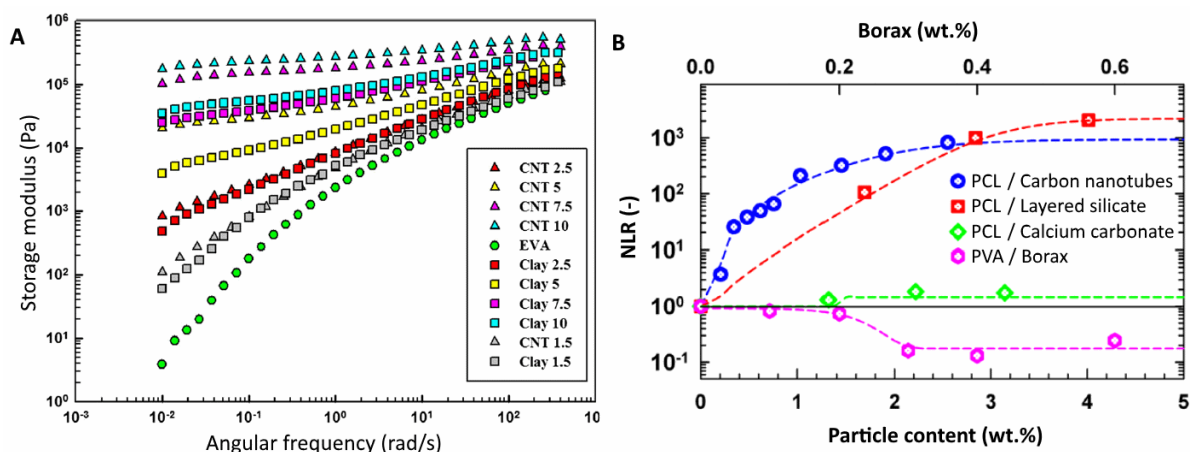


**Fig. 14: (A)** Influence of carbon nanotube (CNT) and clay NPs on low-frequency storage modulus of polyethylene vinyl acetate (EVA). Reprinted with a permission from the ref. 179. Copyright 2014 Springer. **(B)** Systems with various dependence of nonlinear-linear viscoelastic ratio (NLR) on particle content – multiwall carbon nanotubes, layered silicate and precipitated calcium carbonate in polycaprolactone (PCL), borax in polyvinyl acetate (PVA). Reprinted with a permission from the ref. 181. Copyright 2013 AIP Publishing.

discussed above, the nanoparticle spatial organization is closely tied with the polymer adsorption onto nanoparticles and it is therefore reasonable to expect that different dispersion states would feature a different fraction of attached monomers per chain and, consequently, different effective reptation times.

It is assumed that LAOS experiments provide more reliable information relevant to the inner structure than SAOS, since some differently structured materials show the same extent of deformation under small strain while varying in their non-linear response<sup>218</sup>. Several methods have been developed to reduce the LAOS experimental data, among them a shape analysis of the stress-strain (Lissajous) curves and the Fourier-transform analysis. It has been found that only the odd harmonics form the response and presence of the even harmonics is caused by measurement artefacts, such as a secondary flow or a wall-slip of the sample from the geometry<sup>181</sup>. The storage and loss moduli lose their physical meaning in the Fourier-transform rheology, instead, these terms are commonly used to refer to the first harmonics. The next strongest signal is related to the third harmonic which is often presented as the intensity ratio normalized by the first harmonic  $I_{3/1}$ <sup>101</sup>.

At large amplitudes, the shearing cycle represents rather a set of successive processes than a single mechanism governing the viscoelasticity. A sample is strained first and eventually yields at high strain. A flow follows and the structure is then rejuvenated at the end of the cycle<sup>219</sup>. The rheological response averaged over the whole cycle could be approximated as interplay between creation and destruction of structural domains which are both exponential functions of the shear stress. There are four basic classes of the viscoelastic behavior under LAOS<sup>100,101</sup>. The type I (*shear thinning*) is the most common one in polymer melts and solutions. It originates from the flow orientation similarly to shear thinning under the steady flow. Contrary, samples with strong interaction between some structural elements exhibit the type

II (*shear hardening*) response which is believed to be associated with a shear-induced formation of complex microstructures. When formation and destruction rates are balanced, the increasing strain amplitude results into a local maximum either of the loss modulus (type III, *weak strain overshoot*) or both the loss and the storage moduli (type IV, *strong strain overshoot*). The former is typically exhibited by soft glasses while the latter was observed for instance in associative polymer solutions. The type IV behavior is presumably driven by the interaction strength weaker than in the type II but superior to the type III.

Hyun, et al. combined both the LAOS and the SAOS measurements and introduced a nonlinear-linear viscoelastic ratio (NLR) as a relative comparison of contributions from the nonlinear and the linear changes induced by particles (or another component) to the viscoelasticity of the matrix<sup>181</sup>. NLR takes value of 1 if the linear and the nonlinear properties scale in the same manner with the increasing particle loading. When the influence on the nonlinear response exceeds that on the linear one, NLR takes value greater than 1, and, in the contrary situation, NLR is less than unity. Examples of real systems are shown in Fig. 14B for all three cases. The main drawback of the NLR parameter is that, despite its capability to qualitatively distinguish between different microstructures, it misses a clear link to the inner structure of the material and has to be correlated with additional information and measurements. Dramatic changes in the viscoelastic properties of PNC occurs near the percolation threshold<sup>180</sup> which represents an alternative to the polymer gelation<sup>179</sup>. Strong NP networks contribute less to the non-linearity than to the linearity ( $NLR < 1$ ) while opposite applies to dispersed particles ( $NLR > 1$ )<sup>181</sup>. The critical strain which disrupts percolated carbon nanotubes in polycaprolactone melt also caused the saturation of the third harmonics  $I_{3/1}$ , a behavior qualitatively different for both the pure melt and the low-strain response<sup>181</sup>.

### 3.2.3. Electrical properties

A range of electromagnetic properties was successfully tuned by the addition of nanoparticles, e.g. electric conductivity/resistivity<sup>1,13,172,174</sup>, dielectric constant and permittivity<sup>1,12</sup>, DC electric breakdown strength<sup>1</sup> or piezoresistive sensing<sup>172</sup>. Examples of some interesting features which spring from the structural organization follow.

The electrical conductivity of a polymer nanocomposite greatly improves upon the percolation of electrically conductive nanoparticles forming conductive channels across the whole sample. In the case of anisotropic NPs, the percolation threshold decreases with the particle alignment<sup>13</sup>. Hence, the conductivity could be boosted by the particle orientation at a low filler content while only a minor improvement was achieved at a concentration where randomly distributed NPs are already percolated<sup>172</sup>. This way, the electric conductivity in the alignment direction was successfully tuned across 6 orders of magnitude and the material was transformed from insulator to a metallic conductor by the electric field induced alignment<sup>13,174</sup>. Remarkably, the electrical conductivity in the lateral direction increased by two orders of magnitude due to the dielectrophoretic migration and lateral crosslinks and coarsening<sup>13</sup>.

In contrary, the resistivity of a polymer nanocomposite could be enhanced by addition of insulating NPs (e.g. surface modified magnesium oxide)<sup>1</sup>. If well dispersed, these particles can polarize and create potential wells which trap charge carriers and reduce the overall conductivity and, at the same time, they improve the DC electric breakdown strength (by 15 % in ref. 1) by suppressing the space-charge accumulation. When aggregated though, they act as defects and weak points in the bulk of the material which entrap the charge carriers, accumulate charge and reduce both the electric resistivity and the DC electric breakdown strength<sup>1</sup>. The dielectric permittivity increased slightly regardless the structure, depending on the NP concentration. However, all these changes are far less dramatic than the above-mentioned conductivity enhancement, taking place in the range of only several tens of percent.

Li, et al.<sup>12</sup> developed silica coated nanosilver core-shell particles to fabricate a high dielectric constant and low dielectric loss nanocomposite capacitor material. The structure is clearly beneficial to the application since the silica coating effectively prevents the contact between the silver cores and restricts the tunneling currents while allowing for a high NP packing and maximizing the charge accumulation. Overall performance is controlled by the silica layer thickness, but a similar effect is achieved by small ceramic NPs, which fill in the voids between the core-shell NPs and keep them at distance.

### 3.2.4. Magnetic properties

The magnetic behavior of a polymer nanocomposite is largely inherited from the magnetic character and the volume content of the particles with distinct magnetic properties and controlled by the particle orientation and spatial arrangement<sup>115,117,127,162,220,221</sup>. A homogeneous dispersion of magnetic particles is usually sufficient to enhance the overall magnetic properties and render the whole nanocomposite magnetically responsive though ensembles with anisotropic structure commonly provide stronger magnetic response and yield higher remanent magnetization as well as saturation magnetization in the direction of the particle orientation due to the (partial) alignment of particles' easy magnetization axes<sup>116,117,126,127,222</sup>. Correspondingly, the saturation magnetization was reported to vary in the order 1D chains (in the alignment direction) > disordered NPs > 3D array<sup>115</sup>. Furthermore, nanoparticle arrays aligned in a regular pattern are subjected to the well-known structure-related phenomena of ferromagnetism and antiferromagnetism which affect the magnetic properties analogically to common magnetic materials<sup>115,116,156</sup>.

The introduction of magnetism into a composite directly impacts other macroscopic properties of the material. The interparticle magnetic forces induced by the particle magnetization oppose any external mechanical loading and increase the tensile modulus and strength, viscosity and shear modulus of magneto-responsive solids<sup>223,224</sup>, fluids and soft gels<sup>225,226</sup>, correspondingly. Balance between the elastic and the magnetic forces was successfully turned into a smart design of the so-called magnetic origami<sup>227-229</sup>, where linear or planar precursors with patterned magnetic dipoles spontaneously fold into the predetermined 3D shapes (Fig. 15). Such approach combines the benefit of a relatively simple 2D processing with the advanced properties of 3D structures which would be difficult to

fabricate by conventional means. In principle, the origami technique is not restricted to magnetic materials and other tailorable forces such as capillary force<sup>230</sup> may be utilized but the magnetic origami is easily realized and controlled by the magnetic nanoparticle doping while it yields stable structures thanks to the dipole-dipole interactions.

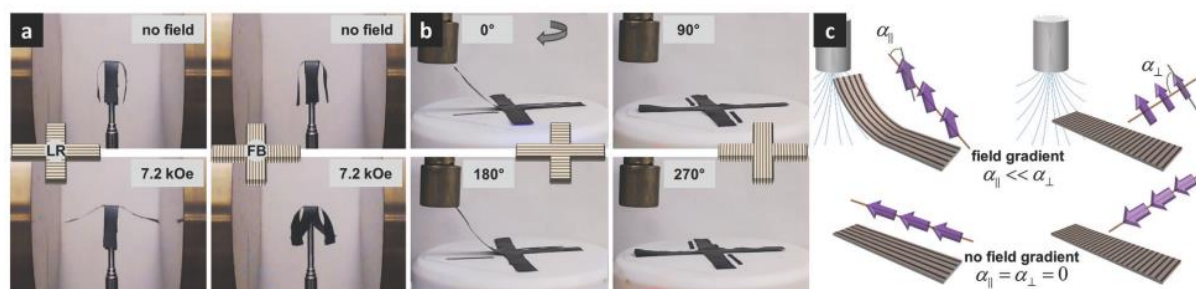


**Fig. 15:** Magnetic origami – anisotropic actuation under (A) uniform horizontal magnetic field for the cross attached by its center with chains of magnetic particles oriented (left) parallel and (right) perpendicular to the field, (B) magnetic field gradient from a permanent magnet that selectively lifts arms with parallel but not perpendicular chains while the cross is being rotated. (C) Schematic view of magnetic NP dipoles orientation relative to chain direction in the presence and absence of a field gradient generated by a permanent magnet. Reprinted with a permission from the ref. 227. Copyright 2015 Royal Society of Chemistry.

### 3.2.5. Optical properties

Most common optical applications (mirrors, lenses, etc.) require transparent materials with low dispersion of light. To suit that need, optical homogeneity is highly desirable. This condition could be met even for a structurally heterogeneous material in the case of matching refractive indices of its components/heterogeneities. At the nanoscale, below the critical scattering size, a precise match of the refractive indices is somewhat less critical as was proven experimentally by preparing exotic transparent materials from crab shell<sup>82</sup> and wood<sup>83</sup> by filling their nano-porous structure with an acrylic polymer. Consequently, an aggregation of NPs is usually unfavorable in optical nanocomposites requiring good optical clarity and minimized scattering. The demand for a good optical performance puts constraints on simultaneous enhancement of the optical and other structure-related properties where clusters and percolated networks would be beneficial but even this limit was successfully overcome by a function specific structural design, for instance a double-percolating network was developed to fabricate an electrically conductive and optically transparent nanocomposite<sup>108</sup>.

The refractive index (RI), a basic optical parameter of functional materials, scales linearly with NP content in simple polymer nanocomposites<sup>231</sup> due to the volume replacement mechanism<sup>232</sup>. High refractive index nanocomposites with RI adjustable by concentration could be fabricated by the introduction of high-RI NPs such as titanium oxide<sup>231</sup>. In a general case, however, the linearity of the refractive index dependence on the concentration could be distorted by various effects such as the plasmon resonance<sup>233</sup>. In a more complex design, a

nanocomposite was fabricated to exhibit negative refractive index value in the MIR spectrum<sup>6</sup>. This extraordinary feature originates from metal nanoparticles coated with a high-RI dielectric layer, which are immersed in a low-RI polymer matrix due to the size governed overlap between the electric and the magnetic dipoles resonance.

Photonics is another field, which can benefit from the remarkable properties of polymer nanocomposites<sup>109–111,151,154</sup>. The diffraction wavelength of a single spherical particle with a magnetic moment depends on the magnetic field tilting angle<sup>125</sup>; moreover, the diffraction wavelength is tuned by the periodicity of the photonic structure<sup>151</sup>. A single-ink printing technique with a high color depth is being developed based on the structural control over the orientation and/or periodicity of nanoparticles fixed in a polymer matrix<sup>109,110</sup> (Fig. 16).

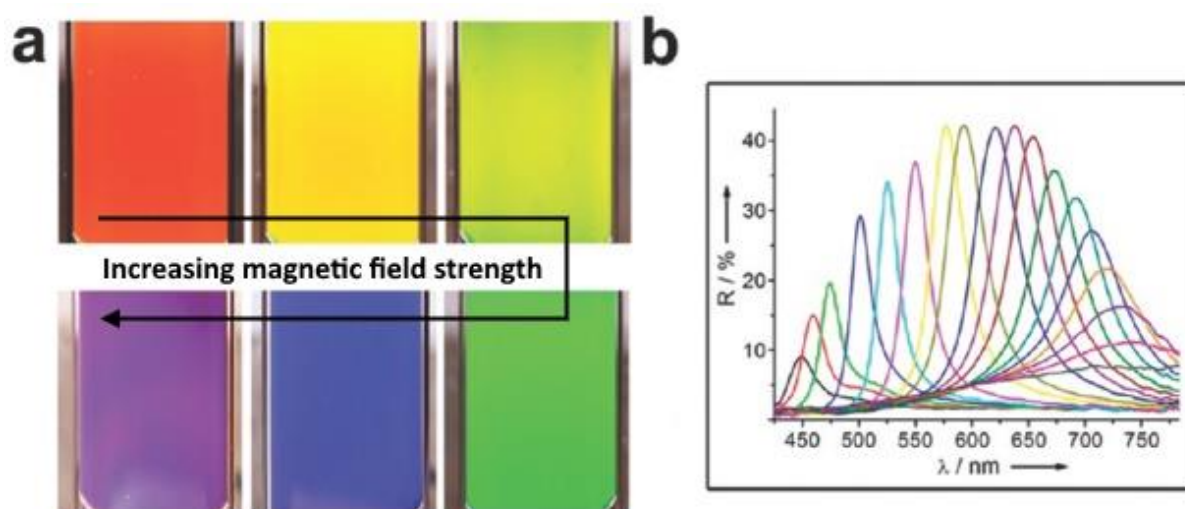


**Fig. 16:** Colloidal nanocrystal clusters dispersion as a material for single-ink structural high color-depth printing **(A)** Digital photos evidencing diffraction color change in response to a varying magnetic field strength. **(B)** Reflectance spectra of the same sample in varying magnetic field strength. Reprinted with a permission from the ref. 109. Copyright 2012 American Chemical Society.

### 3.2.6. Barrier properties

A barrier property represents a general term for a performance related with transport processes through the material. For instance, some inorganic nanoparticles enhance the thermal stability of PNCs by forming a protective ceramic layer upon heating after the initial ablation of surrounding polymer matrix, which reduces the heat flux and slows down the thermal degradation of the material<sup>79,84,85,234,235</sup>. This additional stability is evidenced as a shift of the main degradation step on TGA curves towards higher temperatures. However, it shall be noted that the protective mechanism is kinetic, and the performance depends on parameters such as mechanical stability of the protective layer. The formation could also vary a lot between an oxidative and a non-oxidative atmosphere. Hence, reports on an increased degradation temperature of PNCs has to be proceeded with care.

The probably most intensively researched applications based on barrier properties are probably separation membranes for various gases and liquids<sup>15–17,236–239</sup>. The conventional size-controlled polymer membranes are not able to couple a high permeability with a high selectivity and the improvement of one parameter is tied with the decrease of the other. NPs can either enhance<sup>3,17,236,239,240</sup> or suppress<sup>3,15,238</sup> the membrane permeability regarding the filler type and its specific interaction with the matrix and permeating molecules. The specific performance can be readily tuned by a NP surface treatment<sup>3</sup>. Decreased permeability results from presence of impermeable phase<sup>15</sup> while unselective enhancement of permeation originates from particle porosity<sup>17</sup> and/or relaxation of the polymer and altered chain packing near the nanoparticle surface<sup>3,15</sup>. A good selectivity is achieved by a strong adhesion of NPs to the matrix since a poor adhesion facilitates the formation of unselective voids at the interface and promotes a diffusion of a wide range of species<sup>241</sup>.

An example of a structurally driven property control was reported by Gupta, et al.<sup>16</sup> who adjusted the water uptake and, consequently, the proton conductivity by an addition of hydrophilic NPs of various functionality into sulfonated poly(ether ether ketone) membranes for a fuel cell application. The highest conductivity was achieved in samples with well-dispersed NPs while more hydrophilic particles yielded a lesser enhancement of the water uptake, contrary to the expectation, because their hydrophilicity caused them to collapse into aggregates and expose a lower portion of their surface to water (Fig. 17). A good dispersion is seemingly preferential for the enhanced permeation in order to maximize the surface area. Clusters, on the other hand, may create long diffusive pathways for small molecules such as permanent gases (hydrogen, nitrogen, etc.) while permeation of larger species is far less affected due to the size exclusion effect; hence, the selectivity to large molecules is promoted<sup>240</sup>. This so-called reverse selectivity is well known from the application in reverse membranes.

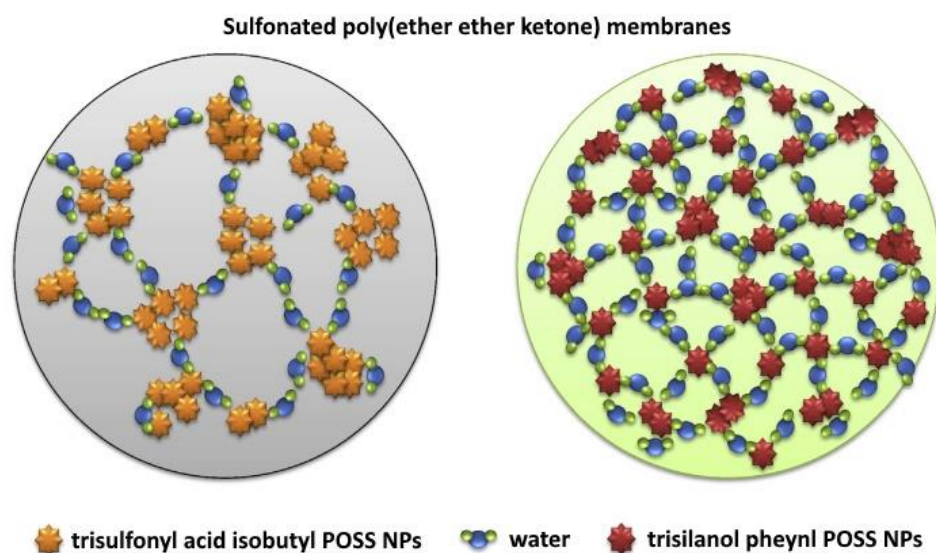


**Fig. 17:** Schematic view of fuel cell membrane microstructure with amount of water uptake and, consequently, proton conductivity controlled by structure. Reprinted with a permission from the ref.

16. Copyright 2013 Elsevier.

## 4. Aims of thesis

This Thesis aims at advancing fundamental understanding of the role of preparation protocol on the structure and properties of polymer nanocomposites. In particular, it focuses on investigation of the principle variables governing nanoparticle spatial organization in model PNCs prepared by solution blending. Effects of both kinetic and thermodynamic variables, e.g., particle size and shape, polymer molecular weight, particle-polymer interaction strength, temperature, shear stress and strain are investigated over a range of NP and polymer concentrations. Attempt is made to analyze the experimental rheological and thermomechanical data using structural information and existing microscopic models.

## 5. Methods

A general-purpose polystyrene Krasten 154 (PS, Synthos Kralupy, Czechia,  $M_w = 280\,000$ ) was utilized as a matrix for initial tests along with octaphenyl-polyhedral oligomeric silsesquioxane (OP-POSS, Hybrid Plastics, Inc., USA) and octamethyl-polyhedral oligomeric silsesquioxane (OM-POSS, Hybrid Plastics, Inc., USA) nanoparticles. Commercial grade polymethylmethacrylate (PMMA) Plexiglas 8N (Evonik Industries AG, Germany) with  $M_n = 50\text{ kg}\cdot\text{mol}^{-1}$ ,  $M_w/M_n = 1.9$ , and  $T_g = 113\text{ }^\circ\text{C}$  (DSC,  $10\text{ K}\cdot\text{min}^{-1}$ ) was used as a matrix. According to NMR analysis provided by the supplier (Evonik, Germany), the PMMA contains 5–7 % of isotactic, 50–52 % of syndiotactic, and 41–52 % of atactic phase, all apparently randomly distributed along each chain. Colloidal bare silica nanoparticles dispersed in isopropanol with the diameter of  $20\pm 4\text{ nm}$  IPA-ST (Nissan Chemicals, Japan) were used as the nanofiller. Toluene in p.a. purity grade was supplied by Lach-ner (Lach-Ner, s.r.o., Czechia). All chemicals were used as obtained with no further purification. OP-POSS/PS composite with POSS concentrations 0.1, 1.0 and 10 wt.% were prepared from the OP-POSS/PS master-batch by solution blending in toluene. The nanocomposite solutions were dispersed with ultrasonic probe Bandelin Sonopuls (Bandelin electronic GmbH & Co KG, Germany) while stirred with a magnetic stirrer followed by vacuum drying at  $140\text{ }^\circ\text{C}$ , at ca  $10\text{--}20\text{ kPa}$ . The NP concentrations were controlled gravimetrically during the preparation and verified employing TGA Q500 thermogravimetric instrument (TA Instruments, Inc., USA) on solid state samples. Rheological behavior was investigated employing AR G2 rheometer (TA Instruments, Inc., USA) with the cone-plate geometry (40 mm diameter,  $2^\circ$  cone) using samples prepared by dissolution of previously obtained nanocomposites in toluene. A PNC-solvent ratio 1:2.5 g/ml (approx. 30 vol. %) was used. Each sample was dispersed for 5 minutes in ultrasonic bath Kraintek K5 (Kraintek Czech, s.r.o., Czechia) one hour prior to the measurement. The tests were performed in the oscillatory regime by varying the applied strain from 0.01 to 5 000 % at frequency 1 Hz and temperature  $25.0\text{ }^\circ\text{C}$ . The results were averaged from two measurements where each data point was obtained as an average of five shearing cycles. A solvent trap was placed around the geometry to prevent solvent evaporation during the measurement.

Colloidal bare silica nanoparticles dispersed in isopropanol with diameter of  $20\pm 4\text{ nm}$  were supplied by Nissan Chemicals (Japan) under the commercial names IPA-ST. Colloidal nanosilica was ultrasonicated by an ultrasonic tip (Bandelin Sonopuls, Germany). Firstly, resonance frequency was found and then, ultrasonication was performed ( $t_{\text{on}} = 0.1\text{ s}$ ). Notably, the starting point for the PNC samples in PMMA was well-dispersed particles in isopropanol. Since isopropanol is weakly acidic ( $\text{p}K_A = 16.5$ ) and miscible with all the solvents used in this research and its concentration in the samples was small, its role in the resulting NP spatial organization was neglected. Then, the desired amount of dispersed nanoparticles was added to polymer solution with the concentration of 66.7 mg of polymer per one milliliter of solvent (about 5.3 vol. %) corresponding to the semi-dilute solution regime. Nanoparticle loading ranged from 0.5 to 10 vol.%. Various solvents were used as the preparation protocol variable: THF, acetone, ethyl acetate, acetone-toluene 1:1 mixture (volumetric ratio), and toluene. All solvents were acquired from Lach-ner (Lach-Ner, s.r.o., Czechia) in p.a. purity grade. Polymer nanocomposite solutions were rigorously mixed at 1200 RPM by a magnetic stirrer for 1 hour. Subsequently, the mixture was rapidly vitrified in a pre-heated chamber at  $140\text{ }^\circ\text{C}$  and kept

there for 24 hours. Grinded samples were further dried for 6 days in a vacuum oven at 140 °C and ca 10–20 kPa to ensure a complete removal of solvent residues. Drying efficiency was checked by thermogravimetric analysis. Dried samples were further grinded and compression molded into 1 mm thick sheets at 190 °C in a hot press (Fontijne Pressess, Netherlands) at closing pressure of 300 kN. The pressure was not relieved until the samples were cooled down to laboratory temperature at a cooling rate of approximately 30 K·min<sup>-1</sup>.

Polymer coil size was determined utilizing DynaPro NanoStar dynamic light scattering device (WYATT, USA) in isopropanol and all the solvents used for sample preparation at various temperatures at concentration of 10 mg·ml<sup>-1</sup> (about 0.84 vol.%) which corresponds to the dilute regime. NP spatial organization and morphology of the PNCs was determined by transmission electron microscopy (TEM, Morgagni 268D 100 kV, FEI, Czech Republic) of ultrathin slides with uniform thickness of approximately 50 nm and by ultra-small-angle X-ray scattering (USAXS, Smartlab diffractometer, Rigaku, Japan) employing the copper rotating anode, 2 × 220 germanium monochromator and 2 × 220 germanium USAXS analyzer. USAXS patterns were analyzed by Guinier and Porod law. USAXS provides an average form and structure information of nanoparticles arrangement in polymer matrix.

TEM provides a direct view of silica nanoparticles arrangement in polymer matrix. The image analysis of TEM micrographs were performed to obtain the distribution function of interparticle separations. Images were chosen to contain minimum of 150 NPs. At first, the NP positions were recorded manually from the TEM images, since the automated particle recognition function failed to recognize single particles within the assemblies due to the insufficient contrast of the neighboring NPs' edges. Due to the approximately 50 nm thickness of the ultramicrotome sections, the electron beam interacts with several NPs on its path through the sample and blurs the particle edges as the 3D structure is being projected into the 2D plane. Particles located above each other will overlap in the TEM snapshot. Therefore, large aggregates are often smeared into objects of an indistinct inner organization. A closer inspection of these objects depends strongly on operator's intuition, which translates into a reduced accuracy of the analysis. In addition, one has to keep in mind that the interparticle separations seen in TEM images are undervalued since they are only 2D projections of the real distances. To extend the statistical population and improve the repeatability, the lengthy operator-dependent manual analysis of the TEM micrographs was replaced by an automated computer-aided image analysis using smaller magnification (44 000×). Since the automated particle recognition function of the ImageJ software failed to recognize single nanoparticles in tight ensembles, the automated TEM image analysis treated clusters and aggregates as the elementary structural units where applicable. The element diameter was calculated by approximating the fitted element area to a circle.

Interparticle separations were computed as Euclidean distances of the centers for each pair of the NPs. It gives rise to  $0.5 \cdot (n - 1)^2$  correlations where  $n$  is the number of NPs. The probability distribution of finding two NPs at a certain interparticle separation was calculated by dividing all the experimentally recorded values into 200 uniformly spaced discrete intervals approximately 4–5 nm wide. The experimentally assessed distribution of interparticle

separation was compared to the probability  $\mathbb{P}$  of finding two randomly selected points in a square in a separation  $D$  equal or less than a threshold value  $d$  given by:

$$\mathbb{P}(D \leq d) = \iint_{\{x^2+y^2 \leq d^2\}} f(x)f(y)dxdy, \quad (12)$$

where  $x$  and  $y$  denotes the absolute value of the difference between the  $x$  and  $y$ -coordinates of the points respectively<sup>242</sup>. For  $x \in (0, a)$ , the function  $f_x$  is given by:

$$f(x) = \frac{2}{a^2}(a - x), \quad 0 < x < a, \quad (13)$$

where  $a$  stands for the length of the square's side. The function  $f_y$  is defined the same way for  $y \in (0, a)$ . After the first integration, the probability function takes the form:

$$\mathbb{P}(D \leq d) = \int_0^d (a - y)\sqrt{d^2 - y^2} (2a - \sqrt{d^2 - y^2}) dy. \quad (14)$$

The outer integration was performed using a numerical method based on the Gaussian quadrature in GNU Octave software<sup>243</sup>. A cut-off value of  $a$ , in the range of 700–800 nm, was selected for each image to provide a reasonable fit to the experimental data. This reflects the fact that the NPs near the image edges were not taken into account if they were part of a structure which larger portion supposedly lying beyond the image's edge. The apparent inter-element distance was determined as the mode, i.e., the most frequently occurring value, which was established from the maximum of the distribution function of the 5 nearest neighbors of each element. The number of neighbors was selected according to the coordination number in a 3D space which is, according to a simple cubic lattice model, equal to 4.68<sup>244</sup>.

Rheological measurements were executed using Ares-G2 rheometer (TA Instruments, Inc., USA) in continuous flow mode with concentric cylinder geometry. The pure polymer solutions exhibited Newtonian behavior at the concentration of interest, which corresponds to the initial mixing step of PNC preparation. Hence, all the presented results were collected at a single strain rate of 20 s<sup>-1</sup> and relativized to viscosities of pure polymer solutions without NPs. The differences in the absolute viscosities of the nanocomposite solutions (1.7–2.9 mPa·s) were marginal compared to the substantial change of viscosity during the solvent evaporation which took place over 10 orders of magnitude (melt viscosity of pure matrix was 4.7·10<sup>7</sup> Pa·s at 140 °C). The diluting effect of isopropanol added with NPs was recognized as insignificant (< 5 % viscosity change for the highest NP concentration) and neglected except the samples in ethyl acetate where the effect was stronger and required a correction for the addition of pure isopropanol without NPs. Samples were stored in sealed glass bottles and measured one day after preparation unless stated otherwise. To minimize solvent evaporation, the procedure time was kept short (< 10 minutes) and the tests were carried out at 25.0 °C. The same instrument was used to record the viscosity of pure polymer solutions at various temperatures, which was required as an input variable for DLS measurements. Glass transition temperature was determined from the maximum of loss modulus from the dynamic mechanical analysis using the RSA-G2 device (TA Instruments, Inc., USA) with a single

cantilever geometry. Rectangular specimens of the typical size  $30 \times 5 \times 1 \text{ mm}^3$  were cut from the molded sheets and their thermo-mechanical history was erased by preheating to  $140 \text{ }^\circ\text{C}$  for 30 minutes. Temperature sweeps were carried out immediately after preheating at deformation amplitude of 0.05 % and frequency of 1 Hz in the range from  $140$  to  $90 \text{ }^\circ\text{C}$  with  $1 \text{ }^\circ\text{C}$  step.

A series of PNCs was prepared from colloidal silica in ethyl methyl ketone (MEK-ST, supplied by Nissan Chemicals, Japan) and polystyrene (Sigma Aldrich, Germany),  $M_w = 192 \text{ kg}\cdot\text{mol}^{-1}$ , in tetrahydrofuran (THF), *N,N*-dimethylacetamide (DMAc), and cyclohexanone (all supplied by Lach-ner, Czechia, in p.a. purity grade) to test the results obtained for the PMMA based PNCs. The NP structural organization was investigated by scanning transmission electron microscopy (STEM) Lyra3 (Tescan, Czechia) and the rheological data was recorded by the same instrument and method as the PMMA samples. Worth noting, the samples in DMAc and cyclohexanone required a correction for the addition of pure ethyl methyl ketone due to their higher absolute viscosities (10.0 and 27.9 mPa·s, respectively).

## 6. Results and discussion

### 6.1. POSS/PS model nanocomposites

The silsesquioxanes were originally chosen as model NPs due to their size, shape and functionality resembling the surface-treated silica. It offers some advantages over silica, most outstandingly the particles are strictly monodisperse and possess a spatially defined functionality while the choice of the functional groups they bear represents a convenient and a relatively easy-to-control tuning parameter of the particle-polymer interaction strength. The affinity of the OP-POSS and OM-POSS particles to polystyrene was estimated according to the chemical composition and verified by a group-contribution calculation of the so-called distance factor Ra based on the Hansen solubility parameters:

$$(Ra)^2 = 4(\delta_{D1} - \delta_{D2})^2 + (\delta_{P1} - \delta_{P2})^2 + (\delta_{H1} - \delta_{H2})^2 \quad (15)$$

where  $\delta_D$ ,  $\delta_P$ , and  $\delta_H$  are the dispersive, polar and hydrogen bonding contributions to the total solubility parameter  $\delta$ , respectively, also referred to as the partial solubility parameters, defined by the equation:

$$\delta^2 = \delta_D^2 + \delta_P^2 + \delta_H^2 \quad (16)$$

The values of POSS-core contribution estimated by Guenther, et al.<sup>245</sup> were applied to access the partial solubility parameters of OM-POSS and OP-POSS listed in the Table 1. It was concluded that OM-POSS and OP-POSS represent nanoparticles with low- and high-affinity to PS, respectively.

**Table 1:** Partial solubility parameters calculated for OM-POSS and OP-POSS.

	$\delta_D$ (J · cm <sup>3</sup> ) <sup>0.5</sup>	$\delta_P$ (J · cm <sup>3</sup> ) <sup>0.5</sup>	$\delta_H$ (J · cm <sup>3</sup> ) <sup>0.5</sup>	Ra (PS) (J · cm <sup>3</sup> ) <sup>0.5</sup>	Ra (toluene) (J · cm <sup>3</sup> ) <sup>0.5</sup>
OM-POSS	14	6	9	15.2	11.5
OP-POSS	21	4	7	3.1	8.4
Toluene <sup>246</sup>	18.0	1.4	2.0	8.3	-
PS <sup>246</sup>	21.3	5.8	4.3	-	8.3

Viscoelastic behavior with a dominant viscous contribution and the loss modulus approximately 1–2 orders of magnitude larger than the storage modulus was found for the polystyrene solution (Fig. 18A). It showed a type III non-linear behavior (weak strain overshoot) with a drop of both storage and loss moduli to near-zero values at approximately 100 % strain amplitude. The accompanying large increase of loss factor  $\tan \delta$  indicated that the loss in elasticity was faster than the loss in viscosity.

The storage and the loss moduli of the POSS/PS nanocomposite solutions were relativized by the corresponding values of the neat polystyrene solution to access the relative contribution

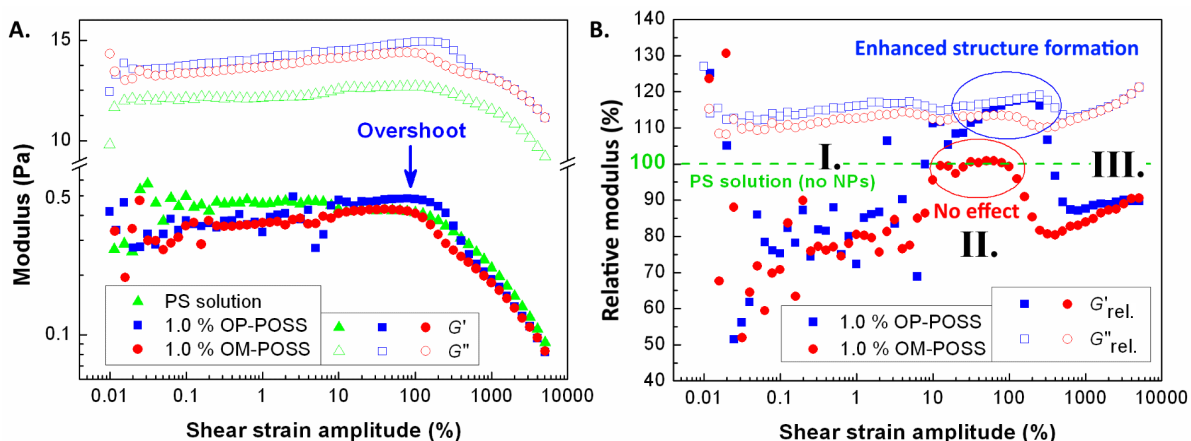


**Fig. 18:** Impact of OM-POSS and OP-POSS NPs on viscoelastic behavior of polystyrene solution in toluene, **(A)** Storage ( $G'$ ) and loss ( $G''$ ) moduli and **(B)** relative storage ( $G'_{rel}$ ) and relative loss ( $G''_{rel}$ ) moduli dependence on shear-strain amplitude. **(I.)** low, **(II.)** intermediate and **(III.)** high strain amplitude regions.

of the NPs (Fig. 18B). Three regimes of rheological response were identified with varying strain amplitude at small (< 10 %), middle (10–100 %) and high-strain amplitudes (> 100 %). The relative loss modulus ( $G''_{rel}$ ) was increased by up to 10–20 % compared to the neat polymer solution nearly independently of the NP type. The relative storage modulus ( $G'_{rel}$ ), on the other hand, manifested nontrivial changes in the elastic contribution to the shear deformation induced by NPs. The data-points for OM-POSS and OP-POSS coincided at small and high strain amplitudes, where the relative storage moduli took values of approximately 80–90 %. This effect was clearly independent of NP-polymer specific interaction. However, at middle strain amplitudes, the strongly interacting OP-POSS particles showed a relative storage modulus of about 118 % while the weakly interacting OM-POSS particles had no significant effect on the elastic contribution. The impact was so pronounced that it shifted the overall rheological response to the type IV (strong overshoot) behavior for the OP-POSS nanocomposite solution.

The type III and IV non-linear behavior, i.e., the weak and strong overshoot, respectively, are both governed by balance of formation and destruction processes in the sheared sample<sup>101</sup>. Hence, the results suggest that within the middle-strain amplitude deformation regime, the OP-POSS NPs enhanced the structure formation tendency and, supposedly, formed stiffened clusters, which increased both the structure formation rate and the relative storage modulus. The OP-POSS/PS nanocomposite solution in toluene fulfills the condition of NP-polymer affinity exceeding that the NP and solvent (Table 1), which is expected for the assembly of chains with NPs to occur. Presumably, the presence of clusters restricted the chain orientation occurring under shear flow, which shifted the border between the middle and the high strain amplitude deformation regime to higher strain-amplitudes (~ 400 % for OP-POSS compared to ~ 100 % for OM-POSS nanocomposite solution). The clusters eventually felt apart at high strain amplitudes and the difference between OP-POSS and OM-POSS NPs vanished. One has to keep in mind that the viscoelastic behavior of these samples was dominated by the viscous contribution; thus, the change in relative storage modulus was overwhelmed by the much higher relative loss modulus.

Varying the OP-POSS concentration led to significant changes in the viscoelastic behavior. Addition of 0.1 % OP-POSS caused a more pronounced gain in the elasticity (up to 65 %) at middle strain amplitudes, as described by the relative storage modulus (Fig. 19A). The gain experienced at small strain amplitudes was likely an artefact due to weak signal. The relative loss modulus was close to the unity except for middle strain amplitudes, where it was elevated by up to 12 %. When compared to the 1 % OP-POSS/PS nanocomposite solution, the low particle content seems to be much more effective in varying the viscoelastic response. The relative loss modulus (Fig. 19A) as well as the relative storage modulus were nearly constant at 10 % OP-POSS, suggesting that at such high concentration, OP-POSS remained uninvolved in cluster formation within the whole studied strain amplitude range. Supposedly, it was addressed to the poor dispersion and the presence of large aggregates, which were manifested by turbidity and loss of transparency in the solid state. The low moduli values were attributed to the preparation protocol as the overall composite mass was kept constant and the amount of polystyrene matrix was 10 % inferior to the pure polystyrene solution.

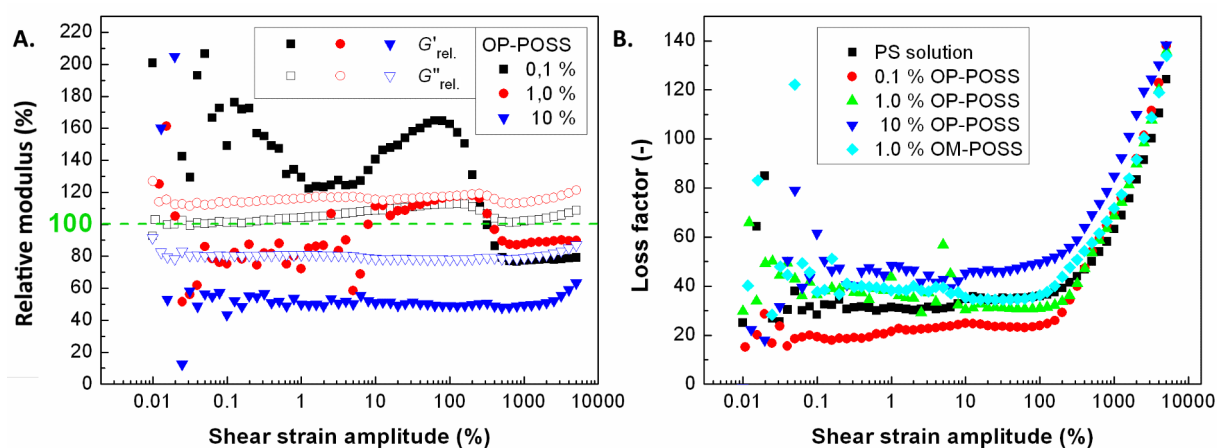


**Fig. 19:** Impact of OP-POSS and OM-POSS on viscoelasticity of polystyrene solution in toluene, **(A)** Relative storage ( $G'_{red}$ ) and relative loss ( $G''_{red}$ ) moduli dependence on shear strain amplitude for varying OP-POSS content, **(B)** Loss factor dependence on shear-strain amplitude.

Another supportive clue for the previous conclusions was provided by the loss factor (Fig. 19B). Decreased values at 0.1 % OP-POSS content at low and middle strain amplitudes evidenced the enhanced elastic properties; however, they did not drop below the value of 15, manifesting the overwhelming dominance of the viscous contribution. Contrary, the elasticity enhancement for the 1 % OP-POSS content was observed only at middle strain amplitudes and it was less pronounced than in the previous case, possibly due to the simultaneous viscosity enhancement. Enhanced viscous behavior prevailed at low and high strain amplitudes. Finally, 10 % OP-POSS enhanced the viscous contribution over the whole investigated range of strain amplitudes.

Despite the promising initial results, the drawbacks of POSS/PS model system proved to outweigh its benefits. Up to now, the particle size was not mentioned. Dynamic light scattering measurements of OP-POSS ultrasonically dispersed in toluene revealed a size-distribution in which the smallest identified value was 2.4 nm. That represents approximately two times the

POSS-unit diameter; however, it is possible that small amount of single stand-alone particles went undetected since the scattering intensity scales with the 6<sup>th</sup> power of the radius and the instrument touches its limit in the range of several nanometers. Anyway, the particle mean-size was established to roughly  $(20 \pm 7)$  nm and clearly manifests the presence of particle assemblages. According to a simple geometrical comparison, such particles contain roughly hundreds to thousands elementary units. These super-particles still fall within the nanoscale range and; therefore, it is not clear whether they should be treated within the reviewed framework rather as primary (undividable) building blocks or as objects composed of elementary particles which could be redistributed during the preparation process. Characterization techniques fall short in aiding to solve this question due to their experimental limitations<sup>247</sup> and the very small dimension of a single POSS nanoparticle. To avoid these difficulties, the further experiments were carried out on another system, i.e., on colloidal silica NPs in PMMA and PS.

## 6.2. Silica/PMMA nanocomposites

As evidenced by the measurements, the silica pre-dispersed in isopropanol remained individually dispersed when added to THF, acetone and ethyl acetate and only small fraction of NPs (~2 mass %) formed aggregates ( $d_{\text{mean}} = 230.8$  nm) in acetone-toluene 1:1. Toluene did not stabilize the NP dispersion though, and a large-scale aggregation and a phase separation occurred.

NP dispersion state in polymer liquid arises from the balance of the solvent–NP, NP–NP, solvent-polymer and NP-polymer interactions and the kinetic conditions of the preparation protocol (shear rate, time of solvent evaporation, viscosity, etc.). By varying the solvent strength, three different nanoparticle organizations were prepared in the silica/PMMA containing a constant NP loading of 1 vol. % (Fig. 20). They were identified as aggregates (Fig. 20A, E), individually dispersed NPs (Fig. 20B–C), and chain bound clusters (Fig. 20D). Mackay et al.<sup>45</sup> proposed hypothesis to quantitatively analyze the state of the NP dispersion in polymer liquids attributed the key role in determining the outcoming NP spatial arrangement to the ratio between the NP radius ( $R_{\text{NP}}$ ) and the polymer radius of gyration ( $R_{\text{G}}$ ). Using different solvents, the  $R_{\text{NP}}/R_{\text{G}}$  ratio varies for the given combination of polymer and NP due to the  $R_{\text{G}}$  varying with the quality of the solvent. To test this hypothesis, the average PMMA coil diameter measured by dynamic light scattering (DLS) was approximately 10.5 nm for all the solvents used in this study at the temperature range covering the blending step of the preparation protocol. The size variation lying within the experimental error was negligible. The coil diameter was always smaller than the NP diameter of  $20 \pm 4$  nm. According to the hypothesis of Mackay et al.<sup>45</sup>,  $R_{\text{NP}}$  larger than the  $R_{\text{G}}$  should result in a poor NP dispersion and, a NP agglomeration should occur. This prediction contradicts the experimental observations presented in this work. However, Mackay et al.<sup>45</sup> investigated PNCs consisting of fullerenes in polyolefin or tightly cross-linked polystyrene nanoparticles in linear polystyrene matrix, i.e. systems with almost “no specific interfacial interactions”. Minimizing or eliminating the role of the adsorption enthalpy undoubtedly leads to the dominance of the entropic factors which in turn relate to the size<sup>248</sup>. Previous studies has already suggested the importance of the interaction balance between the components, i.e. particle-polymer-solvent, on the NP spatial

organization<sup>27,50,63</sup> but the current experimental results clearly show that adsorbing PNC solutions do not conform to the simple prediction based on the NP-polymer coil relative size.

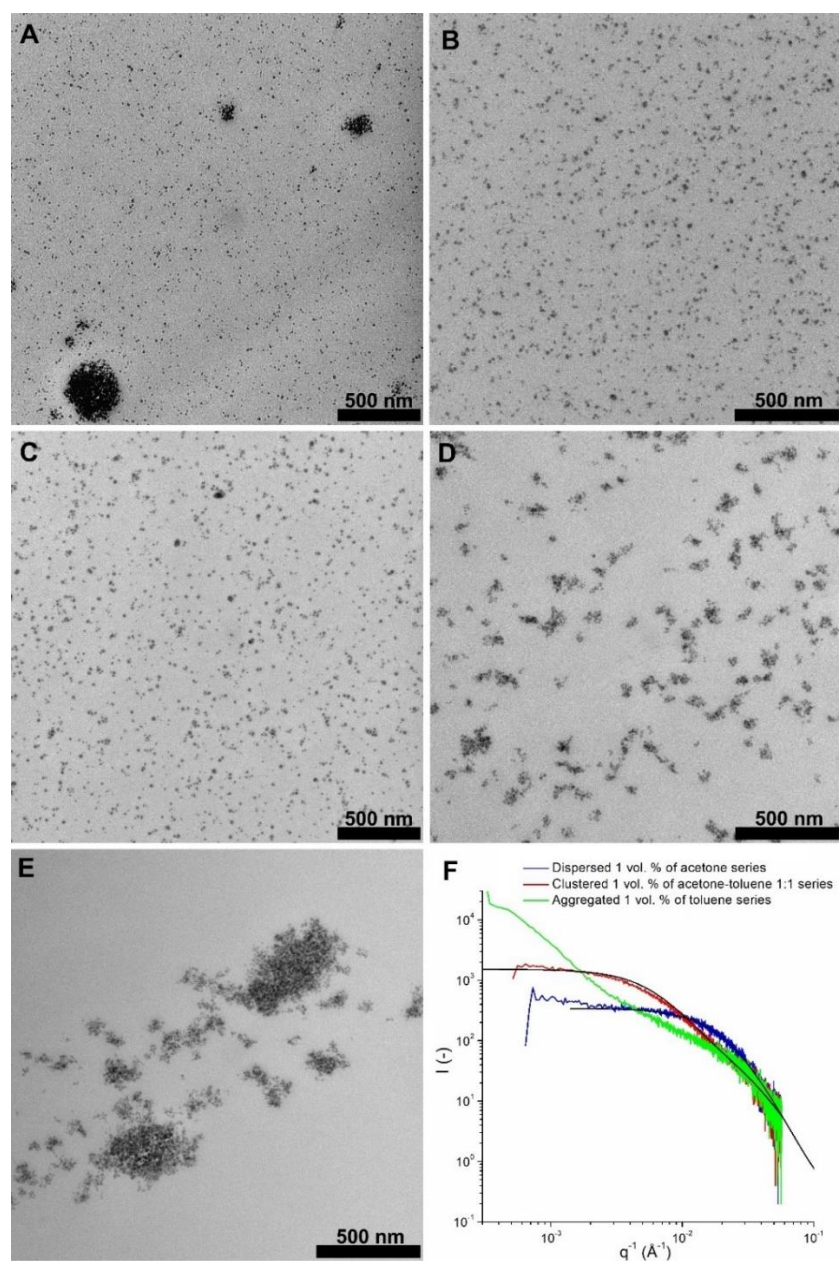


**Fig. 20:** TEM images (magnification 44 000 $\times$ ) of 1 vol. % nanosilica/PMMA nanocomposites with various structure prepared from (A) THF, (B) acetone, (C) ethyl acetate, (D) acetone-toluene 1:1 mixture, and (E) toluene. (F) USAXS dependence of the intensity  $I(-)$  on the length of the scattering vector  $q$  extracted from USAXS data for PNC samples with NP loading of 1 vol. %. The black lines represent fits for dispersed and clustered nanostructures.

The observed systematic changes in NP spatial organization were related to the solvent properties. Interestingly, the spatial organization states followed the same order as was predicted by Schweizer<sup>63</sup> for NPs immersed in adsorbing polymer melt, i.e., aggregated-dispersed-clustered. It shall be noted that the processing before the structure evaluation

involved a prolonged annealing (6 days at 140 °C) which did not erase the specific NP organizations. While annealing was previously reported to enhance a NP dispersion in the case of a favorable NP-polymer interaction, there are substantial differences in the extent of the improvement that could be achieved. The most profound changes were reported for grafted NPs<sup>40,56,249</sup> while the presence of small contact aggregates held together by the Van der Waals interactions is not effectively eliminated by annealing<sup>50</sup>. Hence, if NP agglomerates are initially formed, they could not be easily broken by annealing, despite their repositioning may slightly improve the overall dispersion.

Individually dispersed particles were observed in TEM images of PNC samples prepared from acetone (Fig. 20B) and ethyl acetate (Fig. 20C). The USAXS analysis of the PNC prepared from acetone confirmed the spatial organization consisting of individual particles dispersed in the matrix due to the flat low  $q$  region and the smoothly decreasing intermediate  $q$  region (Fig. 20F). Both methods yielded an average element diameter about 20 nm which matches well with the size of an individual NP.

Chain bound clusters (Fig. 20D) were formed using the 1:1 acetone-toluene mixture solvent. Three populations of cluster sizes were found alongside less frequent single particles. The smallest clusters contained 2 to 3 particles (the least frequent occurrence), the intermediate clusters contained 5 to 9 NPs, and the large clusters consisted of 16 to 26 particles (the most frequent occurrence). Theoretical models<sup>27</sup> suggest a gradual increase of the cluster size with time assuming that individual particles form small clusters consisting of two to three nanoparticles and once formed, these elementary clusters connect to build up larger clusters. An evidence of gradual cluster formation was indeed observed as will be discussed later. The USAXS results showed a complex behavior in the low and the intermediate  $q$  regions (Fig. 20F), indicating the presence of two scattering populations which confirms that the PNC contained internally structured inclusions – clusters with size of ~45 nm and primary building blocks with size of 20 nm.

Finally, preparing the PNC utilizing THF (Fig. 20A) or toluene (Fig. 20E) resulted in aggregates of NPs in a close contact with the average aggregate size of approximately 400 and 500 nm, respectively. In THF, a fraction of NPs remained individually dispersed alongside the aggregates, but it will be referred to this NP organization type as “aggregated” for simplicity and to highlight the presence of the large NP ensembles. The USAXS profiles of PNC prepared from toluene also revealed a presence of big and small populations of multi-NP agglomerates of a size larger than 100 nm. However, the origin of the aggregation in THF and toluene shares little in common and derives from two very different processes as will be described below.

TEM micrographs were subjected to image analysis to provide additional information on the NP arrangement. The results of manual image analysis for 1 and 5 vol. % of silica in PMMA prepared from acetone and acetone-toluene 1:1 are presented in the Fig. 21. The pair correlation function of NP separation was computed by normalizing the experimental data to the random distribution probability (Fig. 21C). Clearly, the solution blending in acetone favors

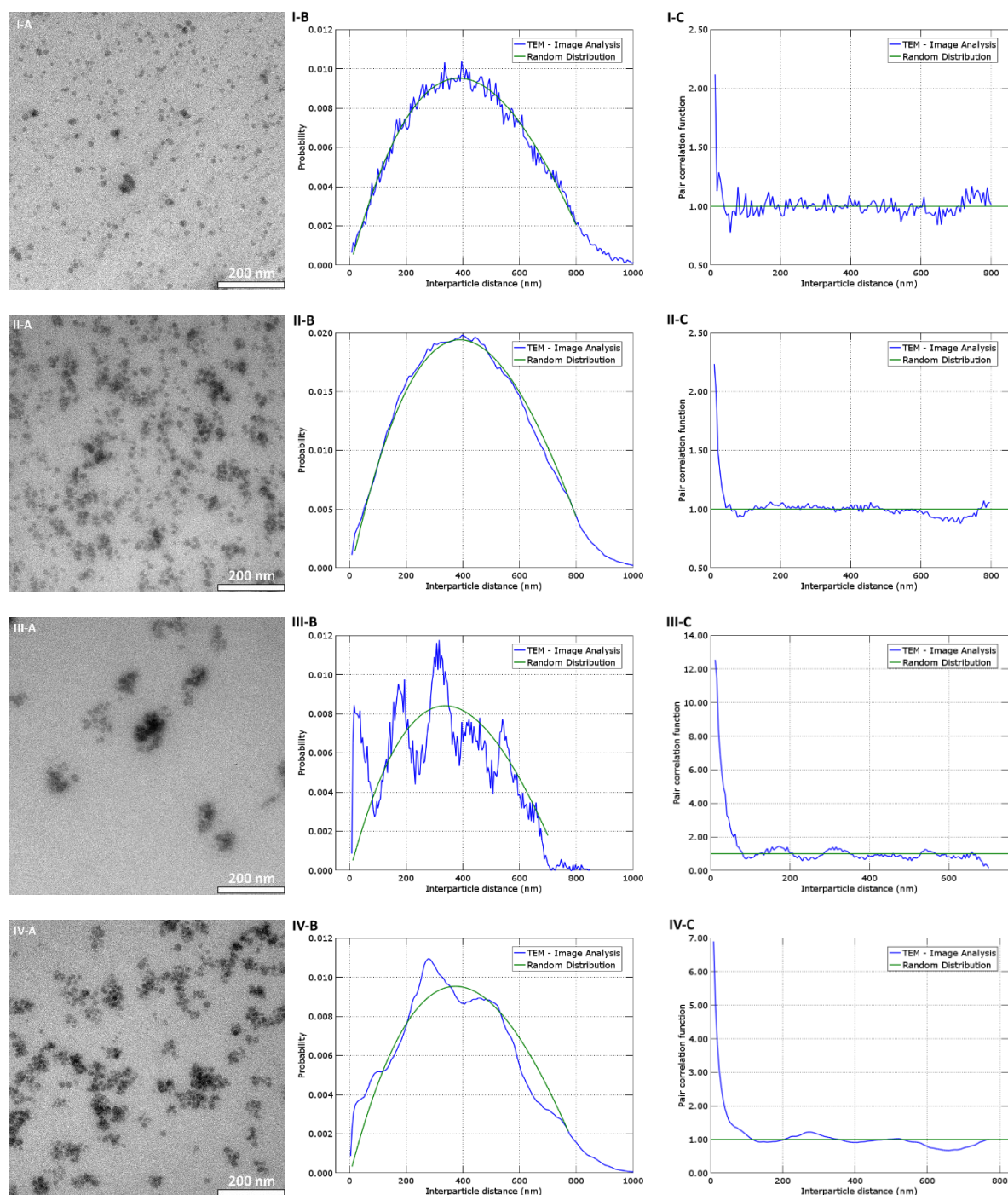


**Fig. 21:** Structural analysis of silica in PMMA P8N, **(A)** TEM image at magnification 110 000 $\times$ , **(B)** Probability distribution of interparticle distances in the TEM image and **(C)** pair correlation function of interparticle distances based on manual image analysis; **(I)** 1 vol. % silica, acetone, **(II)** 5 vol. % silica, acetone, **(III)** 1 vol. % silica, acetone-toluene 1:1, **(IV)** 5 vol. % silica, acetone-toluene 1:1.

dispersion since the experimental probability distribution of the interparticle distances in the Fig. 21 I.B conforms well to the random distribution except for very low separations. The discrepancy clearly suggests presence of small NP ensembles. However, it was beyond the

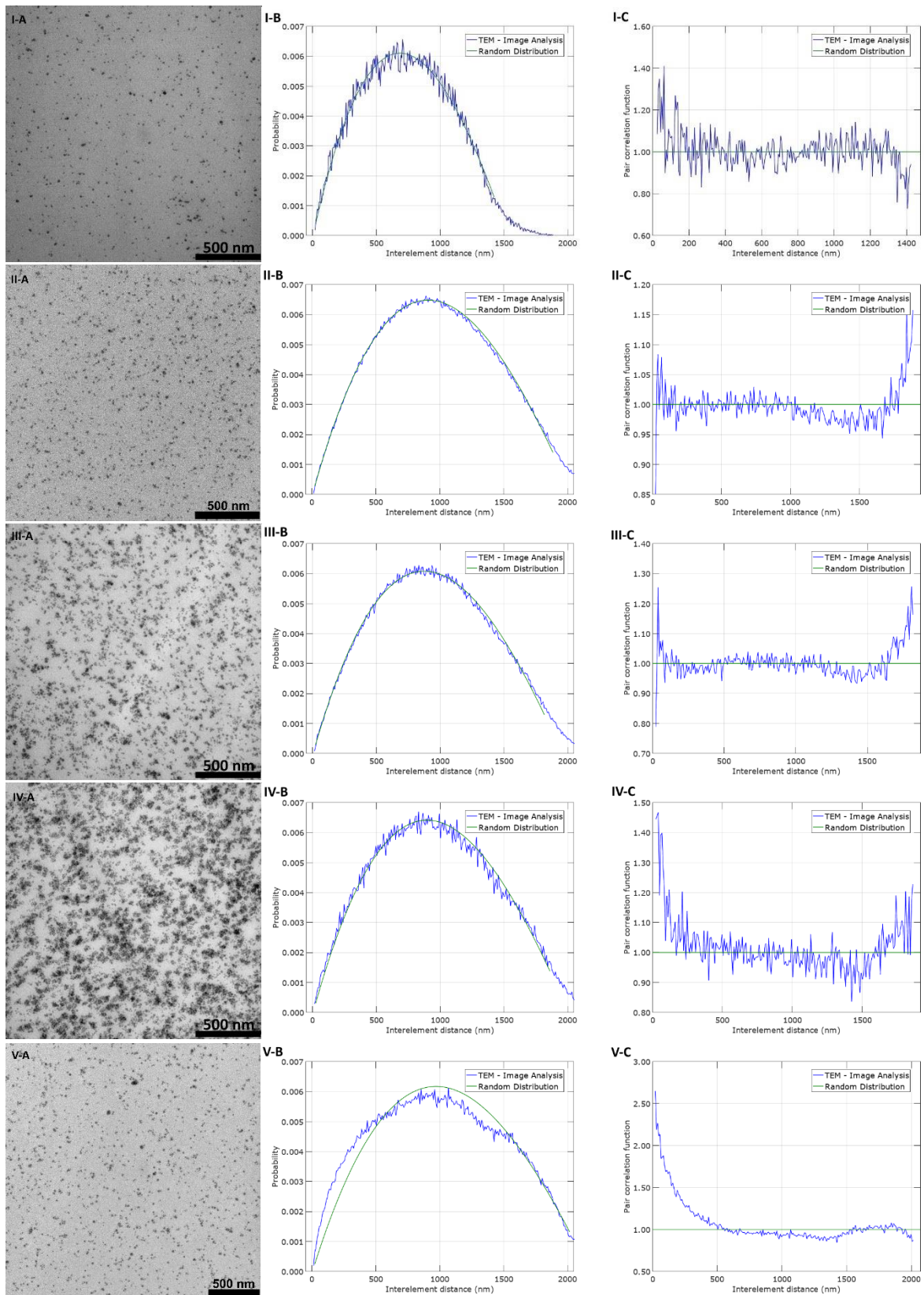
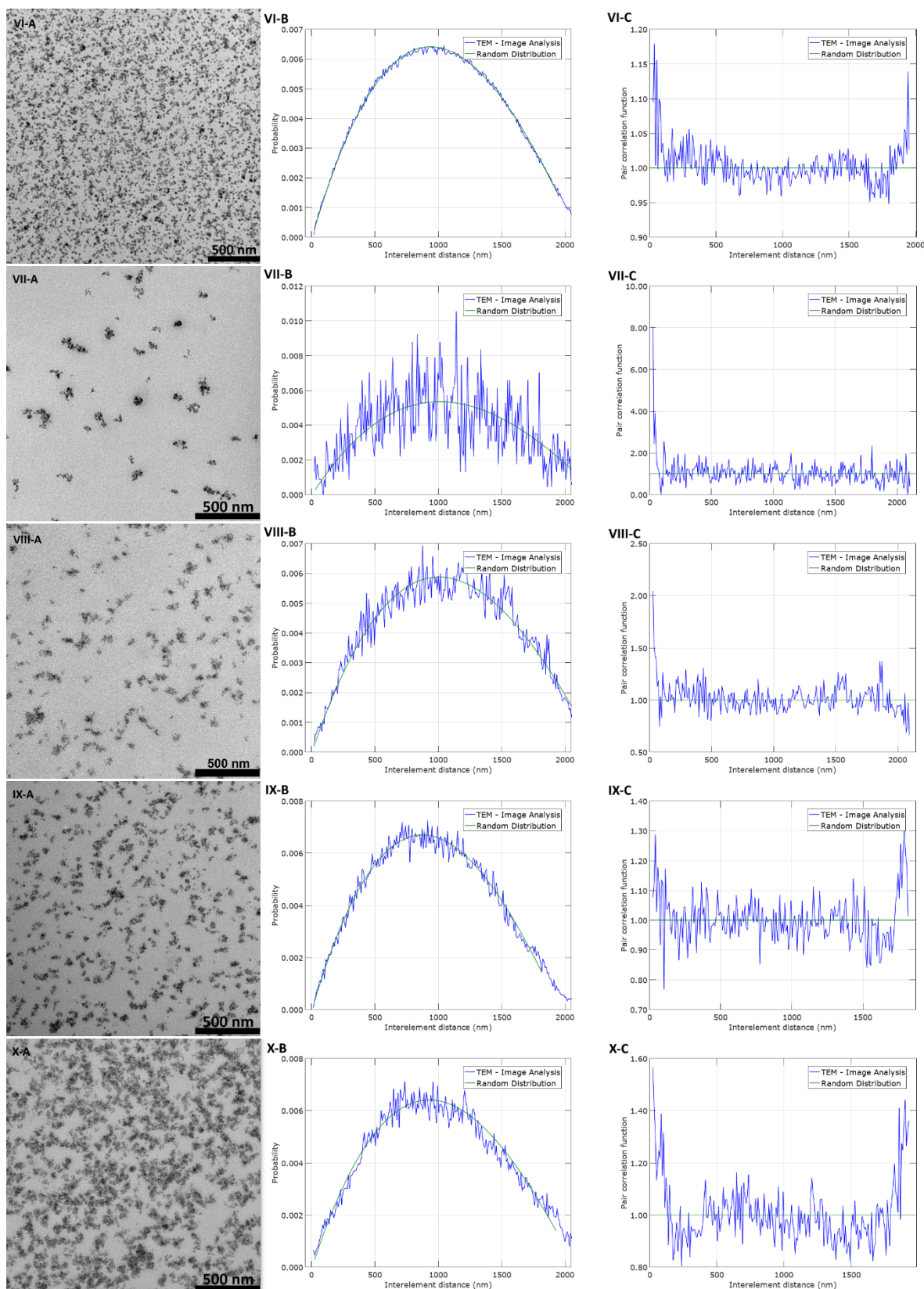


**Fig. 22:** Structural analysis of silica/PMMA PNCs. **(A)** TEM image at magnification 44 000 $\times$ , **(B)** Distribution of interelement distances, **(C)** NP pair correlation function; samples prepared from



**(I–IV)** acetone with 0.5, 1, 5, and 10 vol. % NPs, respectively, **(V–VI)** ethyl acetate with 1, and 5 vol. % NPs, respectively, **(VII–X)** acetone-toluene 1:1 mixture with 0.5, 1, 5, and 10 vol. % NPs, respectively.

limit of the instrumentation to determine whether these are chain bridged, or aggregated NPs and the decisive evidence needs to be searched elsewhere. The partial replacement of acetone by toluene as the solvent in the processing step introduces NP association (Fig. 21 III.A, IV.A). The interparticle separation distribution reveals that the NP ensembles are on average 48.3 nm large and about 120–150 nm apart from each other. These results fairly agree with the findings of the automated image analysis which provides credibility to the automated evaluation process (Fig. 22). The ratio of the interelement distance (Fig. 23A) to the element diameter (Fig. 23B) conformed well to the random distribution<sup>30</sup> for all the evaluated samples within the whole investigated concentration range (Fig. 23C). It validates the idea that aggregates/clusters shall be regarded as sovereign entities randomly dispersed in the polymer matrix and that a balance was established between their size and the separation distance, likely during the annealing phase of the processing.

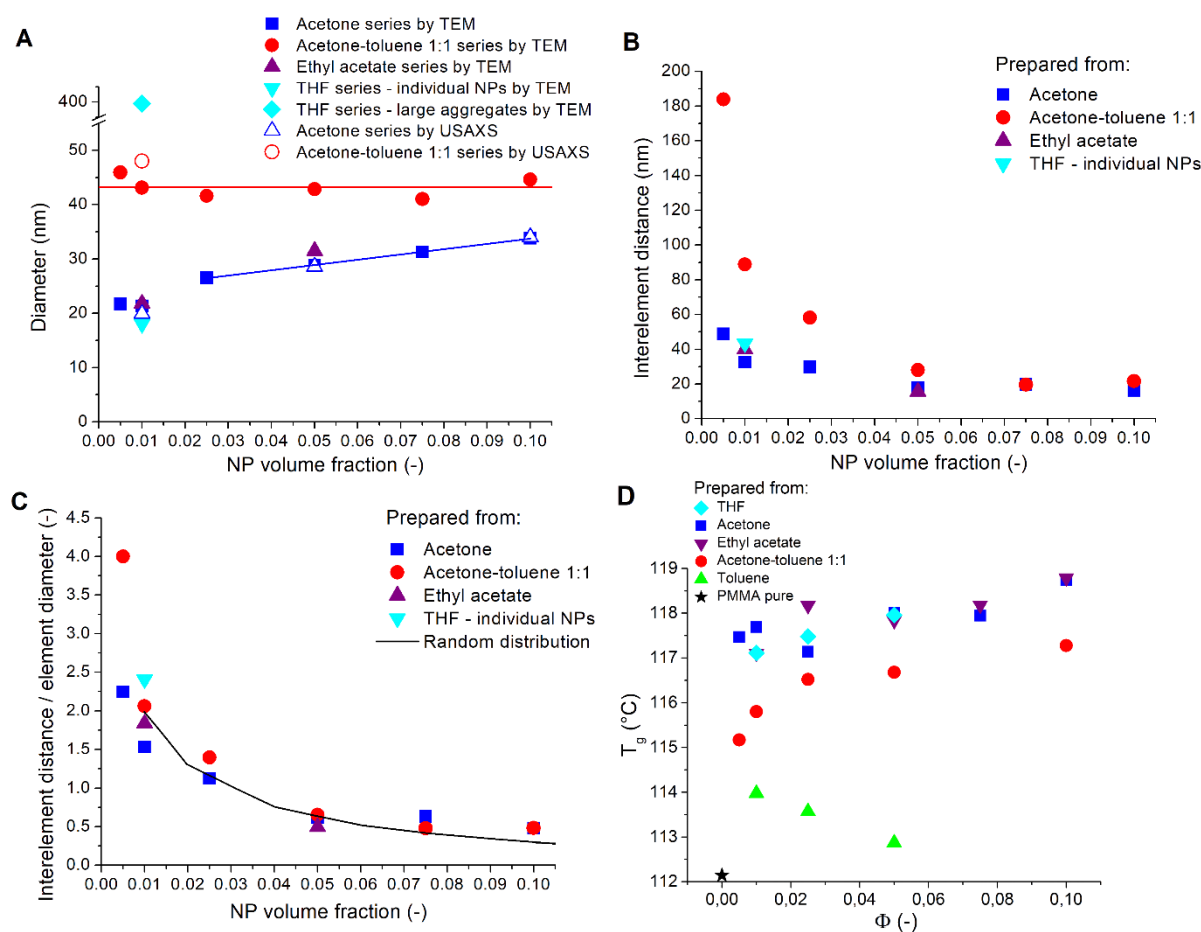


**Fig. 23:** Dependence of (A) element diameter according to the TEM and the USAXS, (B) interelement distance of 5 nearest neighbors determined from the automated image analysis of the TEM snapshots, and (C) interelement distance of 5 nearest neighbors divided by element diameter on NP volume fraction in solid state PNCs prepared from acetone, acetone-toluene 1:1 mixture, ethyl acetate and THF. Values for random distribution taken from the ref. 30 (D) Glass transition temperature as a function of NP volume fraction for various NP structures.

The distance parameter  $Ra$  (eq. 15) of PMMA/acetone and PMMA/acetone-toluene 1:1 mixture takes values of 6.30 and 6.69, respectively<sup>246</sup> or, for another set of solubility parameters,<sup>250</sup> equals to 5.50 and 5.35, respectively. In both cases, the overall interactions are nearly similar, which agrees with the expectation that the final NP dispersion is not directly tied to the quality of the solvent respective to the polymer theta condition<sup>51</sup>. However, polar contribution is more favored in acetone while the dispersion contribution prevails in acetone-toluene 1:1 mixture. Obviously, the tremendous structuring impact of the solvent must be caused by another mechanism. We propose that it is the solvent interaction with NPs which governs the resulting NP spatial organization. The solubility parameter concept was originally developed in organic chemistry, and, thus, values for silica NPs are not readily available in literature. Therefore, we present procedure to estimate the value of the solubility parameters for silica. As described above, polymer is desorbed from silica surface upon addition of a co-solvent – displacer - at the critical volume fraction  $\varphi_c$ . Partial solubility parameters,  $\delta_{part.}$ , of the solvent-mixture is calculated as the average of both components weighed by the respective volume fractions:

$$\delta_{part,mix} = \varphi_c \delta_{part,d} + (1 - \varphi_c) \delta_{part,s}, \quad (17)$$

where the subscripts 'mix', 'd' and 's' regard to the mixture, displacer and solvent, respectively. At the critical displacer volume fraction, it is expected that the silica affinity to polymer equals its affinity to the medium (solvent-displacer mixture), therefore:

$$Ra_{(silica/polymer)}^2 = Ra_{(silica/medium)}^2, \quad (18)$$

$$\begin{aligned} 4(\delta_{D,S} - \delta_{D,p})^2 + (\delta_{P,S} - \delta_{P,p})^2 + (\delta_{H,S} - \delta_{H,p})^2 \\ = 4(\delta_{D,S} - \delta_{D,mix})^2 + (\delta_{P,S} - \delta_{P,mix})^2 + (\delta_{H,S} - \delta_{H,mix})^2, \end{aligned} \quad (19)$$

where the subscripts 'S' and 'p' refers to silica and polymer respectively. Expanded and rearranged, the equation yields:

$$A \cdot \delta_{D,S} + B \cdot \delta_{P,S} + C \cdot \delta_{H,S} = D, \quad (20)$$

$$A = 8(\delta_{D,p} - \delta_{D,mix}); B = 2(\delta_{P,p} - \delta_{P,mix}); C = 2(\delta_{H,p} - \delta_{H,mix}), \quad (21)$$

$$D = 4\delta_{D,p}^2 - 4\delta_{D,mix}^2 + \delta_{P,p}^2 - \delta_{P,mix}^2 + \delta_{H,p}^2 - \delta_{H,mix}^2 \quad (22)$$

which is a three-variable linear equation and could be solved for three independent sets of parameters  $A$ ,  $B$ ,  $C$  and  $D$ . The silica dispersive ( $\delta_{D,S}$ ), polar ( $\delta_{P,S}$ ) and hydrogen bonding ( $\delta_{H,S}$ ) partial solubility parameters were calculated for each combination of 3 displacers of PMMA in carbon tetrachloride out of 6 available<sup>93</sup> and yielded values of  $(18.8 \pm 1.0) (\text{J} \cdot \text{cm}^{-3})^{0.5}$ ,  $(5.7 \pm 0.8) (\text{J} \cdot \text{cm}^{-3})^{0.5}$  and  $(6.3 \pm 0.8) (\text{J} \cdot \text{cm}^{-3})^{0.5}$ , respectively (Table 2). Since the solubility parameter was originally defined as the square root of the cohesion energy density<sup>246</sup>, the cohesion energy of silica could be calculated by multiplying the solubility parameter (Eq. 16) with the silica molar volume ( $24 \text{ cm}^3 \cdot \text{mol}^{-1}$  for  $\beta$ -quartz at  $848 \text{ K}^{251}$ ) to yield the value of  $11.6 \text{ kJ} \cdot \text{mol}^{-1}$ . The estimate is much lower than the cohesion energy of quartz ( $6.52 \text{ eV} \approx 629.0 \text{ kJ} \cdot \text{mol}^{-1}$  for the  $\alpha$ -modification<sup>252</sup>) but the adsorption related processes on the nanosilica surface are not prone to change the silica molecular structure; hence, a much weaker interaction lessened by the crystallization energy is expected compared to bulk quartz.

Moreover, the calculated value of the silica cohesion energy lies on the same scale as the PMMA-silica interaction strength ( $16.7 \text{ kJ}\cdot\text{mol}^{-1}$ ), as shown below. This renders both the observed NP aggregation as well as the expected PMMA adsorption energetically feasible regarding the solvent choice and fortifies the correctness of the calculation. The results also support the expectation of the dominant dispersive factor with a strong polar and hydrogen bonding, which was previously observed for silica<sup>93</sup>. However, use of some displacers led to apparently incorrect results and had to be omitted.

**Table 2:** The input data and the results of the silica partial solubility parameters computation, the letters (S) and (D) mark the solvent and the displacer, respectively. The solubility parameters of the solvent, the displacers and PMMA were taken from the ref. 246 unless otherwise stated.

	$\delta_D$ ( $\text{J}\cdot\text{cm}^{-3}$ ) <sup>0.5</sup>	$\delta_P$ ( $\text{J}\cdot\text{cm}^{-3}$ ) <sup>0.5</sup>	$\delta_H$ ( $\text{J}\cdot\text{cm}^{-3}$ ) <sup>0.5</sup>	$\varphi_c$ <sup>93</sup> (-)
Carbon Tetrachloride (S)	17.8	0	0.6	–
Acetone (D)	15.5	10.4	7.0	0.39
Acetonitrile (D)	15.3	18.0	6.1	0.32
Dioxane (D)	19.0	1.8	7.4	0.39
Ethyl Acetate (D)	15.8	5.3	7.2	0.85
Pyridine (D)	19.0	8.8	5.9	0.26
Tetrahydrofuran (D)	16.8	5.7	8.0	0.53
PMMA	18.6	10.5	7.5	–
PMMA <sup>250</sup>	18.1	10.5	5.1	–
Silica	$18.8 \pm 1.0$	$5.7 \pm 0.8$	$6.3 \pm 0.8$	–

In fact, the interfacial interactions of silica NPs in PMMA solution are dominated by the acid–base interactions between acidic silanol groups on silica and basic groups of PMMA and solvents<sup>253–257</sup>. The addition enthalpies were calculated according to the semi-empirical equation originally proposed by Drago, et al.<sup>258</sup> and later extended by Fowkes, et al.<sup>253–257</sup> for polymers:

$$-\Delta H = E_A E_B + C_A C_B \quad (23)$$

where the parameters  $E$  and  $C$  denote the susceptibility of the acid (A) and the base (B) to undergo the electrostatic interaction and form covalent bonds, respectively. Fowkes, et al.<sup>253–257</sup> found that a strong competition for the acidic moieties on the filler surface exists between a basic solvent and a basic polymer such as PMMA, while an acidic solvent would compete with acidic filler surface for basic functional groups of the polymer<sup>25</sup>. The  $E$  and  $C$  values used for the calculation of the addition enthalpies are listed in the Table 3.

**Table 3:** Overview of the  $E$  and  $C$  values according to the Drago's concept for silica and various bases<sup>257,258</sup> and calculated addition enthalpies  $-\Delta H_{\text{add}}$  onto silica for the listed bases. \*Values obtained as the average of the data for benzene and *p*-xylene. \*\*Value obtained as the average of the data for acetone and toluene.

Acid	$C_a$	$E_a$	
silica	1.08	4.36	
Bases	$C_b$	$E_b$	$\Delta H_{\text{add}}$ on silica (kcal·mol <sup>-1</sup> )
PMMA	0.96	0.68	-4.0
THF	4.27	0.978	-8.9
DMF ( <i>N,N</i> -dimethylformamide)	2.48	1.23	-8.0
acetone	2.33	0.987	-6.8
ethyl acetate	1.74	0.975	-6.1
benzene	0.71	0.486	-2.9
<i>p</i> -xylene	1.78	0.416	-3.7
toluene	1.24*	0.45*	-3.3
acetone-toluene 1:1	–	–	-5.1**

The calculated enthalpies of the donor–acceptor interactions for the model PNCs are shown in the Fig. 24A. The highest value of the negative addition enthalpy  $-\Delta H_{\text{add}}$  in this study is found between THF and silanol groups on the silica surface ( $8.9 \text{ kcal}\cdot\text{mol}^{-1} \approx 37.1 \text{ kJ}\cdot\text{mol}^{-1}$ ), which is significantly stronger than the attraction between PMMA and silica ( $4.0 \text{ kcal}\cdot\text{mol}^{-1} \approx 16.7 \text{ kJ}\cdot\text{mol}^{-1}$ ). In combination with the large excess of the solvent over the polymer, it suggests that the adsorption onto silica is dominated by THF and a strong solvation shell is formed around NPs which, in turn, repels polymer chains from the vicinity of the NPs and causes NP aggregation due to the depletion attraction. The negative addition enthalpy of silica to acetone ( $6.8 \text{ kcal}\cdot\text{mol}^{-1} \approx 28.5 \text{ kJ}\cdot\text{mol}^{-1}$ ) and ethyl-acetate ( $6.1 \text{ kcal}\cdot\text{mol}^{-1} \approx 25.6 \text{ kJ}\cdot\text{mol}^{-1}$ ) is smaller than to THF but still exceeds that of the silica-PMMA couple. Since solvent molecules are the enthalpically favored adsorbate, the stabilization responsible for the experimentally observed dispersion of individual NPs is likely contributed by a colloidal-like solvation effect besides the previously suggested<sup>45</sup> polymer-NP attraction induced repulsion of the adsorbed polymer shells. However, despite the NPs were preserved isolated in the ethyl acetate (Fig. 22 V-A), slight distortion from the random distribution (Fig. 22 V-B, C) manifests an emerging loss of particle stability which eventually prevails at weaker NP-solvent interaction strength or at higher particle loading (see below). Unlike in the previous studies using an extremely slow solvent removal<sup>50</sup>, the dispersion of isolated NPs obtained in the current experiments is maintained through a relatively fast solvent evaporation at 140 °C upon the PNC solidification. Gradually removing acetone or ethyl acetate from the liquid PNC to the point where NPs are expected to start the contact agglomeration, neighboring polymer chains enhance their

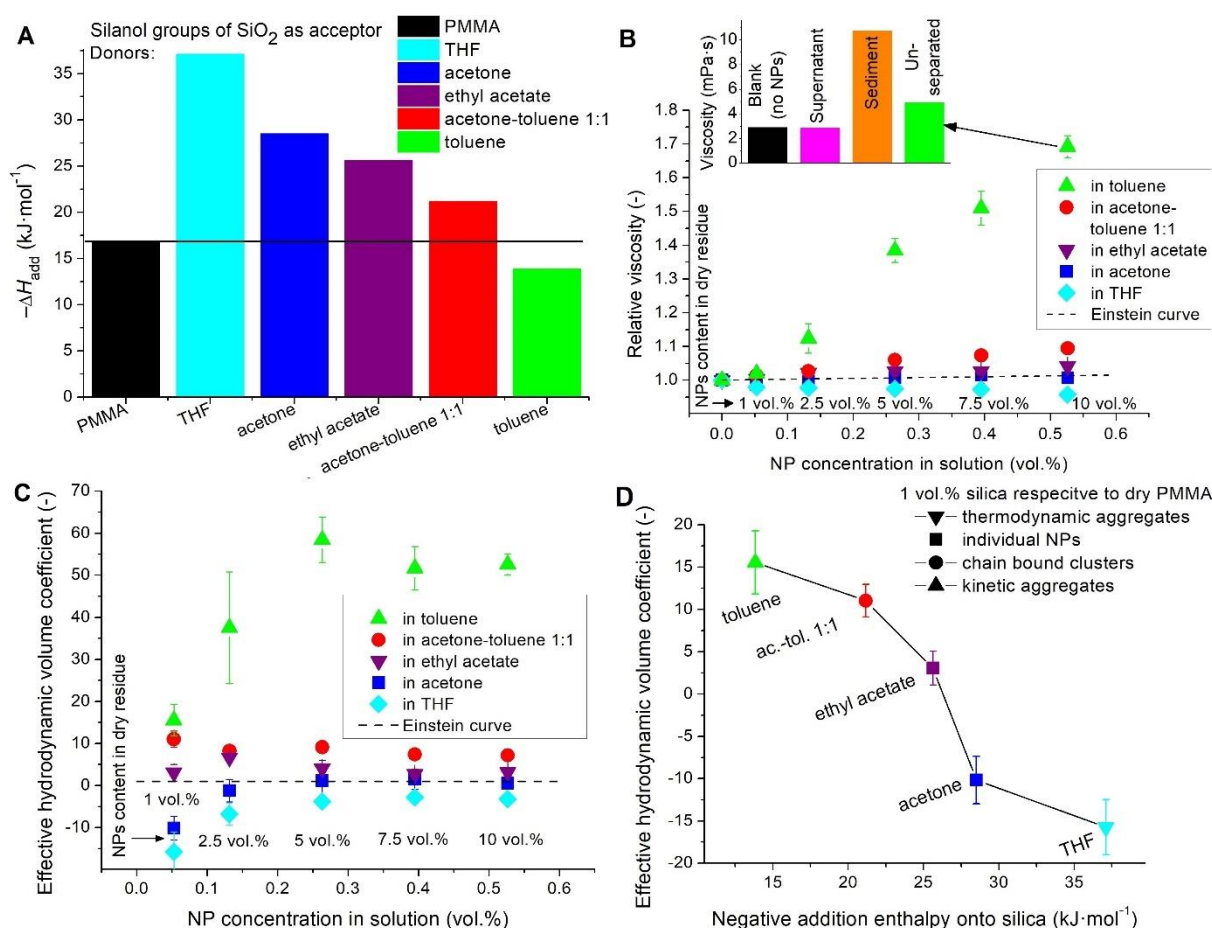


**Fig. 24:** (A) Bar diagram of the donor-acceptor addition enthalpies  $-\Delta H_{add}$  of silanol groups of SiO<sub>2</sub> nanoparticles with PMMA and various solvents. The dependence of (B) the relative viscosity and (C) the effective hydrodynamic volume coefficient on the nanoparticle concentration in 5.3 vol. % solution of PMMA in various solvents with a clearly distinguishable behavior with regard to the NP spatial organization. The inset in (B) compares viscosities of the phases separated from the indicated sample by decantation. (D) Variation of the effective hydrodynamic volume with the negative addition enthalpy  $-\Delta H_{add}$  of solvent onto silica for 1 vol. % silica (relative to dry PMMA) in 5.3 vol. % PMMA solution in various solvents. Symbols indicate the solid-state NP dispersion while colors match the solvents in A–C.

chances in the competition with solvent molecules for the adsorption onto the NP surface. Viscosity of the liquid PNC progressively increases what significantly slows down the NP diffusion and, thus, reduces their ability to agglomerate. This explains the previously reported experimental results<sup>50</sup> stating that a fast solvent evaporation often improves NP dispersion.

The strength of the interaction between the 1:1 acetone-toluene mixture and silica ( $5.1 \text{ kcal}\cdot\text{mol}^{-1} \approx 21.2 \text{ kJ}\cdot\text{mol}^{-1}$ ) prevented the contact agglomeration; however, it was not sufficient to stabilize the dispersion of individual NPs. Since the PMMA-silica attraction is only slightly weaker than that between silica and the solvent mixture, PMMA chains may locally replace the solvent and adsorb onto the NP surface. This balanced competition between the polymer and solvent adsorption is proposed as the mechanism by which the chain bound NP

clusters are formed (Fig. 20D). The low negative enthalpy of addition between toluene and silica ( $3.3 \text{ kcal}\cdot\text{mol}^{-1} \approx 13.8 \text{ kJ}\cdot\text{mol}^{-1}$ ) is reflected by the inability of the solvent to stabilize the dispersed NPs by solvation what leads to the contact agglomeration. The strength of the attraction between PMMA and silica is greater than that for the toluene-silica interaction ( $3.3 \text{ kcal}\cdot\text{mol}^{-1} \approx 13.8 \text{ kJ}\cdot\text{mol}^{-1}$ ) which suggests that the polymer adsorption onto the NP surface takes place as a competitive process to the contact aggregation since the weak toluene-silica interaction is incapable to stabilize the predispersed NPs. The competition is manifested by the presence of two populations of ensembles in the TEM images (Fig. 20E).

The currently presented conclusions correlate well with the previous experimental findings which reported a worsened dispersion or “clusters” of silica/PMMA PNC blended in N,N-dimethylformamide (DMF)<sup>40,249</sup>. The  $-\Delta H_{\text{add}}$  of the DMF-silica couple ( $8.0 \text{ kcal}\cdot\text{mol}^{-1} \approx 33.4 \text{ kJ}\cdot\text{mol}^{-1}$ ) is weaker than for THF-silica ( $8.9 \text{ kcal}\cdot\text{mol}^{-1} \approx 37.1 \text{ kJ}\cdot\text{mol}^{-1}$ ) but stronger than for acetone-silica ( $6.8 \text{ kcal}\cdot\text{mol}^{-1} \approx 28.5 \text{ kJ}\cdot\text{mol}^{-1}$ ) and a somewhat compromised NP dispersion could be expected. Speculatively, the trend outlined by the current conclusions also matches the good dispersion observed for poly(2-vinylpyridine) (P2VP)/silica blended in methyl ethyl ketone (MEK) and the aggregates formed from pyridine<sup>50</sup> since the latter solvent exhibits a very high  $-\Delta H_{\text{add}}$  of the adsorption onto silica ( $12.0 \text{ kcal}\cdot\text{mol}^{-1} \approx 50.2 \text{ kJ}\cdot\text{mol}^{-1}$ ), whereas the addition enthalpy of MEK could be expected similar to that of acetone (exact values not available). However, the lacking  $E$  and  $C$  values for P2VP, which cannot be easily estimated since polymers could not be simply approximated by their monomer units<sup>257</sup>, prevents an exact assessment of this behavior.

While not capable to directly determine the final structure, rheological data (Fig. 24B) provides valuable supplementary information that sheds new light to the structuring phenomena. In the simplest form, the relative viscosity  $\eta_r$  of a dilute suspension of monodisperse spheres is predicted by the Einstein’s formula and is only relevant to the particle hydrodynamic volume, i.e., the effective volume of hydrodynamic constraints experienced by the flow due to the presence of the particles. The hydrodynamic volume typically accounts for the combined volume of bare particles  $\varphi$  and various solvation effects. If those two contributions are separated, the latter is usually merged with the Einstein’s constant and referred to as the intrinsic viscosity or it could be described as the effective hydrodynamic volume coefficient  $k$  (Fig. 24C), defined as the ratio of the intrinsic viscosity and the Einstein’s value of 2.5 (Eq. 8). The effective volume could be comprehended as the volume required to address the actual viscosity regarding the volume fraction of bare particles in the constraints of the Einstein’s equation where the value of 1 relates to systems obeying the Einstein’s formula whereas smaller and larger values pertain to the sub- and super-Einstein behavior, respectively. All three cases are eligible and strongly correlated to the structure of polymer nanocomposite fluid<sup>53</sup>.

A systematic S-shaped decrease of the effective hydrodynamic volume coefficient with the increasing  $-\Delta H_{\text{add}}$  of the solvent adsorption onto the silica was observed (Fig. 24D). The data reflects a shift from the favorable polymer adsorption at large positive  $k$  in weakly interacting solvents such as toluene or acetone-toluene 1:1 mixture to the prevalent depletion attraction

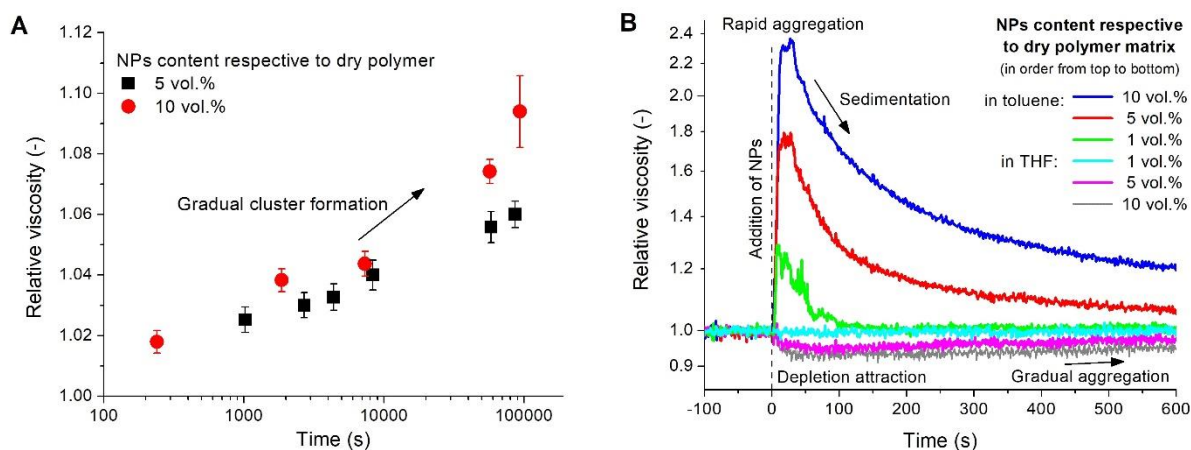


**Fig. 25: (A)** A slow formation kinetics of chain-bound NP clusters in 5.3 vol. % PMMA solution in acetone-toluene 1:1 mixture. Each point represents an independent sample. **(B)** A more rapid formation of kinetical and thermodynamic aggregates in 5.3 vol. % PMMA solution in toluene and THF, respectively. The former is accompanied by a rapid gain in the relative viscosity due to the evolved structures whereas the latter is manifested by a less pronounced decrease of the viscosity due to the depletion attraction which partially diminishes as the aggregation proceeds. Each line represents an average of two independent measurements in which predispersed NPs were added directly into the rheometer geometry. The logarithmic scale is employed to better visualize the comparison of both processes.

at large negative  $k$  in high-affine acetone and THF. Notably, no systematic trend between the value of  $k$  or the final NP dispersion and the dielectric properties nor zeta potentials of THF ( $\epsilon_r = 7.58$ ,  $\zeta = -7.54$  mV), acetone ( $\epsilon_r = 20.7$ ,  $\zeta = -32.9$  mV), ethyl acetate ( $\epsilon_r = 6.02$ ,  $\zeta = -7.45$  mV), and toluene ( $\epsilon_r = 2.38$ ,  $\zeta = -5.01$  mV) was observed. Clearly, the agglomeration in THF and toluene are two unlike processes of dissimilar origin since the interaction strengths of both solvents with silica stand on the opposite sides of the range investigated in this work. The kinetics of both processes was recorded by adding predispersed NPs directly into the rheometer geometry (Fig. 25B). In THF, the initial drop in the relative viscosity partially smeared out over the time what reflects the declining depletion attraction as the effective surface area of the NPs decreased with the proceeding aggregation. Simultaneously, the aggregation also prolonged the mean separation distance that further promoted the stability of the remaining NPs. The combined presence of aggregates and individual NPs suggests a nucleation mechanism of the aggregate growth in THF where the process is kinetically limited by the number of the available nuclei which attract single NPs from their vicinity until a certain critical size is reached or, speculatively, the aggregation tendency is exhausted. The slight increase of the relative viscosity is highly unlikely attributed to the solvent evaporation since it was not present in blank samples, i.e., polymer solution without NPs. In toluene, the agglomeration took place rapidly, practically instantly. The observed change was completed in about the same time ( $\sim 2$  s) as was required for mixing the predispersed NPs into the polymer solution with a pipette which means that the process is presumably kinetically controlled by the rate of NP addition. The following decay of the viscosity was caused by a sedimentation of large agglomerates which rendered them unavailing to the concentric cylinder geometry. A

fully sedimented sample was decanted and the phases were tested separately but no presence of NPs was found in the supernatant by thermogravimetric analysis while its viscosity was slightly reduced compared to the pure polymer solution (Fig. 24B inset), suggesting that the NPs separated into a viscous particle-rich phase thick with polymer. The high recorded viscosity of unseparated samples is in fact an intermediate value of these two phases and as such was inadequate to be addressed by the simple approach based on the Einstein's formula. The phase separation correlates well with the deteriorated homogeneity of the NP distribution observed in the TEM images.

Acetone-toluene 1:1 mixture has the second weakest interaction with silica out of the investigated solvents but unlike the rapid contact agglomeration in toluene, the relative viscosity of the cluster forming nanocomposite solutions gradually rose with time (Fig. 25A). The relative increment exceeded the prediction of the Einstein's equation nearly ten times after one day (Fig. 24B–C). Considering an even spacing of the additional hydrodynamic volume around each particle, the NPs in clusters would have to be enlarged by about 19–22 nm in the diameter to ascribe the excess viscosity. Despite this approach being over simplistic, it draws a conclusion that the average thickness of the adsorbed layer is approximately  $1 R_G$  which correlates reasonably well with the literature reports<sup>66,70,259</sup>.

Rheological measurements also indicated that the solvation stabilization in acetone where a weak depletion attraction was detected smoothly shifts into the adsorption of polymer layers in ethyl acetate and acetone-toluene 1:1. An interpolation between the former two solvents reveals that the ideal Einstein's behavior would be reached at  $-\Delta H_{\text{add}}$  around  $-6.2 \text{ kcal}\cdot\text{mol}^{-1} \approx -25.9 \text{ kJ}\cdot\text{mol}^{-1}$ ,  $2.2 \text{ kcal}\cdot\text{mol}^{-1} \approx 9.2 \text{ kJ}\cdot\text{mol}^{-1}$  below the addition enthalpy of PMMA-silica ( $-4.0 \text{ kcal}\cdot\text{mol}^{-1} \approx -16.7 \text{ kJ}\cdot\text{mol}^{-1}$ ). For comparison, the difference of the silica cohesion energy ( $-11.6 \text{ kJ}\cdot\text{mol}^{-1}$ , see above) and the PMMA-silica addition enthalpy takes the value of  $5.1 \text{ kJ}\cdot\text{mol}^{-1}$ . Given the fact that the entropic penalty upon adsorption on a nanoparticle diminishes with increasing chain length of the adsorbate<sup>244,260</sup>, it is reasonable to expect that the full desorption of a polymer by a much smaller solvent molecule requires the latter to show an enthalpic gain superior to that of the polymer to outweigh the higher entropic penalty. Following this idea, one could attribute the value of  $9.2 \text{ kJ}\cdot\text{mol}^{-1}$  to the entropic gain as solvent is swapped with PMMA as the adsorbate on nanosilica. Despite the polymer chain itself experience an unfavorable adsorption entropy<sup>24,244,261</sup>, the overall entropic situation is beneficial to the polymer adsorption from solution. This conclusion correlates with the experimental findings of Hamieh<sup>262</sup> who reported the specific entropy of adsorption of PMMA-SiO<sub>2</sub> from various solvents to lie in the range  $0-62 \text{ J}\cdot\text{K}^{-1}\cdot\text{mol}^{-1} \approx 0-18.5 \text{ kJ}\cdot\text{mol}^{-1}$  @ 25 °C, among which toluene and THF take the value of 4 and 60  $\text{J}\cdot\text{K}^{-1}\cdot\text{mol}^{-1}$ , respectively. Remarkably, the currently estimated value of  $9.2 \text{ kJ}\cdot\text{mol}^{-1}$  is found near the middle of the range. However, the strong dependence of the adsorption entropy on solvent<sup>262</sup> prevents any further generalization of the results.

The influence of the nanoparticle loading on the spatial organization of the PNC was investigated in the range from 0.5 to 10 vol. % of NPs (Fig. 22, Fig. 26). The results show that the dispersion of isolated NPs in the samples prepared from acetone is only achieved at low

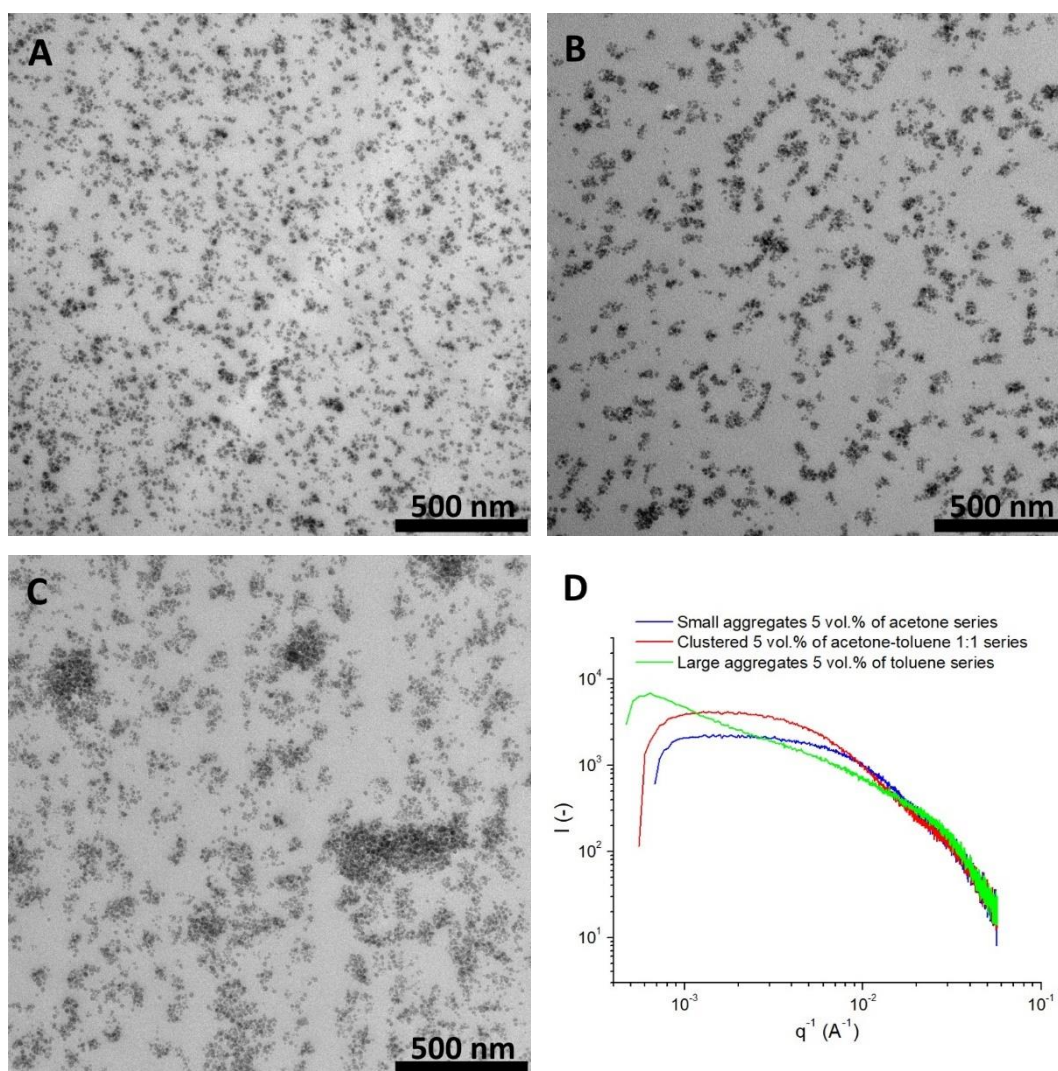


**Fig. 26:** TEM images of **(A)** isolated NPs and small aggregates in PNC samples prepared from acetone with NP loadings of 5 vol. %, **(B)** chain bound NP clusters prepared from acetone-toluene 1:1 mixture with NP loadings of 5 vol. %; and **(C)** aggregates prepared from toluene with NP loadings of 5 vol. %. **(D)** USAXS dependence of intensity  $I$  on the length of the scattering vector  $q$  extracted from USAXS data for PNC sample with NP loading 5 vol. %.

loadings (0.5 and 1 vol. %) while the concentrations above 2.5 vol. % cause the silica nanoparticles to aggregate. Similarly, the detected element size indicates that the stability of individual NPs was lost in ethyl acetate at 5 vol. % NP content. It might be a consequence of the shortened separation length between the NPs which promotes the short-range Van der Waals interaction which always oppose a good dispersion. The aggregate size was relatively small (about 26–34 nm) and grew gradually with increasing concentration as was determined by the image analysis of the TEM snapshots and fitting the USAXS data (Fig. 23A). Simultaneously, the depletion attraction in acetone samples smeared out as the small aggregates emerged and the viscosity further followed the ideal Einstein behavior (Fig. 24C). Likewise, the depletion attraction weakened with increasing NP concentration in THF though it was not completely erased, and neither was the aggregation. We hypothesize that the role

of the elementary structural unit is passed from the primary NPs onto the small ensembles and the situation becomes akin to a good dispersion of larger particles of the equivalent size. Clusters were observed in all samples of acetone-toluene series and the cluster size was preserved approximately constant at 43 nm throughout the whole investigated concentration range (Fig. 23A). Rheological data also indicates a consistent structure of acetone-toluene series within the investigated concentration range as the effective hydrodynamic parameter was preserved practically constant (Fig. 24C). Both populations of agglomerates present in samples of the toluene series grow with increasing silica content. The rapid agglomeration and the phase separation are more profound but principally unchanged at the higher NP concentration (Fig. 25B). Seemingly, the additional silica NPs are redistributed into both populations in a constant number ratio which cause the increase in the number of small agglomerates to appear more pronounced. However, a precise analysis of the TEM images was prevented by the strongly heterogeneous character of the samples caused by the phase separation while analysis of the USAXS data was constrained by the complex scattering pattern which did not converge to any standard fitting model.

In an attempt to compare the current experimental data with the PRISM theory by Schweizer<sup>24</sup>, the addition enthalpy  $-H_{\text{add}}$  (Fig. 24D) was converted into interaction strength (Fig. 27A). An adsorption of a dissolved polymer onto a NP requires that the active sites of both the polymer and the NP surface are freed of the solvent molecules that previously occupied them. Hence, the combined NP-solvent and solvent-polymer interaction opposes the polymer adsorption onto the NP surface while the freed solvent molecules reestablish a mutual interaction. Therefore, the interaction strength was calculated by subtracting the polymer-solvent enthalpy of mixing obtained from the Hansen's solubility parameters:

$$\Delta H_{\text{mix}} = RT\chi = \frac{V_m}{4}(\text{Ra})^2 \quad (24)$$

where  $\chi$ ,  $V_m$  and Ra denote the Flory-Huggins interaction parameter, molar volume and Hansen's distance parameter (eq. 15), respectively; and the solvent-silica addition enthalpy from the sum of the PMMA-silica addition enthalpy and solvent cohesion (evaporation) enthalpy  $\Delta H_{\text{evap}}$ . Unlike the PRISM theory deduced for polymer melts, the current experimental system is fairly diluted what mitigates the internal interactions<sup>51</sup> and reduces the number of entanglement per chain<sup>263</sup>; hence, the calculated value was multiplied by the polymer volume ratio ( $\varphi_p = 0.053$ ) to incorporate the dilution effect and receive the overall interaction strength:

$$\varepsilon = -\Delta H \cdot \varphi_p = -\varphi_p(\Delta H_{\text{add., p-NP}} + \Delta H_{\text{evap., s}} - \Delta H_{\text{add., s-NP}} - \Delta H_{\text{mix, p-s}}) \quad (25)$$

where the subscripts 'p' and 's' mark polymer and solvent, respectively. Remarkably, this rather complex computation combined with the experimental data for the non-aggregated samples collapses into a perfect line with the coefficient of determination  $R^2 = 0.9999$  (Fig. 27A). An interpolation of the acetone and ethyl acetate data showed that the ideal Einstein's behavior would be reached at  $-27.0 \text{ kJ}\cdot\text{mol}^{-1}$ .

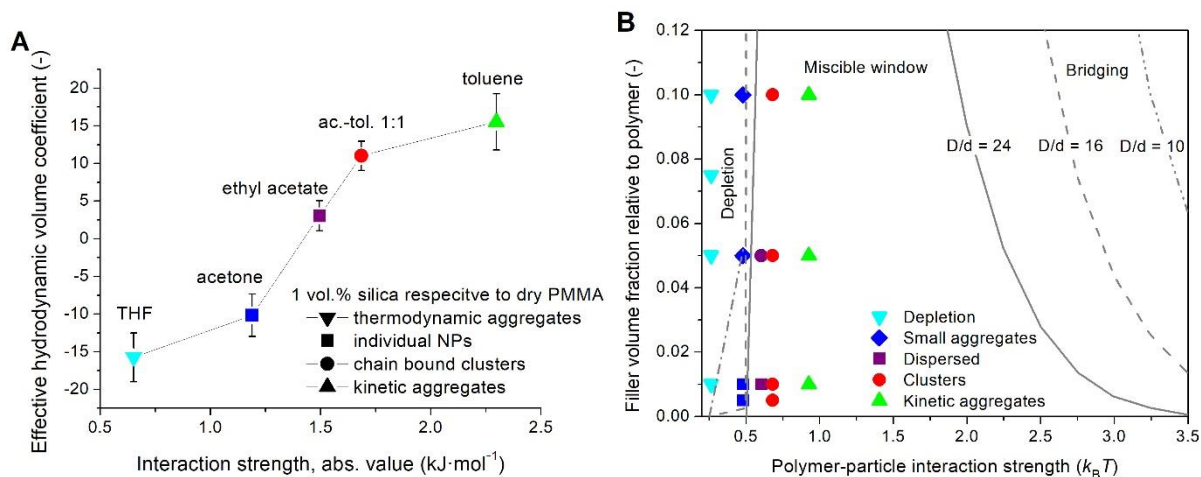


**Fig. 27: (A)** Variation of the effective hydrodynamic volume with the interaction strength  $\epsilon$  (Eq. 25) between solvent and silica at 1 vol. % NP content (respective to dry PMMA) in 5.3 vol. % PMMA solution in various solvents. **(B)** Phase diagram of PMMA-silica nanocomposites. Current experiments (points) are compared with the prediction of the PRISM theory (lines) presented in the ref. 24. Symbols indicate the solid-state NP dispersion while colors mark matching solvents in A and B.

The results, presented in the Table 4 along with the input parameters, were transformed into a phase diagram (Fig. 27B) predicted by the PRISM theory<sup>24</sup> for polymer chains of  $N = 100$  mers, decay length of the interaction  $\alpha = 0.5$  and variable NP-mer size ratio  $D/d$ . The number average molecular weight of the PMMA used in the experiments was  $50 \text{ kg}\cdot\text{mol}^{-1}$  which means that an average chain contains  $\sim 500$  methyl methacrylate units. Provided the length of a C–C bond being  $0.154 \text{ nm}$ , the  $D/d$  would take the value of  $\sim 65$ . If, however, a Kuhn's segment would be considered as the basic chain unit, an average chain would contain  $\sim 100$  units (Kuhn's length of PMMA equals  $l_k = 1.53 \text{ nm}$ <sup>264</sup>) and the  $D/d$  ratio would drop to  $\sim 13$ , both being values in the range investigated by the reported simulation. Keeping in mind the unclarity how well the simulation parameters match the current experimental system, a very good correlation was found between the model and the experimental structures at weak interaction strengths (depletion-driven phase separation). The chain-bound clusters lie deep in the miscible window though, but that could further shrink with an increasing  $D/d$  ratio or a decreasing decay length  $\alpha$ <sup>24</sup>. Speculatively, the entropically driven depletion aggregation treats the Kuhn's segment as the primary chain unit as it is a better representative of the chain dynamics while the enthalpically driven formation of polymer-bound clusters seems to conform better to monomer being the elementary chain unit, possibly due to the adsorption taking place on the scale of individual atoms and functional groups. However, one cannot omit the fact that the presence of solvent transforms the entropic contribution from unfavorable to favorable, as discussed above, which was not considered in the original PRISM theory.

Finally, the glass transition temperature ( $T_g$ ) was chosen as an exemplary bulk property of PNC to demonstrate the importance of NP spatial organization (Fig. 24D). Addition of NPs led to elevated  $T_g$  compared to pure PMMA in all cases regardless the NP structure. According to the expectations, the highest increase of  $T_g$  ( $\sim 6 \text{ }^\circ\text{C}$ ) was recorded for individually dispersed NPs

**Table 4:** Overview of addition enthalpy onto silica  $\Delta H_{add}$ , cohesion (evaporation) enthalpy  $\Delta H_{evap}$ , mixing enthalpy obtained from the HSP solubility parameters  $\Delta H_{mix}$ , undiluted interaction enthalpy of PMMA-silica  $\Delta H$ , and diluted interaction strength  $\epsilon = -\Delta H \cdot \phi_p$  for PMMA and various solvents.

	$\Delta H_{add}$ (kJ·mol <sup>-1</sup> )	$\Delta H_{evap}$ (kJ·mol <sup>-1</sup> )	$\Delta H_{mix}$ (kJ·mol <sup>-1</sup> )	$\Delta H$ (kJ·mol <sup>-1</sup> )	$\epsilon = -\Delta H \cdot \phi_p$ (kJ·mol <sup>-1</sup> )	$\epsilon = -\Delta H \cdot \phi_p$ (k <sub>B</sub> ·T)
THF	-37.1	-32.0	0.78	-12.38	0.65	0.26
acetone	-28.5	-33.7	0.56	-22.61	1.19	0.48
ethyl acetate	-25.6	-35.9	1.29	-28.42	1.49	0.60
acetone-toluene 1:1	-21.2	-35.6	0.67	-32.02	1.68	0.68
toluene	-13.8	-38.0	2.46	-43.67	2.30	0.93
PMMA	-16.7	-	-	-	-	-

(prepared from acetone or ethyl-acetate) which provided largest NP surface area available for polymer adsorption. The increase of  $T_g$  scaled only very weakly with NP volume fraction in these samples which means that the majority of polymer chains were already affected by addition of small portion of dispersed NPs. If the mean separation length of NP elements drops below approximately 4 times the polymer coil diameter, i.e., about 40 nm in this case, each chain is statistically either adjacent to a NP or neighboring with a such chain. Adsorption on NP surface alters the chain dynamics which in turn influences the dynamics of an intertangled neighbor. This possibly explains the nearly identical values of  $T_g$  for samples with individually dispersed NPs with the samples prepared from THF – though large aggregates were present; the remaining NPs were evenly dispersed through the matrix at mean interparticle distance comparable to the samples of acetone and ethyl acetate series (Fig. 23B) and probably contributed to most of the observed increase in  $T_g$ . Contrary, clusters of acetone-toluene 1:1 series showed systematically rising  $T_g$  with increasing NP volume fraction which manifested the constrained NP surface area available for polymer adsorption and extended mean separation length between clusters. The heterogeneous character of samples prepared from toluene, uneven distribution of NPs throughout the matrix due to phase separation and effective NP surface area lessened by aggregation reduced the impact of NPs on the polymer matrix and caused the samples of toluene series to exhibit the lowest  $T_g$  out of all the investigated PNCs.

### 6.3. Silica/PS nanocomposites

A set of silica/PS samples was prepared (Fig. 28) to elaborate on the general applicability of the results obtained with silica/PMMA nanocomposites. The silica NPs predispersed in ethyl methyl ketone remained individually dispersed when added to THF, *N,N*-dimethylacetamide (DMAc) and cyclohexanone. 1 vol.% of silica NPs maintained a clustered spatial organization in DMAc ( $d_{mean} = 33.8$  nm) and cyclohexanone ( $d_{mean} = 36.5$  nm) while depletion aggregation occurred in THF ( $d_{mean} = 1804.6$  nm), but, unlike in PMMA nanocomposites, no evidence of

individual NPs alongside the large aggregates was found in the samples prepared from THF (Fig. 28 III). A rather vague correlation of the interelement distance of the 5 nearest neighbors to the element diameter ratio was found between the experimental structures and a random dispersion (Fig. 29A); however, the steep slope at the low NP loading limit renders the function very sensitive to the precise particle content and, thus, prone to be dominated by the local NP concentration fluctuation.

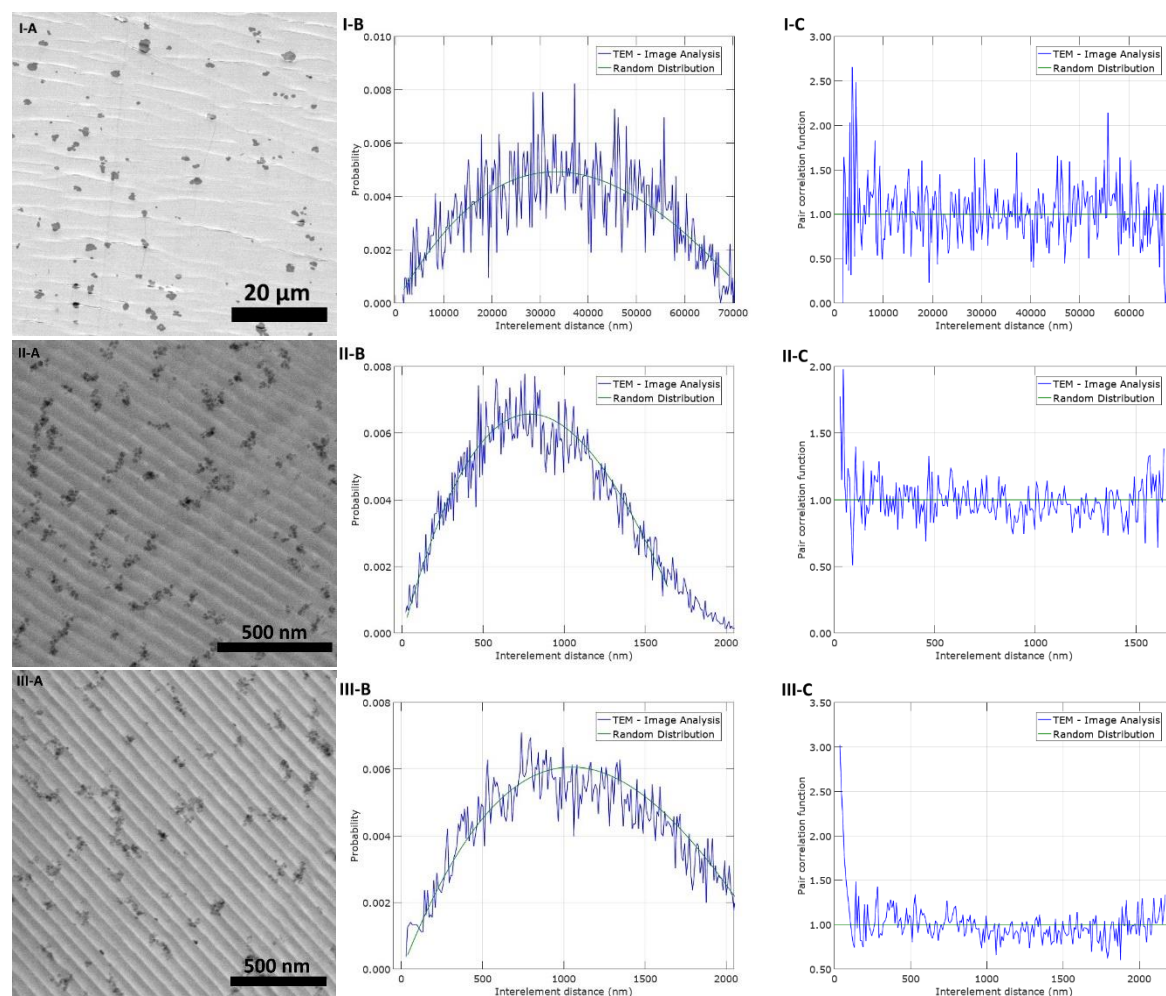


**Fig. 28:** Structural analysis of silica in PS 192k, **(A)** STEM image, **(B)** Probability distribution of interelement distances in the STEM image, **(C)** Pair correlation function; **(I)** THF/1 vol. % silica, **(II)** DMAc/1 vol. % silica, **(III)** cyclohexanone/1 vol. % silica.

The addition enthalpies onto silica were calculated according to the Drago's concept from the eq. 23 (Fig. 29B, Table 5). The missing values for cyclohexanone were substituted by acetone as the chemically closest substance with available data and the value for PS was approximated from styrene (substituted by toluene) multiplied by the polymer/monomer ratio for PMMA/MMA (substituted by methyl acetate) considering that the effectivity of the polymer interactions relative to its monomer is similar for PS and PMMA and stems from the steric inaccessibility of the functional groups attached to the polymer backbone. The depletion aggregation and clustering caused analogical discrepancy between the recorded viscosity (Fig.

29C) and the theoretical prediction of the Einstein's model (Fig. 29D) as their PMMA counterparts. At the first glance, the dissimilarity of the experimental structures, clearly proved by both the electron microscopy (Fig. 28) and the rheological data (Fig. 29C–D), might look confusing given the close values of the addition enthalpies on silica for THF ( $-8.9 \text{ kcal}\cdot\text{mol}^{-1} \cong -37.1 \text{ kJ}\cdot\text{mol}^{-1}$ ) and DMAc ( $-8.5 \text{ kcal}\cdot\text{mol}^{-1} \cong -35.7 \text{ kJ}\cdot\text{mol}^{-1}$ ); however, the interaction strength calculated according to the eq. 25 revealed the unlike character of the PS-silica interaction in these two solvents (Table 6) and both the depletion aggregation and clustering occurred in similar range as in the PMMA samples (Fig. 29E). It is worth noting that the silica/PMMA in ethyl acetate, system with the closest interaction strength to the clustered silica/PS in DMAc and cyclohexanone, showed a dispersion of individual NPs at 1 vol. % with a distorted distribution, possibly due to attractive interparticle interaction (Fig. 22 V), and a possible clustering at 5 vol. % (Fig. 22 VI). The phase diagram in the Fig. 29F suggests that the PS further narrows the miscible window, which would be expected for a longer polymer chain with a shorter Kuhn's length (1.0 nm for PS<sup>265</sup> compared to 1.53 nm for PMMA) defined by  $N \approx 280$ , and  $D/d \approx 20$ .

**Table 5:** Overview of the  $E$  and  $C$  values according to the Drago's concept for silica and various bases<sup>257,258</sup> and calculated addition enthalpies  $-\Delta H_{add}$  onto silica for the listed bases. \*Values for PS estimated from the data for toluene and PMMA/methyl acetate ratio. \*\*Missing values substituted by acetone as the chemically closest substance with available data.

Acid	$C_a$	$E_a$	
silica	1.08	4.36	
Bases	$C_b$	$E_b$	$\Delta H_{add}$ on silica ( $\text{kcal}\cdot\text{mol}^{-1}$ )
PS*	0.74	0.34	-2.3
THF	4.27	0.978	-8.9
DMAc ( <i>N,N</i> -dimethylacetamide)	2.58	1.32	-8.5
cyclohexanone**	2.33	0.987	-6.8

**Table 6:** Overview of addition enthalpy onto silica  $\Delta H_{add}$ , cohesion (evaporation) enthalpy  $\Delta H_{evap}$ , mixing enthalpy obtained from the HSP solubility parameters  $\Delta H_{mix}$ , undiluted interaction enthalpy of PS-silica  $\Delta H$ , and diluted interaction strength  $\epsilon = -\Delta H \cdot \phi_p$  for PS and various solvents.

	$\Delta H_{add}$ ( $\text{kJ}\cdot\text{mol}^{-1}$ )	$\Delta H_{evap}$ ( $\text{kJ}\cdot\text{mol}^{-1}$ )	$\Delta H_{mix}$ ( $\text{kJ}\cdot\text{mol}^{-1}$ )	$\Delta H$ ( $\text{kJ}\cdot\text{mol}^{-1}$ )	$\epsilon = -\Delta H \cdot \phi_p$ ( $\text{kJ}\cdot\text{mol}^{-1}$ )	$\epsilon = -\Delta H \cdot \phi_p$ ( $k_B \cdot T$ )
THF	-37.1	-32.0	1.94	-6.36	0.33	0.14
DMAc	-35.7	-48.2	3.45	-25.50	1.34	0.54
cyclohexanone	-28.4	-43.1	1.47	-25.66	1.35	0.54
PS	-9.5	-	-	-	-	-

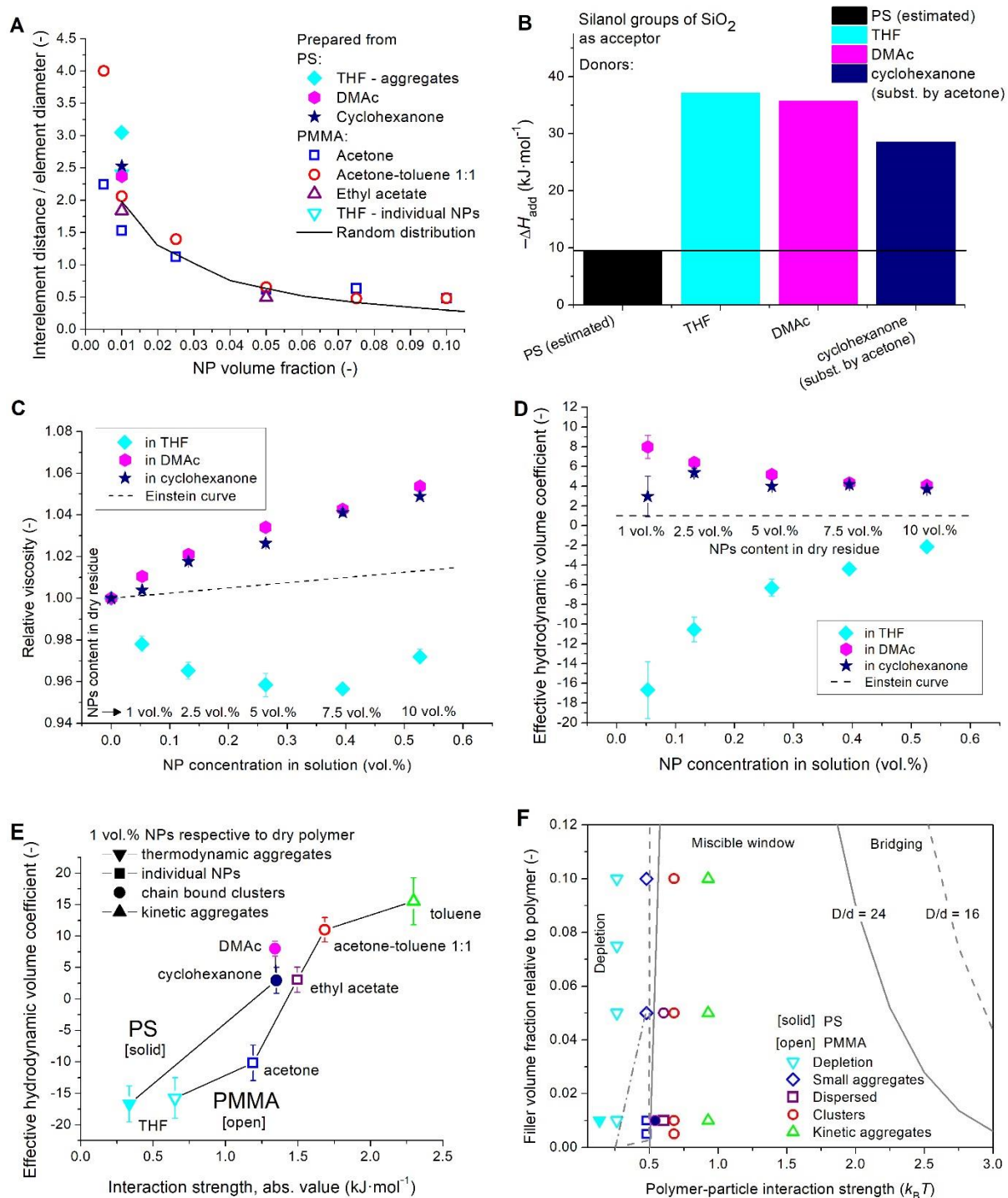


**Fig. 29: (A)** Dependence of interelement distance of 5 nearest neighbors divided by element diameter on NP volume fraction in solid state PS-based PNCs prepared from THF, DMAC, and cyclohexanone compared to PMMA PNCs. **(B)** Bar diagram of the donor-acceptor addition enthalpies  $-\Delta H_{add}$  of silanol groups of SiO<sub>2</sub> nanoparticles with PS and various solvents. The dependence of **(C)** the relative viscosity and **(D)** the effective hydrodynamic volume coefficient on the nanoparticle concentration in 5.3 vol. % solution of PS in various solvents with a clearly distinguishable behavior regarding the NP spatial organization. **(E)** Comparison of the effective hydrodynamic volume variation with the interaction

strength  $\epsilon$  (Eq. 25) between solvent and silica at 1 vol. % NP content (respective to dry polymer) for PMMA and PS 5.3 vol. % solution in various solvents. Symbols indicate the solid-state NP dispersion while colors match the solvents in A–D. **(F)** Phase diagram of PMMA-silica (open symbols) and PS-silica (solid symbols) nanocomposites. Current experiments (points) are compared with the prediction of the PRISM theory (lines) presented in the ref. 24. Symbols indicate the solid-state NP dispersion while colors mark matching solvents in A–E.

## 7. Conclusions

Nonlinear oscillatory shear test of POSS/PS nanocomposite solutions in toluene revealed dominant viscous contribution and presence of three regimes of viscoelastic response with varying shear strain amplitude within the investigated range. The pure PS solution exhibited the type III (*weak overshoot*) LAOS behavior, which is a common phenomenon for soft glassy materials under nonlinear oscillatory shear test, but it was shifted to the type IV (*strong overshoot*) LAOS behavior by the addition of strongly interacting OP-POSS NPs. The overshoot is caused by the balance of formation and destruction processes and the transition from the weak (type III) to the strong (type IV) type of overshoot was linked to enhanced structure formation rate due to the introduction of new attractive interactions (NP-polymer). It was suggested that NPs and chains form stiffened clusters at middle shear strain amplitudes. However, the role is strongly concentration confined, probably due to the NP propensity to aggregate at higher loadings, and only limited amount of OP-POSS NPs can be involved in the cluster formation.

NP structuring phenomena in polymer matrix was studied on silica/PMMA model system and the general applicability of the conclusions was tested on silica/PS samples. The adopted solution blending method was recognized as a suitable technique of polymer nanocomposite (PNC) preparation capable of simple nanoparticle (NP) dispersion tuning by the selection of solvent. A promising potential for further applications was promoted by preserving the NP spatial organization through the excessive thermal processing. Qualitative differences between various NP spatial organizations (individually dispersed NPs, polymer bound clusters and aggregates) were investigated with emphasis on the impact of NP dispersion on PNC properties which were demonstrated by direct comparison of glass transition temperatures for various NP arrangements. Deeper investigation into the structural impact on relaxation and mechanical properties may represent a goal for the further research. Combined results of TEM image analysis, USAXS and rheology provided a complex image of physico-chemical principles controlling the structuring phenomena of nanoparticles in polymer solutions and brought a comprehensive understanding of the composition-preparation protocol-solid state structure relationship.

Experimental evidence suggesting that the NP dispersion state is inherited from the solution-blending step of the PNC preparation and stems from the complex interplay of solvent-solvent, solvent-polymer, solvent-particle, polymer-particle, and particle-particle attractions was provided. The processing solvent was quantitatively linked to the amount of polymer adsorption and depletion attraction through a systematic increase of the effective hydrodynamic volume coefficient  $k$  with the increasing polymer-silica interaction strength which in turn depended strongly on the solvent's physico-chemical properties. A major contribution was attributed to the basic properties of the solvent molecule competing with the basic functional groups of polymer segments for the acidic active sites on the silica surface. The data reflects a shift from a favorable polymer adsorption at large positive  $k$  in weakly interacting solvents such as toluene or acetone-toluene 1:1 for PMMA and DMAc or cyclohexanone for PS mixture to a prevalent depletion attraction at large negative  $k$  in high-affine acetone or THF. An ideal Einstein behavior of the silica/PMMA nanocomposite solution

was predicted by interpolation between acetone and ethyl acetate to occur in a solvent in which the PMMA would experience an interaction strength to silica of  $-27.0 \text{ kJ}\cdot\text{mol}^{-1}$ . The experimental results correlated rather well with the prediction of the PRISM theory when dilution of the interaction strength was considered, since the theory was originally developed for adsorbing nanocomposite melts. A very narrow miscibility window was observed though, and it even closed at higher particle concentration. These results could potentially serve as the basis for prediction of the outcoming NP dispersion in adsorbing solution blended PNCs which could find an application in the design of advanced polymer nanocomposites with enhanced functional properties.

## 8. References

- (1) Zhou, Y.; He, J.; Hu, J.; Dang, B. Surface-Modified MgO Nanoparticle Enhances the Mechanical and Direct-Current Electrical Characteristics of Polypropylene/Polyolefin Elastomer Nanodielectrics. *J. Appl. Polym. Sci.* **2016**, *133* (1), 42863 1--10.
- (2) Javidparvar, A. A.; Ramezanzadeh, B.; Ghasemi, E. Effects of Surface Morphology and Treatment of Iron Oxide Nanoparticles on the Mechanical Properties of an Epoxy Coating. *Prog. Org. Coatings* **2016**, *90*, 10–20.
- (3) Su, N. C.; Buss, H. G.; McCloskey, B. D.; Urban, J. J. Enhancing Separation and Mechanical Performance of Hybrid Membranes through Nanoparticle Surface Modification. *ACS Macro Lett.* **2015**, *4* (11), 1239–1243.
- (4) Liff, S. M.; Kumar, N.; McKinley, G. H. High-Performance Elastomeric Nanocomposites via Solvent-Exchange Processing. *Nat. Mater.* **2007**, *6* (1), 76–83.
- (5) Chen, L.; Zhao, P.; Xie, H.; Yu, W. Thermal Properties of Epoxy Resin Based Thermal Interfacial Materials by Filling Ag Nanoparticle-Decorated Graphene Nanosheets. *Compos. Sci. Technol.* **2016**, *125*, 17–21.
- (6) Khosravi, S.; Rostami, A.; Rostami, G.; Dolatyari, M. Nanocomposite Multilayer Structure for Broadband MIR Negative Refractive Index. *J. Light. Technol.* **2015**, *33* (19), 4171–4175.
- (7) Bronnbauer, C.; Hornich, J.; Gasparini, N.; Guo, F.; Hartmeier, B.; Luechinger, N. A.; Pflaum, C.; Brabec, C. J.; Forberich, K. Printable Dielectric Mirrors with Easily Adjustable and Well-Defined Reflection Maxima for Semitransparent Organic Solar Cells. *Adv. Opt. Mater.* **2015**, *3* (10), 1424–1430.
- (8) Chen, S.; Gaume, R. Transparent Bulk-Size Nanocomposites with High Inorganic Loading. *Appl. Phys. Lett.* **2015**, *107* (24), 241906.
- (9) Gál, T.; Sepsi, Ö.; Medwick, P. A.; Wagner, A.; Koppa, P. Modeling the Optical Properties of Nanocomposite Media Using Effective Transfer Matrices. *Appl. Opt.* **2014**, *53* (28), 6598–6604.
- (10) Gadomsky, O. N.; Altunin, K. K.; Stepin, S. N.; Katnov, V. E.; Rusin, A. A.; Pereskokov, E. A. Near-Field Effect in Composite Nanomaterials with a Quasi-Zero Refractive Index. *Opt. Commun.* **2014**, *315*, 286–294.
- (11) Tang, F.; Wang, C.; Wang, J.; Wang, X.; Li, L. Organic–inorganic Hybrid Nanoparticles with Enhanced Fluorescence. *Colloids Surfaces A Physicochem. Eng. Asp.* **2015**, *480*, 38–44.
- (12) Li, X.; Niitsoo, O.; Couzis, A. Electrostatically Assisted Fabrication of Silver-Dielectric Core/Shell Nanoparticles Thin Film Capacitor with Uniform Metal Nanoparticle Distribution and Controlled Spacing. *J. Colloid Interface Sci.* **2016**, *465*, 333–341.

- (13) Park, C.; Wilkinson, J.; Banda, S.; Ounaies, Z.; Wise, K. E.; Sauti, G.; Lillehei, P. T.; Harrison, J. S. Aligned Single-Wall Carbon Nanotube Polymer Composites Using an Electric Field. *J. Polym. Sci. Part B Polym. Phys.* **2006**, *44* (12), 1751–1762.
- (14) Wu, S.; Ladani, R. B.; Zhang, J.; Bafekrpour, E.; Ghorbani, K.; Mouritz, A. P.; Kinloch, A. J.; Wang, C. H. Aligning Multilayer Graphene Flakes with an External Electric Field to Improve Multifunctional Properties of Epoxy Nanocomposites. *Carbon N. Y.* **2015**, *94*, 607–618.
- (15) Althumayri, K.; Harrison, W. J.; Shin, Y.; Gardiner, J. M.; Casiraghi, C.; Budd, P. M.; Bernardo, P.; Clarizia, G.; Jansen, J. C. The Influence of Few-Layer Graphene on the Gas Permeability of the High-Free-Volume Polymer PIM-1. *Philos. Trans. A. Math. Phys. Eng. Sci.* **2016**, *374* (2060).
- (16) Gupta, D.; Madhukar, A.; Choudhary, V. Effect of Functionality of Polyhedral Oligomeric Silsesquioxane [POSS] on the Properties of Sulfonated Poly(Ether Ether Ketone) [SPEEK] Based Hybrid Nanocomposite Proton Exchange Membranes for Fuel Cell Applications. *Int. J. Hydrogen Energy* **2013**, *38* (29), 12817–12829.
- (17) Kanehashi, S.; Chen, G. Q.; Scholes, C. A.; Ozcelik, B.; Hua, C.; Ciddor, L.; Southon, P. D.; D’Alessandro, D. M.; Kentish, S. E. Enhancing Gas Permeability in Mixed Matrix Membranes through Tuning the Nanoparticle Properties. *J. Memb. Sci.* **2015**, *482*, 49–55.
- (18) Gibson, L. J. The Hierarchical Structure and Mechanics of Plant Materials. *J. R. Soc. Interface* **2012**, *9* (76), 2749–2766.
- (19) Barthelat, F.; Engineering, M. Biomimetics for next Generation Materials. *Philos. Trans. R. Soc. London A Math. Phys. Eng. Sci.* **2007**, *365* (1861), 2907–2919.
- (20) Wegst, U. G. K.; Bai, H.; Saiz, E.; Tomsia, A. P.; Ritchie, R. O. Bioinspired Structural Materials. *Nat. Mater.* **2014**, *14* (1), 23–36.
- (21) Espinosa, H. D.; Rim, J. E.; Barthelat, F.; Buehler, M. J. Merger of Structure and Material in Nacre and Bone – Perspectives on de Novo Biomimetic Materials. *Prog. Mater. Sci.* **2009**, *54* (8), 1059–1100.
- (22) Rho, J.-Y.; Kuhn-Spearing, L.; Zioupos, P. Mechanical Properties and the Hierarchical Structure of Bone. *Med. Eng. & Phys.* **1998**, *20* (2), 92–102.
- (23) Wang, J.; Cheng, Q.; Tang, Z. Layered Nanocomposites Inspired by the Structure and Mechanical Properties of Nacre. *Chem. Soc. Rev.* **2012**, *41* (3), 1111–1129.
- (24) Hooper, J. B.; Schweizer, K. S. Theory of Phase Separation in Polymer Nanocomposites. *Macromolecules* **2006**, *39* (15), 5133–5142.
- (25) Nichols, G.; Byard, S.; Bloxham, M. J.; Botterill, J.; Dawson, N. J.; Dennis, A.; Diart, V.; North, N. C.; Sherwood, J. D. A Review of the Terms Agglomerate and Aggregate with a Recommendation for Nomenclature Used in Powder and Particle Characterization. *J.*

- Pharm. Sci.* **2002**, *91* (10), 2103–2109.
- (26) Sherman, L. M. Chasing Nanocomposites. *Plast. Technol.* **2004**, *50*, 56–61.
- (27) Starr, F. W.; Douglas, J. F.; Glotzer, S. C. Origin of Particle Clustering in a Simulated Polymer Nanocomposite and Its Impact on Rheology. *J. Chem. Phys.* **2003**, *119* (3), 1777.
- (28) Hiemenz, P. C.; Rajagopalan, R. *Principles of Colloid and Surface Chemistry, Third Edition, Revised and Expanded*; CRC Press, 1997.
- (29) Donaldson, S. H.; Røyne, A.; Kristiansen, K.; Rapp, M. V.; Das, S.; Gebbie, M. A.; Lee, D. W.; Stock, P.; Valtiner, M.; Israelachvili, J. Developing a General Interaction Potential for Hydrophobic and Hydrophilic Interactions. *Langmuir* **2015**, *31* (7), 2051–2064.
- (30) Zidek, J.; Kucera, J.; Jancar, J. Nearest Particle Distance and the Statistical Distribution of Agglomerates from a Model of a Finite Set of Particles. *C. Mater. Contin.* **2011**, *24* (3), 183–208.
- (31) Torquato, S.; Jiao, Y. Organizing Principles for Dense Packings of Nonspherical Hard Particles: Not All Shapes Are Created Equal. *Phys. Rev. E. Stat. Nonlin. Soft Matter Phys.* **2012**, *86* (1 Pt 1), 11102.
- (32) Jancar, J.; Douglas, J. F.; Starr, F. W.; Kumar, S. K.; Cassagnau, P.; Lesser, A. J.; Sternstein, S. S.; Buehler, M. J. Current Issues in Research on Structure–property Relationships in Polymer Nanocomposites. *Polymer (Guildf)*. **2010**, *51* (15), 3321–3343.
- (33) Hashemi, A.; Jouault, N.; Williams, G. A.; Zhao, D.; Cheng, K. J.; Kysar, J. W.; Guan, Z.; Kumar, S. K. Enhanced Glassy State Mechanical Properties of Polymer Nanocomposites via Supramolecular Interactions. *Nano Lett.* **2015**, *15* (8), 5465–5471.
- (34) Maillard, D.; Kumar, S. K.; Fragneaud, B.; Kysar, J. W.; Rungta, A.; Benicewicz, B. C.; Deng, H.; Brinson, L. C.; Douglas, J. F. Mechanical Properties of Thin Glassy Polymer Films Filled with Spherical Polymer-Grafted Nanoparticles. *Nano Lett.* **2012**, *12* (8), 3909–3914.
- (35) Jordan, J.; Jacob, K. I.; Tannenbaum, R.; Sharaf, M. A.; Jasiuk, I. Experimental Trends in Polymer Nanocomposites—a Review. *Mater. Sci. Eng. A* **2005**, *393* (1–2), 1–11.
- (36) Zhao, D.; Schneider, D.; Fytas, G.; Kumar, S. K. Controlling the Thermomechanical Behavior of Nanoparticle/Polymer Films. *ACS Nano* **2014**, *8* (8), 8163–8173.
- (37) Harton, S. E.; Kumar, S. K.; Yang, H.; Koga, T.; Hicks, K.; Lee, H.; Mijovic, J.; Liu, M.; Vallery, R. S.; Gidley, D. W. Immobilized Polymer Layers on Spherical Nanoparticles. *Macromolecules* **2010**, *43* (7), 3415–3421.
- (38) Schadler, L. S.; Kumar, S. K.; Benicewicz, B. C.; Lewis, S. L.; Harton, S. E. Designed Interfaces in Polymer Nanocomposites: A Fundamental Viewpoint. *MRS Bull.* **2007**, *32* (04), 335–340.
- (39) Kim, S. Y.; Schweizer, K. S.; Zukoski, C. F. Multiscale Structure, Interfacial Cohesion, Adsorbed Layers, and Thermodynamics in Dense Polymer-Nanoparticle Mixtures. *Phys.*

- Rev. Lett.* **2011**, *107* (22), 225504.
- (40) Meth, J. S.; Zane, S. G.; Chi, C.; Londono, J. D.; Wood, B. A.; Cotts, P.; Keating, M.; Guise, W.; Weigand, S. Development of Filler Structure in Colloidal Silica–Polymer Nanocomposites. *Macromolecules* **2011**, *44* (20), 8301–8313.
- (41) Janes, D. W.; Moll, J. F.; Harton, S. E.; Durning, C. J. Dispersion Morphology of Poly(Methyl Acrylate)/Silica Nanocomposites. *Macromolecules* **2011**, *44* (12), 4920–4927.
- (42) Bansal, A.; Yang, H.; Li, C.; Cho, K.; Benicewicz, B. C.; Kumar, S. K.; Schadler, L. S. Quantitative Equivalence between Polymer Nanocomposites and Thin Polymer Films. *Nat. Mater.* **2005**, *4* (9), 693–698.
- (43) Stojanović, D. B.; Brajović, L.; Orlović, A.; Dramlić, D.; Radmilović, V.; Uskoković, P. S.; Aleksić, R. Transparent PMMA/Silica Nanocomposites Containing Silica Nanoparticles Coating under Supercritical Conditions. *Prog. Org. Coatings* **2013**, *76* (4), 626–631.
- (44) Triebel, C.; Münstedt, H. Temperature Dependence of Rheological Properties of Poly(Methyl Methacrylate) Filled with Silica Nanoparticles. *Polymer (Guildf)*. **2011**, *52* (7), 1596–1602.
- (45) Mackay, M. E.; Tuteja, A.; Duxbury, P. M.; Hawker, C. J.; Van Horn, B.; Guan, Z.; Chen, G.; Krishnan, R. S. General Strategies for Nanoparticle Dispersion. *Science (80-. )*. **2006**, *311* (5768), 1740–1743.
- (46) Cangialosi, D.; Boucher, V. M.; Alegría, A.; Colmenero, J. Enhanced Physical Aging of Polymer Nanocomposites: The Key Role of the Area to Volume Ratio. *Polymer (Guildf)*. **2012**, *53* (6), 1362–1372.
- (47) Jouault, N.; Vallat, P.; Dalmas, F.; Said, S.; Jestin, J.; Boué, F. Well-Dispersed Fractal Aggregates as Filler in Polymer–Silica Nanocomposites: Long-Range Effects in Rheology. *Macromolecules* **2009**, *42* (6), 2031–2040.
- (48) Jouault, N.; Dalmas, F.; Boué, F.; Jestin, J. Multiscale Characterization of Filler Dispersion and Origins of Mechanical Reinforcement in Model Nanocomposites. *Polymer (Guildf)*. **2012**, *53* (3), 761–775.
- (49) Chevigny, C.; Jouault, N.; Dalmas, F.; Boué, F.; Jestin, J. Tuning the Mechanical Properties in Model Nanocomposites: Influence of the Polymer-Filler Interfacial Interactions. *J. Polym. Sci. Part B Polym. Phys.* **2011**, *49* (11), 781–791.
- (50) Jouault, N.; Zhao, D.; Kumar, S. K. Role of Casting Solvent on Nanoparticle Dispersion in Polymer Nanocomposites. *Macromolecules* **2014**, *47* (15), 5246–5255.
- (51) Kim, S. Y.; Zukoski, C. F. Role of Polymer Segment-Particle Surface Interactions in Controlling Nanoparticle Dispersions in Concentrated Polymer Solutions. *Langmuir* **2011**, *27* (17), 10455–10463.

- (52) Kim, S. Y.; Zukoski, C. F. Particle Restabilization in Silica/PEG/Ethanol Suspensions: How Strongly Do Polymers Need To Adsorb To Stabilize Against Aggregation? *Langmuir* **2011**, *27* (9), 5211–5221.
- (53) Kim, S. Y.; Zukoski, C. F. Super- and Sub-Einstein Intrinsic Viscosities of Spherical Nanoparticles in Concentrated Low Molecular Weight Polymer Solutions. *Soft Matter* **2012**, *8* (6), 1801–1810.
- (54) Kumar, S. K.; Krishnamoorti, R. Nanocomposites: Structure, Phase Behavior, and Properties. *Annu. Rev. Chem. Biomol. Eng.* **2010**, *1*, 37–58.
- (55) Patra, T. K.; Singh, J. K. Coarse-Grain Molecular Dynamics Simulations of Nanoparticle-Polymer Melt: Dispersion vs. Agglomeration. *J. Chem. Phys.* **2013**, *138* (14), 144901.
- (56) Akcora, P.; Liu, H.; Kumar, S. K.; Moll, J.; Li, Y.; Benicewicz, B. C.; Schadler, L. S.; Acehan, D.; Panagiotopoulos, A. Z.; Pryamitsyn, V.; et al. Anisotropic Self-Assembly of Spherical Polymer-Grafted Nanoparticles. *Nat. Mater.* **2009**, *8* (4), 354–359.
- (57) Housmans, C.; Sferrazza, M.; Napolitano, S. Kinetics of Irreversible Chain Adsorption. *Macromolecules* **2014**, *47* (10), 3390–3393.
- (58) Liu, J.; Wu, Y.; Shen, J.; Gao, Y.; Zhang, L.; Cao, D. Polymer–nanoparticle Interfacial Behavior Revisited: A Molecular Dynamics Study. *Phys. Chem. Chem. Phys.* **2011**, *13* (28), 13058.
- (59) Nakatani, A. .; Chen, W.; Schmidt, R. .; Gordon, G. .; Han, C. . Chain Dimensions in Polysilicate-Filled Poly(Dimethyl Siloxane). *Polymer (Guildf)*. **2001**, *42* (8), 3713–3722.
- (60) Tuteja, A.; Duxbury, P. M.; Mackay, M. E. Polymer Chain Swelling Induced by Dispersed Nanoparticles. *Phys. Rev. Lett.* **2008**, *100* (7), 077801.
- (61) Kim, S. Y.; Meyer, H. W.; Saalwächter, K.; Zukoski, C. F. Polymer Dynamics in PEG-Silica Nanocomposites: Effects of Polymer Molecular Weight, Temperature and Solvent Dilution. *Macromolecules* **2012**, *45* (10), 4225–4237.
- (62) Hooper, J. B.; Schweizer, K. S.; Desai, T. G.; Koshy, R.; Koblinski, P. Structure, Surface Excess and Effective Interactions in Polymer Nanocomposite Melts and Concentrated Solutions. *J. Chem. Phys.* **2004**, *121* (14), 6986.
- (63) Hooper, J. B.; Schweizer, K. S. Contact Aggregation, Bridging, and Steric Stabilization in Dense Polymer–Particle Mixtures. *Macromolecules* **2005**, *38* (21), 8858–8869.
- (64) Hooper, J. B.; Schweizer, K. S. Real Space Structure and Scattering Patterns of Model Polymer Nanocomposites. *Macromolecules* **2007**, *40* (19), 6998–7008.
- (65) Wang, D.; Yang, M.; Dong, Z.; Bo, S.; Ji, X. Interaction between Poly (Ethylene Oxide) and Silica Nanoparticles in Dilute Solutions. *Chinese J. Polym. Sci.* **2013**, *31* (9), 1290–1298.
- (66) Anderson, B. J.; Zukoski, C. F. Rheology and Microstructure of Entangled Polymer

- Nanocomposite Melts. *Macromolecules* **2009**, *42* (21), 8370–8384.
- (67) Jiang, T.; Zukoski, C. F. Role of Particle Size and Polymer Length in Rheology of Colloid–Polymer Composites. *Macromolecules* **2012**, *45* (24), 9791–9803.
- (68) Kim, S. Y.; Zukoski, C. F. Molecular Weight Effects on Particle and Polymer Microstructure in Concentrated Polymer Solutions. *Macromolecules* **2013**, *46* (16), 6634–6643.
- (69) Ranka, M.; Varkey, N.; Ramakrishnan, S.; Zukoski, C. F. Impact of Small Changes in Particle Surface Chemistry for Unentangled Polymer Nanocomposites. *Soft Matter* **2015**, *11* (8), 1634–1645.
- (70) Anderson, B. J.; Zukoski, C. F. Rheology and Microstructure of an Unentangled Polymer Nanocomposite Melt. *Macromolecules* **2008**, *41* (23), 9326–9334.
- (71) Anderson, B. J.; Zukoski, C. F. Rheology and Microstructure of Polymer Nanocomposite Melts: Variation of Polymer Segment-Surface Interaction. *Langmuir* **2010**, *26* (11), 8709–8720.
- (72) Rahedi, A. J.; Douglas, J. F.; Starr, F. W. Model for Reversible Nanoparticle Assembly in a Polymer Matrix. *J. Chem. Phys.* **2008**, *128* (2), 24902.
- (73) Zhang, Q.; Janner, M.; He, L.; Wang, M.; Hu, Y.; Lu, Y.; Yin, Y. Photonic Labyrinths: Two-Dimensional Dynamic Magnetic Assembly and *in Situ* Solidification. *Nano Lett.* **2013**, *13* (4), 1770–1775.
- (74) Ladani, R. B.; Wu, S.; Kinloch, A. J.; Ghorbani, K.; Zhang, J.; Mouritz, A. P.; Wang, C. H. Multifunctional Properties of Epoxy Nanocomposites Reinforced by Aligned Nanoscale Carbon. *Mater. Des.* **2016**, *94*, 554–564.
- (75) Khanna, P. K.; Singh, N.; Charan, S.; Subbarao, V. V. V. S.; Gokhale, R.; Mulik, U. P. Synthesis and Characterization of Ag/PVA Nanocomposite by Chemical Reduction Method. *Mater. Chem. Phys.* **2005**, *93* (1), 117–121.
- (76) Kuljanin-Jakovljević, J. Ž.; Radosavljević, A. N.; Spasojević, J. P.; Carević, M. V.; Mitrić, M. N.; Kačarević-Popović, Z. M. Gamma Irradiation Induced *In Situ* Synthesis of Lead Sulfide Nanoparticles in Poly(Vinyl Alcohol) Hydrogel. *Radiat. Phys. Chem.* **2017**, *130*, 282–290.
- (77) Lu, Y.; Mei, Y.; Schrunner, M.; Ballauff, M.; Möller, M. W.; Breu, J. *In Situ* Formation of Ag Nanoparticles in Spherical Polyacrylic Acid Brushes by UV Irradiation. *J. Phys. Chem. C* **2007**, *111* (21), 7676–7681.
- (78) Ji, X.; Hampsey, J. E.; Hu, Q.; He, J.; Yang, Z.; Lu, Y. Mesoporous Silica-Reinforced Polymer Nanocomposites. *Chem. Mater.* **2003**, *15* (19), 3656–3662.
- (79) Florea, N. M.; Lungu, A.; Badica, P.; Craciun, L.; Enculescu, M.; Ghita, D. G.; Ionescu, C.; Zgiran, R. G.; Iovu, H. Novel Nanocomposites Based on Epoxy Resin/Epoxy-Functionalized Polydimethylsiloxane Reinforced with POSS. *Compos. Part B Eng.* **2015**,

75, 226–234.

- (80) Bershtein, V.; Fainleib, A.; Egorova, L.; Grigoryeva, O.; Kirilenko, D.; Konnikov, S.; Ryzhov, V.; Starostenko, O.; Yakushev, P.; Yagovkina, M.; et al. The Impact of Ultra-Low Amounts of Introduced Reactive POSS Nanoparticles on Structure, Dynamics and Properties of Densely Cross-Linked Cyanate Ester Resins. *Eur. Polym. J.* **2015**, *67*, 128–142.
- (81) Wang, Q.; Wang, C.; Zhang, M.; Jian, M.; Zhang, Y. Feeding Single-Walled Carbon Nanotubes or Graphene to Silkworms for Reinforced Silk Fibers. *Nano Lett.* **2016**, *16* (10), 6695–6700.
- (82) Iftekhar Shams, M.; Nogi, M.; Berglund, L. A.; Yano, H. The Transparent Crab: Preparation and Nanostructural Implications for Bioinspired Optically Transparent Nanocomposites. *Soft Matter* **2012**, *8* (5), 1369–1373.
- (83) Li, Y.; Fu, Q.; Yu, S.; Yan, M.; Berglund, L. Optically Transparent Wood from a Nanoporous Cellulosic Template: Combining Functional and Structural Performance. *Biomacromolecules* **2016**, *17* (4), 1358–1364.
- (84) Fina, A.; Tabuani, D.; Camino, G. Polypropylene–polysilsesquioxane Blends. *Eur. Polym. J.* **2010**, *46* (1), 14–23.
- (85) Sánchez-Soto, M.; Schiraldi, D. A.; Illescas, S. Study of the Morphology and Properties of Melt-Mixed Polycarbonate–POSS Nanocomposites. *Eur. Polym. J.* **2009**, *45* (2), 341–352.
- (86) Iyer, S.; Schiraldi, D. A. Role of Specific Interactions and Solubility in the Reinforcement of Bisphenol A Polymers with Polyhedral Oligomeric Silsesquioxanes. *Macromolecules* **2007**, *40* (14), 4942–4952.
- (87) Joshi, M.; Butola, B. S.; Simon, G.; Kukaleva, N. Rheological and Viscoelastic Behavior of HDPE/Octamethyl-POSS Nanocomposites. *Macromolecules* **2006**, *39* (5), 1839–1849.
- (88) Cassagnau, P. Payne Effect and Shear Elasticity of Silica-Filled Polymers in Concentrated Solutions and in Molten State. *Polymer (Guildf)*. **2003**, *44* (8), 2455–2462.
- (89) Zheng, Y.; Yan, K.; Zhao, Y.; Zhu, X.; Möller, M.; Hu, C. Preparation and Characterization of Poly(L-Lactic Acid)/Hollow Silica Nanospheres Nanocomposites. *Fibers Polym.* **2016**, *17* (12), 2020–2026.
- (90) Alvarado, J.; Acosta, G.; Perez, F. Study of the Effect of the Dispersion of Functionalized Nanoparticles TiO<sub>2</sub> with Photocatalytic Activity in LDPE. *Polym. Degrad. Stab.* **2016**, *134*, 376–382.
- (91) Shenhar, R.; Norsten, T. B.; Rotello, V. M. Polymer-Mediated Nanoparticle Assembly: Structural Control and Applications. *Adv. Mater.* **2005**, *17* (6), 657–669.
- (92) Jouault, N.; Crawford, M. K.; Chi, C.; Smalley, R. J.; Wood, B.; Jestin, J.; Melnichenko, Y.

- B.; He, L.; Guise, W. E.; Kumar, S. K. Polymer Chain Behavior in Polymer Nanocomposites with Attractive Interactions. *ACS Macro Lett* **2016**, *5* (4), 523–527.
- (93) Van der Beek, G. P.; Stuart, M. A. C.; Fler, G. J.; Hofman, J. E. Segmental Adsorption Energies for Polymers on Silica and Alumina. *Macromolecules* **1991**, *24* (25), 6600–6611.
- (94) Hamming, L. M.; Qiao, R.; Messersmith, P. B.; Catherine Brinson, L. Effects of Dispersion and Interfacial Modification on the Macroscale Properties of TiO<sub>2</sub> Polymer–matrix Nanocomposites. *Compos. Sci. Technol.* **2009**, *69* (11–12), 1880–1886.
- (95) Bansal, A.; Yang, H.; Li, C.; Benicewicz, B. C.; Kumar, S. K.; Schadler, L. S. Controlling the Thermomechanical Properties of Polymer Nanocomposites by Tailoring the Polymer–particle Interface. *J. Polym. Sci. Part B Polym. Phys.* **2006**, *44* (20), 2944–2950.
- (96) Hedayati, M.; Salehi, M.; Bagheri, R.; Panjepour, M.; Maghzian, A. Ball Milling Preparation and Characterization of Poly (Ether Ether Ketone)/Surface Modified Silica Nanocomposite. *Powder Technol.* **2011**, *207* (1–3), 296–303.
- (97) Kalathi, J. T.; Yamamoto, U.; Schweizer, K. S.; Grest, G. S.; Kumar, S. K. Nanoparticle Diffusion in Polymer Nanocomposites. *Phys. Rev. Lett.* **2014**, *112* (10), 108301.
- (98) Noirez, L.; Baroni, P.; Mendil-Jakani, H. The Missing Parameter in Rheology: Hidden Solid-like Correlations in Viscous Liquids, Polymer Melts and Glass Formers. *Polym. Int.* **2009**, *58* (8), 962–968.
- (99) Graessley, W. W. Entangled Linear, Branched and Network Polymer Systems - Molecular Theories. *Adv. Polym. Sci.* **1982**, *47*, 67–117.
- (100) Hyun, K.; Kim, S. H.; Ahn, K. H.; Lee, S. J. Large Amplitude Oscillatory Shear as a Way to Classify the Complex Fluids. *J. Nonnewton. Fluid Mech.* **2002**, *107* (1–3), 51–65.
- (101) Hyun, K.; Wilhelm, M.; Klein, C. O.; Cho, K. S.; Nam, J. G.; Ahn, K. H.; Lee, S. J.; Ewoldt, R. H.; McKinley, G. H. A Review of Nonlinear Oscillatory Shear Tests: Analysis and Application of Large Amplitude Oscillatory Shear (LAOS). *Prog. Polym. Sci.* **2011**, *36* (12), 1697–1753.
- (102) Liu, J.; Gao, Y.; Cao, D.; Zhang, L.; Guo, Z. Nanoparticle Dispersion and Aggregation in Polymer Nanocomposites: Insights from Molecular Dynamics Simulation. *Langmuir* **2011**, *27* (12), 7926–7933.
- (103) Chen, Y.; Liu, L.; Yang, Q.; Wen, S.; Zhang, L.; Zhong, C. Computational Study of Nanoparticle Dispersion and Spatial Distribution in Polymer Matrix under Oscillatory Shear Flow. *Langmuir* **2013**, *29* (45), 13932–13942.
- (104) Mueller, S.; Llewellyn, E. W.; Mader, H. M. The Rheology of Suspensions of Solid Particles. *Proc. R. Soc. A Math. Phys. Eng. Sci.* **2009**, *466* (2116), 1201–1228.
- (105) Nguyen, N.-T. Micro-Magnetofluidics: Interactions between Magnetism and Fluid Flow on the Microscale. *Microfluid. Nanofluidics* **2012**, *12* (1–4), 1–16.

- (106) Erb, R. M.; Libanori, R.; Rothfuchs, N.; Studart, A. R. Composites Reinforced in Three Dimensions by Using Low Magnetic Fields. *Science* (80-. ). **2012**, *335* (6065), 199–204.
- (107) Libanori, R.; Erb, R. M.; Studart, A. R. Mechanics of Platelet-Reinforced Composites Assembled Using Mechanical and Magnetic Stimuli. *ACS Appl. Mater. Interfaces* **2013**, *5* (21), 10794–10805.
- (108) Le Ferrand, H.; Bolisetty, S.; Demirörs, A. F.; Libanori, R.; Studart, A. R.; Mezzenga, R. Magnetic Assembly of Transparent and Conducting Graphene-Based Functional Composites. *Nat. Commun.* **2016**, *7*, 12078.
- (109) He, L.; Wang, M.; Ge, J.; Yin, Y. Magnetic Assembly Route to Colloidal Responsive Photonic Nanostructures. *Acc. Chem. Res.* **2012**, *45* (9), 1431–1440.
- (110) He, L.; Hu, Y.; Kim, H.; Ge, J.; Kwon, S.; Yin, Y. Magnetic Assembly of Nonmagnetic Particles into Photonic Crystal Structures. *Nano Lett.* **2010**, *10* (11), 4708–4714.
- (111) Kushnir, S. E.; Kazin, P. E.; Trusov, L. A.; Tretyakov, Y. D. Self-Organization of Micro- and Nanoparticles in Ferrofluids. *Russ. Chem. Rev.* **2012**, *81* (6), 560–570.
- (112) Wang, M.; He, L.; Yin, Y. Magnetic Field Guided Colloidal Assembly. *Mater. Today* **2013**, *16* (4), 110–116.
- (113) Tracy, J. B.; Crawford, T. M. Magnetic Field-Directed Self-Assembly of Magnetic Nanoparticles. *MRS Bull.* **2013**, *38* (11), 915–920.
- (114) Ghosh, S.; Puri, I. K. Soft Polymer Magnetic Nanocomposites: Microstructure Patterning by Magnetophoretic Transport and Self-Assembly. *Soft Matter* **2013**, *9* (6), 2024–2029.
- (115) Tang, Y.; Chen, Q.; Chen, R. Magnetic Field Induced Controllable Self-Assembly of Maghemite Nanocrystals: From 3D Arrays to 1D Nanochains. *Appl. Surf. Sci.* **2015**, *347*, 202–207.
- (116) Motornov, M.; Malynych, S. Z.; Pippalla, D. S.; Zdyrko, B.; Royter, H.; Roiter, Y.; Kahabka, M.; Tokarev, A.; Tokarev, I.; Zhulina, E.; et al. Field-Directed Self-Assembly with Locking Nanoparticles. *Nano Lett.* **2012**, *12* (7), 3814–3820.
- (117) Fragouli, D.; Buonsanti, R.; Bertoni, G.; Sangregorio, C.; Innocenti, C.; Falqui, A.; Gatteschi, D.; Cozzoli, P. D.; Athanassiou, A.; Cingolani, R. Dynamical Formation of Spatially Localized Arrays of Aligned Nanowires in Plastic Films with Magnetic Anisotropy. *ACS Nano* **2010**, *4* (4), 1873–1878.
- (118) Lorenzo, D.; Fragouli, D.; Bertoni, G.; Innocenti, C.; Anyfantis, G. C.; Davide Cozzoli, P.; Cingolani, R.; Athanassiou, A. Formation and Magnetic Manipulation of Periodically Aligned Microchains in Thin Plastic Membranes. *J. Appl. Phys.* **2012**, *112* (8), 083927.
- (119) Melle, S.; Martin, J. E. Chain Model of a Magnetorheological Suspension in a Rotating Field. *J. Chem. Phys.* **2003**, *118* (21), 9875.
- (120) Melle, S.; Calderón, O. G.; Rubio, M. A.; Fuller, G. G. Chain Rotational Dynamics in MR

- Suspensions. *Int. J. Mod. Phys. B* **2002**, *16* (17n18), 2293–2299.
- (121) Rigbi, Z.; Mark, J. E. Effects of a Magnetic Field Applied during the Curing of a Polymer Loaded with Magnetic Filler. *J. Polym. Sci. Polym. Phys. Ed.* **1985**, *23* (6), 1267–1269.
- (122) Sohoni, G. B.; Mark, J. E. Anisotropic Reinforcement in Elastomers Containing Magnetic Filler Particles. *J. Appl. Polym. Sci.* **1987**, *34* (8), 2853–2859.
- (123) Jestin, J.; Cousin, F.; Dubois, I.; Ménager, C.; Schweins, R.; Oberdisse, J.; Boué, F. Anisotropic Reinforcement of Nanocomposites Tuned by Magnetic Orientation of the Filler Network. *Adv. Mater.* **2008**, *20* (13), 2533–2540.
- (124) Robbes, A.-S.; Cousin, F.; Meneau, F.; Dalmas, F.; Boué, F.; Jestin, J. Nanocomposite Materials with Controlled Anisotropic Reinforcement Triggered by Magnetic Self-Assembly. *Macromolecules* **2011**, *44* (22), 8858–8865.
- (125) Ge, J.; Lee, H.; He, L.; Kim, J.; Lu, Z.; Kim, H.; Goebel, J.; Kwon, S.; Yin, Y. Magnetochromatic Microspheres: Rotating Photonic Crystals. *J. Am. Chem. Soc.* **2009**, *131* (43), 15687–15694.
- (126) Fragouli, D.; Das, A.; Innocenti, C.; Guttikonda, Y.; Rahman, S.; Liu, L.; Caramia, V.; Megaridis, C. M.; Athanassiou, A. Polymeric Films with Electric and Magnetic Anisotropy Due to Magnetically Assembled Functional Nanofibers. *ACS Appl. Mater. Interfaces* **2014**, *6* (6), 4535–4541.
- (127) Krommenhoek, P. J.; Tracy, J. B. Magnetic Field-Directed Self-Assembly of Magnetic Nanoparticle Chains in Bulk Polymers. *Part. Part. Syst. Charact.* **2013**, *30* (9), 759–763.
- (128) Swan, J. W.; Bauer, J. L.; Liu, Y.; Furst, E. M. Directed Colloidal Self-Assembly in Toggled Magnetic Fields. *Soft Matter* **2014**, *10* (8), 1102–1109.
- (129) Panda, P.; Bong, K. W.; Hatton, T. A.; Doyle, P. S. Branched Networks by Directed Assembly of Shape Anisotropic Magnetic Particles. *Langmuir* **2011**, *27* (22), 13428–13435.
- (130) Domínguez-García, P.; Melle, S.; Pastor, J. M.; Rubio, M. A. Scaling in the Aggregation Dynamics of a Magnetorheological Fluid. *Phys. Rev. E* **2007**, *76* (5), 051403.
- (131) Melle, S.; Calderón, O. G.; Rubio, M. A.; Fuller, G. G. Rotational Dynamics in Dipolar Colloidal Suspensions: Video Microscopy Experiments and Simulations Results. *J. Nonnewton. Fluid Mech.* **2002**, *102* (2), 135–148.
- (132) Swan, J. W.; Vasquez, P. A.; Whitson, P. A.; Fincke, E. M.; Wakata, K.; Magnus, S. H.; Winne, F. D.; Barratt, M. R.; Agui, J. H.; Green, R. D.; et al. Multi-Scale Kinetics of a Field-Directed Colloidal Phase Transition. *Proc. Natl. Acad. Sci.* **2012**, *109* (40), 16023–16028.
- (133) Melle, S.; Fuller, G. G.; Rubio, M. A. Structure and Dynamics of Magnetorheological Fluids in Rotating Magnetic Fields. *Phys. Rev. E* **2000**, *61* (4), 4111–4117.
- (134) Melle, S.; Rubio, M. A.; Fuller, G. G. Time Scaling Regimes in Aggregation of Magnetic

- Dipolar Particles: Scattering Dichroism Results. *Phys. Rev. Lett.* **2001**, *87* (11), 115501.
- (135) Melle, S.; Rubio, M. A.; Fuller, G. G. Orientation Dynamics of Magnetorheological Fluids Subject to Rotating External Fields. *Int. J. Mod. Phys. B* **2001**, *15* (06n07), 758–766.
- (136) Melle, S.; Calderón, O. G.; Rubio, M. A.; Fuller, G. G. Microstructure Evolution in Magnetorheological Suspensions Governed by Mason Number. *Phys. Rev. E* **2003**, *68* (4), 041503.
- (137) Domínguez-García, P.; Pastor, J. M.; Melle, S.; Rubio, M. A. Electrostatic and Hydrodynamics Effects in a Sedimented Magnetorheological Suspension. *Phys. Rev. E* **2009**, *80* (2), 021405.
- (138) Park, B. J.; Fang, F. F.; Choi, H. J. Magnetorheology: Materials and Application. *Soft Matter* **2010**, *6* (21), 5246.
- (139) Hong, R. Y.; Ren, Z. Q.; Han, Y. P.; Li, H. Z.; Zheng, Y.; Ding, J. Rheological Properties of Water-Based Ferrofluids. *Chem. Eng. Sci.* **2007**, *62* (21), 5912–5924.
- (140) Zhou, W. L.; Carpenter, E. E.; Lin, J.; Kumbhar, A.; Sims, J.; O'Connor, C. J. Nanostructures of Gold Coated Iron Core-Shell Nanoparticles and the Nanobands Assembled under Magnetic Field. *Eur. Phys. J. D* **2001**, *16* (1), 289–292.
- (141) Ge, J.; Yin, Y. Magnetically Tunable Colloidal Photonic Structures in Alkanol Solutions. *Adv. Mater.* **2008**, *20* (18), 3485–3491.
- (142) Lin, J.; Zhou, W.; Kumbhar, A.; Wiemann, J.; Fang, J.; Carpenter, E. E.; O'Connor, C. J. Gold-Coated Iron (Fe@Au) Nanoparticles: Synthesis, Characterization, and Magnetic Field-Induced Self-Assembly. *J. Solid State Chem.* **2001**, *159* (1), 26–31.
- (143) Sahoo, Y.; Cheon, M.; Wang, S.; Luo, H.; Furlani, E. P.; Prasad, P. N. Field-Directed Self-Assembly of Magnetic Nanoparticles. *J. Phys. Chem. B* **2004**, *108* (11), 3380–3383.
- (144) Gao, J.; Zhang, B.; Zhang, X.; Xu, B. Magnetic-Dipolar-Interaction-Induced Self-Assembly Affords Wires of Hollow Nanocrystals of Cobalt Selenide. *Angew. Chemie Int. Ed.* **2006**, *45* (8), 1220–1223.
- (145) Jia, B.; Gao, L. Morphological Transformation of Fe<sub>3</sub>O<sub>4</sub> Spherical Aggregates from Solid to Hollow and Their Self-Assembly under an External Magnetic Field. *J. Phys. Chem. C* **2008**, *112* (3), 666–671.
- (146) Keng, P. Y.; Kim, B. Y.; Shim, I.-B.; Sahoo, R.; Veneman, P. E.; Armstrong, N. R.; Yoo, H.; Pemberton, J. E.; Bull, M. M.; Griebel, J. J.; et al. Colloidal Polymerization of Polymer-Coated Ferromagnetic Nanoparticles into Cobalt Oxide Nanowires. *ACS Nano* **2009**, *3* (10), 3143–3157.
- (147) Hill, L. J.; Pyun, J. Colloidal Polymers via Dipolar Assembly of Magnetic Nanoparticle Monomers. *ACS Appl. Mater. Interfaces* **2014**, *6* (9), 6022–6032.
- (148) He, L.; Wang, M.; Zhang, Q.; Lu, Y.; Yin, Y. Magnetic Assembly and Patterning of General

- Nanoscale Materials through Nonmagnetic Templates. *Nano Lett.* **2013**, *13* (1), 264–271.
- (149) Bell, R. C.; Karli, J. O.; Vavreck, A. N.; Zimmerman, D. T.; Ngatu, G. T.; Wereley, N. M. Magnetorheology of Submicron Diameter Iron Microwires Dispersed in Silicone Oil. *Smart Mater. Struct.* **2008**, *17* (1), 015028.
- (150) Ye, L.; Pearson, T.; Cordeau, Y.; Mefford, O. T.; Crawford, T. M. Triggered Self-Assembly of Magnetic Nanoparticles. *Sci. Rep.* **2016**, *6*, 23145.
- (151) Hu, Y.; He, L.; Yin, Y. Magnetically Responsive Photonic Nanochains. *Angew. Chemie Int. Ed.* **2011**, *50* (16), 3747–3750.
- (152) Laskar, J. M.; Philip, J.; Raj, B. Experimental Evidence for Reversible Zippering of Chains in Magnetic Nanofluids under External Magnetic Fields. *Phys. Rev. E* **2009**, *80* (4), 041401.
- (153) Ahniyaz, A.; Sakamoto, Y.; Bergstrom, L. Magnetic Field-Induced Assembly of Oriented Superlattices from Maghemite Nanocubes. *Proc. Natl. Acad. Sci.* **2007**, *104* (45), 17570–17574.
- (154) Ding, T.; Song, K.; Clays, K.; Tung, C.-H. Fabrication of 3D Photonic Crystals of Ellipsoids: Convective Self-Assembly in Magnetic Field. *Adv. Mater.* **2009**, *21* (19), 1936–1940.
- (155) Yin, Y.; Xia, Y. Self-Assembly of Monodispersed Spherical Colloids into Complex Aggregates with Well-Defined Sizes, Shapes, and Structures. *Adv. Mater.* **2001**, *13* (4), 267–271.
- (156) Chen, C.-J.; Chiang, R.-K.; Jeng, Y.-R. Crystallization and Magnetic Properties of 3D Micrometer-Scale Simple-Cubic Maghemite Superlattices. *J. Phys. Chem. C* **2011**, *115* (37), 18142–18148.
- (157) Hynninen, A.-P.; Dijkstra, M. Phase Diagram of Dipolar Hard and Soft Spheres: Manipulation of Colloidal Crystal Structures by an External Field. *Phys. Rev. Lett.* **2005**, *94* (13), 138303.
- (158) Yethiraj, A.; van Blaaderen, A. A Colloidal Model System with an Interaction Tunable from Hard Sphere to Soft and Dipolar. *Nature* **2003**, *421* (6922), 513–517.
- (159) Liu, Q.; Roberts, A. P.; Larrasoña, J. C.; Banerjee, S. K.; Guyodo, Y.; Tauxe, L.; Oldfield, F. Environmental Magnetism: Principles and Applications. *Rev. Geophys.* **2012**, *50* (4), RG4002.
- (160) Ge, K.; Liu, Q. Effects of the Grain Size Distribution on Magnetic Properties of Magnetite: Constraints from Micromagnetic Modeling. *Chinese Sci. Bull.* **2014**, *59* (34), 4763–4773.
- (161) Williams, W.; Dunlop, D. J. Simulation of Magnetic Hysteresis in Pseudo-Single-Domain Grains of Magnetite. *J. Geophys. Res. Solid Earth* **1995**, *100* (B3), 3859–3871.
- (162) Cheng, G.; Romero, D.; Fraser, G. T.; Hight Walker, A. R. Magnetic-Field-Induced

- Assemblies of Cobalt Nanoparticles. *Langmuir* **2005**, *21* (26), 12055–12059.
- (163) Erb, R. M.; Yellen, B. B. Magnetic Manipulation of Colloidal Particles. In *Nanoscale Magnetic Materials and Applications*; Springer US: Boston, MA, 2009; pp 563–590.
- (164) He, L.; Hu, Y.; Han, X.; Lu, Y.; Lu, Z.; Yin, Y. Assembly and Photonic Properties of Superparamagnetic Colloids in Complex Magnetic Fields. *Langmuir* **2011**, *27* (22), 13444–13450.
- (165) Roskov, K. E.; Atkinson, J. E.; Bronstein, L. M.; Spontak, R. J. Magnetic Field-Induced Alignment of Nanoparticles in Electrospun Microfibers. *RSC Adv.* **2012**, *2* (11), 4603.
- (166) Grzelczak, M.; Vermant, J.; Furst, E. M.; Liz-Marzán, L. M. Directed Self-Assembly of Nanoparticles. *ACS Nano* **2010**, *4* (7), 3591–3605.
- (167) Min, Y.; Akbulut, M.; Kristiansen, K.; Golan, Y.; Israelachvili, J. The Role of Interparticle and External Forces in Nanoparticle Assembly. *Nat. Mater.* **2008**, *7* (7), 527–538.
- (168) Lumsdon, S. O.; Kaler, E. W.; Velev, O. D. Two-Dimensional Crystallization of Microspheres by a Coplanar AC Electric Field. *Langmuir* **2004**, *20* (6), 2108–2116.
- (169) Goh, P. S.; Ismail, A. F.; Ng, B. C. Directional Alignment of Carbon Nanotubes in Polymer Matrices: Contemporary Approaches and Future Advances. *Compos. Part A Appl. Sci. Manuf.* **2014**, *56*, 103–126.
- (170) Cho, H.-B.; Nakayama, T.; Suematsu, H.; Suzuki, T.; Jiang, W.; Niihara, K.; Song, E.; Eom, N. S. A.; Kim, S.; Choa, Y.-H. Insulating Polymer Nanocomposites with High-Thermal-Conduction Routes via Linear Densely Packed Boron Nitride Nanosheets. *Compos. Sci. Technol.* **2016**, *129*, 205–213.
- (171) Batra, S.; Unsal, E.; Cakmak, M. Directed Electric Field Z -Alignment Kinetics of Anisotropic Nanoparticles for Enhanced Ionic Conductivity. *Adv. Funct. Mater.* **2014**, *24* (48), 7698–7708.
- (172) Oliva-Avilés, A. I.; Avilés, F.; Sosa, V. Electrical and Piezoresistive Properties of Multi-Walled Carbon Nanotube/Polymer Composite Films Aligned by an Electric Field. *Carbon N. Y.* **2011**, *49* (9), 2989–2997.
- (173) Koerner, H.; Jacobs, J. D.; Tomlin, D. W.; Busbee, J. D.; Vaia, R. A. Tuning Polymer Nanocomposite Morphology: AC Electric Field Manipulation of Epoxy–Montmorillonite (Clay) Suspensions. *Adv. Mater.* **2004**, *16* (4), 297–302.
- (174) Martin, C. A.; Sandler, J. K. W.; Windle, A. H.; Schwarz, M.-K.; Bauhofer, W.; Schulte, K.; Shaffer, M. S. P. Electric Field-Induced Aligned Multi-Wall Carbon Nanotube Networks in Epoxy Composites. *Polymer (Guildf).* **2005**, *46* (3), 877–886.
- (175) Fujihara, T.; Cho, H.-B.; Kanno, M.; Nakayama, T.; Suzuki, T.; Jiang, W.; Suematsu, H.; Niihara, K. Three-Dimensional Structural Control and Analysis of Hexagonal Boron Nitride Nanosheets Assembly in Nanocomposite Films Induced by Electric Field

- Concentration. *Jpn. J. Appl. Phys.* **2014**, 53 (2S), 02BD12.
- (176) Huynh, M. T. T.; Nakayama, T.; Kawamoto, A.; Nguyen, S. T.; Suzuki, T.; Suematsu, H.; Niihara, K.; Cho, H.-B.; Choa, Y.-H. Fabrication of Stacked-Cup Carbon Nanotube/Polymer Nanocomposite Films with Linear Controlled Percolation Routes. *Mater. Chem. Phys.* **2016**, 171, 39–44.
- (177) Payne, A. R.; Whittaker, R. E. Reinforcement of Rubber with Carbon Black. *Composites* **1970**, 1 (4), 203–214.
- (178) Payne, A. R. Dynamic Properties of Natural Rubber Containing Heat-Treated Carbon Blacks. *J. Appl. Polym. Sci.* **1965**, 9 (10), 3245–3254.
- (179) Hassanabadi, H. M.; Wilhelm, M.; Rodrigue, D. A Rheological Criterion to Determine the Percolation Threshold in Polymer Nano-Composites. *Rheol. Acta* **2014**, 53 (10–11), 869–882.
- (180) Sugiyama, M.; Nakamura, Y.; Norisuye, T. Dilute-Solution Properties of Polystyrene Polymacromonomer Having Side Chains of over 100 Monomeric Units. *Polym. J.* **2007**, 40 (2), 109–115.
- (181) Lim, H. T.; Ahn, K. H.; Hong, J. S.; Hyun, K. Nonlinear Viscoelasticity of Polymer Nanocomposites under Large Amplitude Oscillatory Shear Flow. *J. Rheol. (N. Y. N. Y.)* **2013**, 57 (3), 767.
- (182) Salehiyan, R.; Song, H. Y.; Choi, W. J.; Hyun, K. Characterization of Effects of Silica Nanoparticles on (80/20) PP/PS Blends via Nonlinear Rheological Properties from Fourier Transform Rheology. *Macromolecules* **2015**, 48 (13), 4669–4679.
- (183) BELLAN, C.; BOSSIS, G. FIELD DEPENDENCE OF VISCOELASTIC PROPERTIES OF MR ELASTOMERS. *Int. J. Mod. Phys. B* **2002**, 16 (17n18), 2447–2453.
- (184) Jancar, J.; Recman, L. Particle Size Dependence of the Elastic Modulus of Particulate Filled PMMA near Its Tg. *Polymer (Guildf)*. **2010**, 51 (17), 3826–3828.
- (185) Kalfus, J.; Jancar, J. Reinforcing Mechanisms in Amorphous Polymer Nano-Composites. *Compos. Sci. Technol.* **2008**, 68 (15–16), 3444–3447.
- (186) Kopesky, E. T.; Haddad, T. S.; McKinley, G. H.; Cohen, R. E. Miscibility and Viscoelastic Properties of Acrylic Polyhedral Oligomeric Silsesquioxane–poly(Methyl Methacrylate) Blends. *Polymer (Guildf)*. **2005**, 46 (13), 4743–4752.
- (187) Kalfus, J.; Jancar, J. Viscoelastic Response of Nanocomposite Poly(Vinyl Acetate)-Hydroxyapatite with Varying Particle Shape—Dynamic Strain Softening and Modulus Recovery. *Polym. Compos.* **2007**, 28 (6), 743–747.
- (188) Jancar, J.; Hoy, R. S.; Lesser, A. J.; Jancarova, E.; Zidek, J. Effect of Particle Size, Temperature, and Deformation Rate on the Plastic Flow and Strain Hardening Response of PMMA Composites. *Macromolecules* **2013**, 46 (23), 9409–9426.

- (189) Sarvestani, A. S.; Picu, C. R. Network Model for the Viscoelastic Behavior of Polymer Nanocomposites. *Polymer (Guildf)*. **2004**, *45* (22), 7779–7790.
- (190) Sarvestani, A. S.; Picu, C. R. A Frictional Molecular Model for the Viscoelasticity of Entangled Polymer Nanocomposites. *Rheol. Acta* **2005**, *45* (2), 132–141.
- (191) Chen, Q.; Gong, S.; Moll, J.; Zhao, D.; Kumar, S. K.; Colby, R. H. Mechanical Reinforcement of Polymer Nanocomposites from Percolation of a Nanoparticle Network. *ACS Macro Lett.* **2015**, *4* (4), 398–402.
- (192) Zhu, A.-J.; Sternstein, S. . Nonlinear Viscoelasticity of Nanofilled Polymers: Interfaces, Chain Statistics and Properties Recovery Kinetics. *Compos. Sci. Technol.* **2003**, *63* (8), 1113–1126.
- (193) Kalfus, J.; Jancar, J. Relaxation Processes in PVAc-HA Nanocomposites. *J. Polym. Sci. Part B Polym. Phys.* **2007**, *45* (11), 1380–1388.
- (194) Kalfus, J.; Jancar, J. Elastic Response of Nanocomposite Poly(Vinylacetate)-Hydroxyapatite with Varying Particle Shape. *Polym. Compos.* **2007**, *28* (3), 365–371.
- (195) Kalfus, J.; Jancar, J. Immobilization of Polyvinylacetate Macromolecules on Hydroxyapatite Nanoparticles. *Polymer (Guildf)*. **2007**, *48* (14), 3935–3937.
- (196) Dorigato, A.; Dzenis, Y.; Pegoretti, A. Filler Aggregation as a Reinforcement Mechanism in Polymer Nanocomposites. *Mech. Mater.* **2013**, *61*, 79–90.
- (197) Potts, J. R.; Dreyer, D. R.; Bielawski, C. W.; Ruoff, R. S. Graphene-Based Polymer Nanocomposites. *Polymer (Guildf)*. **2011**, *52* (1), 5–25.
- (198) Jancar, J.; Hoy, R. S.; Jancarova, E.; Zidek, J. Effect of Temperature, Strain Rate and Particle Size on the Yield Stresses and Post-Yield Strain Softening of PMMA and Its Composites. *Polymer (Guildf)*. **2015**, *63*, 196–207.
- (199) Tannenbaum, R.; Zubris, M.; David, K.; Ciprari, D.; Jacob, K.; Jasiuk, I.; Dan, N. FTIR Characterization of the Reactive Interface of Cobalt Oxide Nanoparticles Embedded in Polymeric Matrices. *J. Phys. Chem. B* **2006**, *110* (5), 2227–2232.
- (200) Ciprari, D.; Jacob, K.; Tannenbaum, R. Characterization of Polymer Nanocomposite Interphase and Its Impact on Mechanical Properties. *Macromolecules* **2006**, *39* (19), 6565–6573.
- (201) Kopesky, E. T.; McKinley, G. H.; Cohen, R. E. Toughened Poly(Methyl Methacrylate) Nanocomposites by Incorporating Polyhedral Oligomeric Silsesquioxanes. *Polymer (Guildf)*. **2006**, *47* (1), 299–309.
- (202) Hall, L. M.; Jayaraman, A.; Schweizer, K. S. Molecular Theories of Polymer Nanocomposites. *Curr. Opin. Solid State Mater. Sci.* **2010**, *14* (2), 38–48.
- (203) Kalra, V.; Escobedo, F.; Joo, Y. L. Effect of Shear on Nanoparticle Dispersion in Polymer Melts: A Coarse-Grained Molecular Dynamics Study. *J. Chem. Phys.* **2010**, *132* (2),

24901.

- (204) Tuteja, A.; Mackay, M. E.; Narayanan, S.; Asokan, S.; Wong, M. S. Breakdown of the Continuum Stokes-Einstein Relation for Nanoparticle Diffusion. *Nano Lett.* **2007**, *7* (5), 1276–1281.
- (205) Tuteja, A.; Duxbury, P. M.; Mackay, M. E. Multifunctional Nanocomposites with Reduced Viscosity. *Macromolecules* **2007**, *40* (26), 9427–9434.
- (206) Yanez, J. A.; Laarz, E.; Bergström, L. Viscoelastic Properties of Particle Gels. *J. Colloid Interface Sci.* **1999**, *209* (1), 162–172.
- (207) Cassagnau, P. Melt Rheology of Organoclay and Fumed Silica Nanocomposites. *Polymer (Guildf)*. **2008**, *49* (9), 2183–2196.
- (208) Yziquel, F.; Carreau, P. J.; Tanguy, P. A. Non-Linear Viscoelastic Behavior of Fumed Silica Suspensions. *Rheol. Acta* **1999**, *38* (1), 14–25.
- (209) Paquien, J.-N.; Galy, J.; Gérard, J.-F.; Pouchelon, A. Rheological Studies of Fumed Silica–polydimethylsiloxane Suspensions. *Colloids Surfaces A Physicochem. Eng. Asp.* **2005**, *260* (1–3), 165–172.
- (210) Zhu, Z.; Thompson, T.; Wang, S.-Q.; von Meerwall, E. D.; Halasa, A. Investigating Linear and Nonlinear Viscoelastic Behavior Using Model Silica-Particle-Filled Polybutadiene. *Macromolecules* **2005**, *38* (21), 8816–8824.
- (211) Piau, J.-M.; Dorget, M.; Palierne, J.-F.; Pouchelon, A. Shear Elasticity and Yield Stress of Silica–silicone Physical Gels: Fractal Approach. *J. Rheol. (N. Y. N. Y)*. **1999**, *43* (2), 305–314.
- (212) Robertson, C. G.; Warren, S.; Plazek, D. J.; Roland, C. M. Reentanglement Kinetics in Sheared Polybutadiene Solutions. *Macromolecules* **2004**, *37* (26), 10018–10022.
- (213) Akhlaghi, O.; Menciloglu, Y. Z.; Akbulut, O. Rheological Behavior of Poly(Acrylonitrile) Concentrated Solutions: Effect of Sb<sub>2</sub>O<sub>3</sub> Nanoparticles on Shear and Extensional Flow. *Colloid Polym. Sci.* **2016**, *294* (9), 1463–1473.
- (214) Zhang, Q.; Archer, L. A. Poly(Ethylene Oxide)/Silica Nanocomposites: Structure and Rheology. *Langmuir* **2002**, *18* (26), 10435–10442.
- (215) Solomon, M. J.; Almusallam, A. S.; Seefeldt, K. F.; Somwangthanaroj, A.; Varadan, P. Rheology of Polypropylene/Clay Hybrid Materials. *Macromolecules* **2001**, *34* (6), 1864–1872.
- (216) Bair, S.; Yamaguchi, T.; Brouwer, L.; Schwarze, H.; Vergne, P.; Poll, G. Oscillatory and Steady Shear Viscosity: The Cox–Merz Rule, Superposition, and Application to EHL Friction. *Tribol. Int.* **2014**, *79*, 126–131.
- (217) Kabanemi, K. K.; Héту, J.-F. A Reptation-Based Model to the Dynamics and Rheology of Linear Entangled Polymers Reinforced with Nanoscale Rigid Particles. *J. Nonnewton.*

*Fluid Mech.* **2010**, *165* (15–16), 866–878.

- (218) Ravindranath, S.; Wang, S.-Q.; Olechnowicz, M.; Chavan, V. S.; Quirk, R. P. How Polymeric Solvents Control Shear Inhomogeneity in Large Deformations of Entangled Polymer Mixtures. *Rheol. Acta* **2010**, *50* (2), 97–105.
- (219) van der Vaart, K.; Rahmani, Y.; Zargar, R.; Hu, Z.; Bonn, D.; Schall, P. Rheology of Concentrated Soft and Hard-Sphere Suspensions. *J. Rheol. (N. Y. N. Y.)* **2013**, *57* (4), 1195.
- (220) Martins, P.; Kolen'ko, Y. V.; Rivas, J.; Lanceros-Mendez, S. Tailored Magnetic and Magnetoelectric Responses of Polymer-Based Composites. *ACS Appl. Mater. Interfaces* **2015**, *7* (27), 15017–15022.
- (221) Abramson, S.; Dupuis, V.; Neveu, S.; Beaunier, P.; Montero, D. Preparation of Highly Anisotropic Cobalt Ferrite/Silica Microellipsoids Using an External Magnetic Field. *Langmuir* **2014**, *30* (30), 9190–9200.
- (222) Nakata, K.; Hu, Y.; Uzun, O.; Bakr, O.; Stellacci, F. Chains of Superparamagnetic Nanoparticles. *Adv. Mater.* **2008**, *20* (22), 4294–4299.
- (223) Jung, H. S.; Kwon, S. H.; Choi, H. J.; Jung, J. H.; Kim, Y. G. Magnetic Carbonyl Iron/Natural Rubber Composite Elastomer and Its Magnetorheology. *Compos. Struct.* **2016**, *136*, 106–112.
- (224) An, H.; Picken, S. J.; Mendes, E. Nonlinear Rheological Study of Magneto Responsive Soft Gels. *Polymer (Guildf)* **2012**, *53* (19), 4164–4170.
- (225) Stepanov, G. V.; Abramchuk, S. S.; Grishin, D. A.; Nikitin, L. V.; Kramarenko, E. Y.; Khokhlov, A. R. Effect of a Homogeneous Magnetic Field on the Viscoelastic Behavior of Magnetic Elastomers. *Polymer (Guildf)* **2007**, *48* (2), 488–495.
- (226) Hintze, C.; Borin, D. Y.; Ivaneyko, D.; Toshchevnikov, V.; Saphiannikova-Grenzer, M.; Heinrich, G. Soft Magnetic Elastomers with Controllable Stiffness: Experiments and Modelling. *KGK-KAUTSCHUK GUMMI KUNSTSTOFFE* **2014**, *67* (4), 53–59.
- (227) Mishra, S. R.; Dickey, M. D.; Velev, O. D.; Tracy, J. B. Selective and Directional Actuation of Elastomer Films Using Chained Magnetic Nanoparticles. *Nanoscale* **2016**, *8* (3), 1309–1313.
- (228) Boncheva, M.; Andreev, S. A.; Mahadevan, L.; Winkleman, A.; Reichman, D. R.; Prentiss, M. G.; Whitesides, S.; Whitesides, G. M. Magnetic Self-Assembly of Three-Dimensional Surfaces from Planar Sheets. *Proc. Natl. Acad. Sci.* **2005**, *102* (11), 3924–3929.
- (229) Zeng, M.; Laromaine, A.; Feng, W.; Levkin, P. A.; Roig, A. Origami Magnetic Cellulose: Controlled Magnetic Fraction and Patterning of Flexible Bacterial Cellulose. *J. Mater. Chem. C* **2014**, *2* (31), 6312.
- (230) Andres, C. M.; Zhu, J.; Shyu, T.; Flynn, C.; Kotov, N. A. Shape-Morphing Nanocomposite

- Origami. *Langmuir* **2014**, *30* (19), 5378–5385.
- (231) Nussbaumer, R. J.; Caseri, W. R.; Smith, P.; Tervoort, T. Polymer-TiO<sub>2</sub> Nanocomposites: A Route Towards Visually Transparent Broadband UV Filters and High Refractive Index Materials. *Macromol. Mater. Eng.* **2003**, *288* (1), 44–49.
- (232) Macdonald, E. K.; Shaver, M. P. Intrinsic High Refractive Index Polymers. *Polym. Int.* **2015**, *64* (1), 6–14.
- (233) Tripathi, S. K.; Kaur, R.; Kaur, J.; Sharma, M. Third-Order Nonlinear Optical Response of Ag–CdSe/PVA Hybrid Nanocomposite. *Appl. Phys. A* **2015**, *120* (3), 1047–1057.
- (234) Perrin, F. X.; Panaitescu, D. M.; Frone, A. N.; Radovici, C.; Nicolae, C. The Influence of Alkyl Substituents of POSS in Polyethylene Nanocomposites. *Polymer (Guildf)*. **2013**, *54* (9), 2347–2354.
- (235) Fina, A.; Tabuani, D.; Frache, A.; Camino, G. Polypropylene–polyhedral Oligomeric Silsesquioxanes (POSS) Nanocomposites. *Polymer (Guildf)*. **2005**, *46* (19), 7855–7866.
- (236) Rahman, M. M.; Filiz, V.; Shishatskiy, S.; Abetz, C.; Neumann, S.; Bolmer, S.; Khan, M. M.; Abetz, V. PEBA<sup>®</sup> with PEG Functionalized POSS as Nanocomposite Membranes for CO<sub>2</sub> Separation. *J. Memb. Sci.* **2013**, *437*, 286–297.
- (237) Konietzny, R.; Koschine, T.; Rätzke, K.; Staudt, C. POSS-Hybrid Membranes for the Removal of Sulfur Aromatics by Pervaporation. *Sep. Purif. Technol.* **2014**, *123*, 175–182.
- (238) Liu, A.; Walther, A.; Ikkala, O.; Belova, L.; Berglund, L. A. Clay Nanopaper with Tough Cellulose Nanofiber Matrix for Fire Retardancy and Gas Barrier Functions. *Biomacromolecules* **2011**, *12* (3), 633–641.
- (239) Isfahani, A. P.; Sadeghi, M.; Dehaghani, A. H. S.; Aravand, M. A. Enhancement of the Gas Separation Properties of Polyurethane Membrane by Epoxy Nanoparticles. *J. Ind. Eng. Chem.* **2016**, *44*, 67–72.
- (240) Merkel, T. C. Ultrapervmeable, Reverse-Selective Nanocomposite Membranes. *Science (80- )*. **2002**, *296* (5567), 519–522.
- (241) Vu, D. Q.; Koros, W. J.; Miller, S. J. Mixed Matrix Membranes Using Carbon Molecular Sieves. *J. Memb. Sci.* **2003**, *211* (2), 311–334.
- (242) Mathai, A. M.; Moschopoulos, P.; Pederzoli, G. Random Points Associated with Rectangles. *Rend. del Circ. Mat. di Palermo* **1999**, *48* (1), 163–190.
- (243) Eaton, J. W.; Bateman, D.; Hauberg, S.; Wehbring, R. *GNU Octave Version 4.4.0 Manual: A High-Level Interactive Language for Numerical Computations*; 2018.
- (244) Nowicki, W. Structure and Entropy of a Long Polymer Chain in the Presence of Nanoparticles. *Macromolecules* **2002**, *35* (4), 1424–1436.
- (245) Guenther, A. J.; Lamison, K. R.; Lubin, L. M.; Haddad, T. S.; Mabry, J. M. Hansen

- Solubility Parameters for Octahedral Oligomeric Silsesquioxanes. *Ind. Eng. Chem. Res.* **2012**, *51* (38), 12282–12293.
- (246) Hansen, C. M. *Hansen Solubility Parameters: A User's Handbook, Second Edition*; CRC Press, 2007; Vol. 2.
- (247) Yu, W.; Wang, J.; You, W. Structure and Linear Viscoelasticity of Polymer Nanocomposites with Agglomerated Particles. *Polymer (Guildf)*. **2016**, *98*, 190–200.
- (248) Kumar, S. K.; Jouault, N.; Benicewicz, B.; Neely, T. Nanocomposites with Polymer Grafted Nanoparticles. *Macromolecules* **2013**, *46* (9), 3199–3214.
- (249) You, W.; Yu, W.; Zhou, C. Cluster Size Distribution of Spherical Nanoparticles in Polymer Nanocomposites: Rheological Quantification and Evidence of Phase Separation. *Soft Matter* **2017**, *13* (22), 4088–4098.
- (250) Stefanis, E.; Tzivintzelis, I.; Panayiotou, C. The Partial Solubility Parameters: An Equation-of-State Approach. *Fluid Phase Equilib.* **2006**, *240* (2), 144–154.
- (251) Hudon, P.; Jung, I.-H.; Baker, D. R. Melting of  $\beta$ -Quartz up to 2.0 GPa and Thermodynamic Optimization of the Silica Liquidus up to 6.0 GPa. *Phys. Earth Planet. Inter.* **2002**, *130* (3–4), 159–174.
- (252) He, Y.; Cao, C.; Wan, Y.-X.; Cheng, H.-P. From Cluster to Bulk: Size Dependent Energetics of Silica and Silica-Water Interaction. *J. Chem. Phys.* **2006**, *124* (2), 024722.
- (253) Marmo, M. J.; Mostafa, M. A.; Jinnai, H.; Fowkes, F. M.; Manson, J. A. Acid-Base Interaction in Filler-Matrix Systems. *Ind. Eng. Chem. Prod. Res. Dev.* **1976**, *15* (3), 206–211.
- (254) Fowkes, F. M.; Mostafa, M. A. Acid-Base Interactions in Polymer Adsorption. *Ind. Eng. Chem. Prod. Res. Dev.* **1978**, *17* (1), 3–7.
- (255) Fowkes, F. M. Acid-Base Contributions to Polymer-Filler Interactions. *Rubber Chem. Technol.* **1984**, *57* (2), 328–343.
- (256) Allara, D. L.; Fowkes, F. M.; Noolandi, J.; Rubloff, G. W.; Tirrell, M. V. Bonding and Adhesion of Polymer Interfaces. *Mater. Sci. Eng.* **1986**, *83* (2), 213–226.
- (257) Fowkes, F. M. Quantitative Characterization of the Acid-Base Properties of Solvents, Polymers, and Inorganic Surfaces. *J. Adhes. Sci. Technol.* **1990**, *4* (1), 669–691.
- (258) Drago, R. S.; Vogel, G. C.; Needham, T. E. Four-Parameter Equation for Predicting Enthalpies of Adduct Formation. *J. Am. Chem. Soc.* **1971**, *93* (23), 6014–6026.
- (259) Liu, J.; Wu, Y.; Shen, J.; Gao, Y.; Zhang, L.; Cao, D. Polymer–nanoparticle Interfacial Behavior Revisited: A Molecular Dynamics Study. *Phys. Chem. Chem. Phys.* **2011**, *13* (28), 13058.
- (260) Linden, C. Vander; Leemput, R. Van. Adsorption Studies of Polystyrene on Silica I.

- Polydisperse Adsorbate. *J. Colloid Interface Sci.* **1978**, *67* (1), 63–69.
- (261) Wu, G.; Asai, S.; Sumita, M.; Yui, H. Entropy Penalty-Induced Self-Assembly in Carbon Black or Carbon Fiber Filled Polymer Blends. *Macromolecules* **2002**, *35* (3), 945–951.
- (262) Hamieh, T. Study of the Specific Entropy of Poly ( $\alpha$ -n-Alkyl) Methacrylates Adsorbed on Alumina or Silica by Inverse Gas Chromatography (IGC). *Soft Mater.* **2010**, *9* (1), 15–31.
- (263) Huang, Q.; Mednova, O.; Rasmussen, H. K.; Alvarez, N. J.; Skov, A. L.; Almdal, K.; Hassager, O. Concentrated Polymer Solutions Are Different from Melts: Role of Entanglement Molecular Weight. *Macromolecules* **2013**, *46* (12), 5026–5035.
- (264) Fetters, L. J.; Lohse, D. J.; Colby, R. H. Chain Dimensions and Entanglement Spacings. In *Physical Properties of Polymers Handbook*; Springer New York: New York, NY, 2007; pp 447–454.
- (265) Lu, W.; Yin, P.; Osa, M.; Wang, W.; Kang, N.-G.; Hong, K.; Mays, J. W. Solution Properties, Unperturbed Dimensions, and Chain Flexibility of Poly(1-Adamantyl Acrylate). *J. Polym. Sci. Part B Polym. Phys.* **2017**, *55* (20), 1526–1531.

## 9. Author's publication list

1. Lepcio, P.; Ondreas, F.; Zarybnicka, K.; Zboncak, M.; Caha, O.; Jancar, J. Bulk polymer nanocomposites with preparation protocol governed nanostructure: the origin and properties of aggregates and polymer bound clusters. *Soft Matter*. **2018**, 14, 2094-2103. ISSN: 1744-6848.
2. Lepcio, P.; Ondreas, F.; Jancar, J. The effect of nanoparticles on rheological behavior of polystyrene solutions under large amplitude oscillation shear (LAOS). *Material Science Forum*. **2016**, 851, pp 215–220. ISSN: 0255-5476.
3. Lepcio, P.; Ondreas, F.; Zboncak, M.; Zarybnicka, K.; Jancar, J. Rheology-based evidence on nanoparticle structuring mechanism in solution blended polymer nanocomposites. *DYFP2018 Book of Abstracts*. Eindhoven: **2018**, 300-303, *1<sup>st</sup> prize award for best poster*.
4. Lepcio, P.; Jancar, J. Vliv nanočástic na rheologické chování roztoku polystyrenu při oscilačních smykových testech s velkou amplitudou (LAOS). *Czech chemical society symposium series*. **2015**. s. 24-24. ISSN: 2336-7202.
5. Lepcio, P.; Ondreas, F.; Zboncak, M.; Jancar, J. Rheology-based evidence on nanoparticle structuring mechanism in solution blended polymer nanocomposites. *Curie – Pasteur – CEITEC joint young scientist retreat*. Brno: **2017**. p. 22-2. (*Abstract and talk*).
6. Lepcio, P.; Ondreas, F.; Zboncak, M.; Jancar, J. Rheological investigation into bottom-up solution blending preparation route of polymer nanocomposites. *CEITEC PhD Retreat II, Book of abstracts*. Brno: **2017**. p. 87-87. ISBN: 978-80-210-8550-3.
7. Lepcio, P.; Jancar, J. Nanoparticle induced changes in rheological behavior of polystyrene solutions under LAOS. *Book of Abstracts CEITEC PhD Retreat*. Brno: **2015**. p. 101-101. ISBN: 978-80-210-7825-3.
8. Lepcio, P.; Jancar, J. Rheological behavior of polymer nanocomposite suspensions. *Chemistry & Life 2015 - Book of Abstracts*. Brno: **2015**. p. 187-188. ISBN: 978-80-214-5228-2.
9. Lepcio, P.; Jancar, J. Structure- property relationships in polymer nanocomposites. *Workshop on Structure and Dynamics of Polymer Nanocomposites*. Montpellier: **2015**. p. 24-24.